

COHERENT NONLINEAR OPTICS OF ELECTRON SPINS IN
SEMICONDUCTORS

by

YUMIN SHEN

A DISSERTATION

Presented to the Department of Physics
and the Graduate School of the University of Oregon
in partial fulfillment of the requirements
for the degree of
Doctor of Philosophy

September 2007

“Coherent Nonlinear Optics of Electron Spins in Semiconductors,” a dissertation prepared by Yumin Shen in partial fulfillment of the requirements for the Doctor of Philosophy degree in the Department of Physics. This dissertation has been approved and accepted by:

Dr. Michael G. Raymer, Chair of the Examining Committee

Date

Committee in charge: Dr. Michael G. Raymer, Chair
 Dr. Hailin Wang, Advisor
 Dr. Dietrich Belitz
 Dr. James N. Imamura
 Dr. Andrew H. Marcus

Accepted by:

Dean of the Graduate School

An Abstract of the Dissertation of

Yumin Shen for the degree of Doctor of Philosophy

in the Department of Physics to be taken September 2007

Title: COHERENT NONLINEAR OPTICS OF ELECTRON SPINS IN
SEMICONDUCTORSApproved: _____
Dr. Hailin Wang

This dissertation presents experimental studies of electron spin coherence in semiconductors. The spin coherence arises from a coherent superposition of electron spin states in the conduction band and can be preserved over remarkably long time and length scales. Electron spin coherence in semiconductors provides an effective model system for investigating fundamental issues of quantum coherences in an interacting manybody system. The robustness of the electron spin coherence also makes it a highly promising platform for optical manipulation of quantum coherences and for the development of coherent quantum devices.

Electron spin coherence induced in the presence of a transverse external magnetic field corresponds to a Larmor precession of the electron spin around

the magnetic field. The primary experimental tools for probing and manipulating electron spin coherence are coherent nonlinear optical techniques including transient differential absorption (DA) and time-resolved Faraday rotation (TRFR), which probe, respectively, the oscillations or quantum beats in optical absorption and refractive index induced by the Larmor spin precession.

Nonlinear optical processes in semiconductors are fundamentally modified by inherent manybody interactions between optical excitations. We have developed new experimental techniques based on DA and TRFR to elucidate how these interactions affect and manifest in optical manipulation of electron spins. In an excitonic system, Coulomb interactions between excitons can lead to the formation of bound and unbound two-exciton states. Detailed experimental studies in GaAs and InGaAs quantum wells, along with a phenomenological theoretical analysis, show that the coupling of the spin coherence to the two-exciton states determines the DA and TRFR responses. Nonlinear optical processes via the two-exciton states also lead to a striking difference between closely related TRFR and DA, as revealed by the spectral as well as intensity dependence of the nonlinear optical responses.

We have also demonstrated a spin manipulation scheme that controls the amplitude as well as the phase of the quantum beats from electron spin coherence by exploiting the relative phase between relevant Larmor precessions of electron spins. Surprisingly, the spin manipulation scheme can be more effective in an excitonic system than in a corresponding atomic-like system.

CURRICULUM VITAE

NAME OF AUTHOR: Yumin Shen

PLACE OF BIRTH: Henan, China

DATE OF BIRTH: September, 1975

GRADUATE AND UNDERGRADUATE SCHOOLS ATTENDED:

University of Oregon, Eugene, Oregon
Peking University, Beijing, China
Beijing Normal University, Beijing, China

DEGREES AWARDED:

Doctor of Philosophy in Physics, 2007, University of Oregon
Master of Science, 2000, Peking University
Bachelor of Science, 1997, Beijing Normal University

AREAS OF SPECIAL INTEREST:

Semiconductor optics, Spintronics, Cavity QED

PROFESSIONAL EXPERIENCE:

University of Oregon, Eugene, OR.
Graduate Teaching Fellow, 2000 - 2007
Peking University, Beijing, China.
Teaching and Research Assistant, 1997 - 2000
The Institute of Physics, Chinese Academy of Sciences, Beijing, China.
Research Assistant, summer 1997

GRANTS, AWARDS AND HONORS:

Student Travel Grants Award from Division of Laser Science of the American Physical Society, 2005

Student Travel Grants Award from Colorado Meeting on Fundamental Optical Processes in Semiconductors (FOPS), 2004

PUBLICATIONS:

Y. Shen, A. M. Goebel, and H. Wang, “Control of quantum beats from electron spin coherence in semiconductor quantum wells,” *Phys. Rev. B* **75** (2007) 045341.

Y. Shen, A.M. Goebel, G. Khitrova, H.M. Gibbs, and H. Wang, “Nearly degenerate time-resolved Faraday rotation in an interacting exciton system”, *Phys. Rev. B* **72** (2005) 233307.

ACKNOWLEDGEMENTS

First and to the most, I would like to thank Dr. Hailin Wang, my advisor, for all his help on supporting my Ph.D. research and on coaching me how to become a scientist. Without his insightful guidance, rigorous attitude, great passion and hand-in-hand help, it would be extremely hard for me to accomplish my dissertation research. Secondly, I want to thank all my colleagues. In this great lab, everybody is willing to help each other on research and experiments. I would like to thank Alexander M. Goebel, on his contribution to the theoretical model. I would like to thank Dr. Mark Philips, Dr. Scott Lacy, and Dr. Phedon Palinginis, for the experimental skills I learned from them. I would like to thank Dr. Susanta Sarkar, Dr. Sasha Tavenner Kruger, Shannon O’Leary, Tim Sweeney, Yan Guo, Young-Shin Park and Andrew Cook for their help to my experiments. Also I would like to thank Guoqiang Cui and Dr. Mats Larsson for many useful discussions. I would like to thank Khodadad Nima Dinyari and other colleagues who proofread my thesis. Particularly, I would like to thank Guoqiang Cui for the respective contribution of Fig. 55(b) in this dissertation. I really enjoyed the time I worked and studied in Wang lab, with all these talented and nice people.

I would like to thank Dr. Nai-Hang Kwong and Dr. Rolf Binder for helpful discussions on spin coherence and exciton scattering. I would like to thank Charles

Santory and Dr. Fedor Jelezko for helpful discussions on diamond NV centers. I would like to thank Dr. Michael Raymer for providing advices on revising this dissertation.

I would like to thank Dr. Brian Smith for his help on \LaTeX . I shall thank all the people who work on the GNU projects and Open Source projects, because I use the software they developed to write this thesis, e.g., \TeX for typesetting, R-project for processing and plotting data, and GNU Scientific Library for simulation.

I would like to thank my dearest wife, Zhihong Chen, for her love, endless support, taking care of our daughter and being with me. I would like to thank my father, Dr. Jianzhong Shen, and my mother, for their continuous encouragement on my research in physics. I want to give special thanks to my brother, Huaipu Shen, for taking care of my parents while I am thousands of miles away from home.

To pursue a Ph.D. in physics is not an easy task. I am so lucky that I have the support from the best advisor, my family, and all of my friends, during this most important time of my life.

Dedicated to my beloved family.

TABLE OF CONTENTS

Chapter	Page
I. INTRODUCTION	1
Electron Spin Relaxation in Semiconductors	5
Nonlinear Optical Processes and Manybody Interactions	8
Overview	11
II. EXCITONIC TRANSITIONS IN GaAs QUANTUM WELLS	14
Band Structure of GaAs Quantum Well	17
Optical Selection Rules	19
Exciton States in Semiconductor	23
Biexciton and Two-Exciton States	26
Summary	28
III. ELECTRON SPIN COHERENCE IN GaAs QUANTUM WELLS	29
Electron Spin Coherence Through Optical Excitation	29
GaAs QW Subject to an External Magnetic Field in Voigt Geometry	33
Nonlinear Optical Polarization	38
Quantum Beats from a Three-Level V System	39
Measurements of Spin Coherence	48
Manybody Effects Corrections	52
Summary	54
IV. SAMPLES AND EXPERIMENTAL TECHNIQUES	55
Semiconductor QW Samples	55
Laser System	58
External Pulse Shaper	59

Chapter	Page
Super-Conducting Magnetic System	62
Transient Differential Absorption Spectroscopy	63
Time-Resolved Faraday Rotation (TRFR)	65
Overview of Experimental Setup	69
V. ELECTRON SPIN COHERENCE OBSERVED IN TRFR	72
Magnetic Field Dependence	73
Temperature Dependence	74
Detuning Dependence for Degenerate Pump-Probe	76
Summary	80
VI. MANIPULATING SPIN PRECESSION WITH OPTICAL PULSES	81
Spin Control in a Precession Picture	82
Controlling the Amplitude of the Quantum Beats	86
Controlling the Phase of the Quantum Beats	88
Polarization Dependence	92
Summary	94
VII. HIGHER ORDER NONLINEAR PROCESSES IN ABSORPTION QUANTUM BEATS	95
Quantum Beats from an N -exciton System	96
Probe Intensity Dependence of Two-pulse DA	100
Control Intensity Dependence	103
Spectral Response of Absorption Spin Beats	105
Explicit Observation of a $\chi^{(5)}$ Quantum Beat	107
Summary	111
VIII. CONTRIBUTIONS FROM EXCITON INTERACTIONS OBSERVED IN TRFR	112
Two-color Time-Resolved Faraday Rotation	113
TRFR Response from Bound Two-Exciton States	117

Chapter	Page
TRFR Response from Unbound Two-Exciton States	120
Probe Intensity Dependence	125
Summary	129
IX. OPTICAL TRANSITIONS OF DIAMOND NITROGEN VACANCY CENTERS	130
Nitrogen Vacancy Center	131
Sample Preparation	134
Locating NV Centers	136
Photoluminescence Spectrum of NV Centers in Diamond Nanocrystals	137
Blinking and Spectral Diffusion	141
Photon Correlation of NV Emission	148
Summary	150
X. SUMMARY AND OUTLOOK	152
Summary	152
Outlook	154
BIBLIOGRAPHY	157

LIST OF FIGURES

Figure	Page
1. Schematic of type I GaAs quantum well.	18
2. Band structure for bulk GaAs and GaAs quantum wells.	19
3. Optical selection rule for bulk GaAs and GaAs quantum wells.	22
4. The energy bands of an exciton.	25
5. Schematic of N -exciton states for HH excitons.	27
6. Dipole coherence in two-level system.	30
7. Excitation of spin coherence through two dipole allowed transitions.	31
8. A classical Larmor spin precession model.	31
9. The Voigt geometry.	34
10. Optical selection rules for HH transition of GaAs QW subject to an external magnetic field in Voigt geometry.	37
11. Energy diagram of a three-level V system.	40
12. Numerical simulation results of DA and TRFR measurements.	53
13. Linear absorption spectrum for a 17.5 nm GaAs SQW (sample A) at 10 K.	56
14. Linear absorption spectrum for a 13.0 nm GaAs MQW (sample B) at 10 K.	56
15. Linear absorption spectrum for an 8 nm InGaAs MQW (sample C) at 10 K.	57
16. Schematic of the pulse shaper apparatus.	60
17. Schematic of the transient DA apparatus.	64
18. Schematic of the TRFR apparatus.	68
19. Schematic of the experimental apparatus.	70
20. TRFR quantum beats from the 13 nm GaAs MQW (sample B) at 10 K measured as a function of magnetic field.	73
21. Degenerate TRFR responses obtained in a 13 nm GaAs MQW (sample B) at various temperatures.	75
22. Temperature dependence of $ g_e $ and T_2^*	77
23. Detuning dependence of degenerate TRFR.	78
24. Schematic of tipping a precessing spin by an optical pulse.	83
25. Schematic of the three-pulse DA setup.	84
26. DA responses as a function of the pump-probe delay with a fixed delay, τ_2 , between the control and probe. The quantum beat amplitudes are changed as a function of control intensity.	87

Figure	Page
27. DA responses as a function of the pump-probe delay with a fixed delay, τ_2 , between the control and probe. The quantum beat phase is changed as a function of control intensity.	89
28. The relative contribution to quantum beats from the parallel (circles) and perpendicular (squares) spin components as a function of the control intensity.	90
29. DA responses as a function of the pump-probe delay at a fixed τ_2 given by 61 ps, 54 ps, 46 ps, 38 ps, 31 ps, 23 ps, 15 ps, and 7ps. . . .	91
30. The absorption quantum beats of 17.5 nm GaAs SQW obtained at $B = 3$ T and $T = 10$ K.	93
31. Optical selection rule for the transitions between the conduction and the $J_z=3/2$ valence bands in a magnetic field along the x-axis, illustrated in N -exciton energy eigenstates of ground, one-exciton, and two-exciton states. States are labeled by electron spin.	96
32. Probe intensity dependence of degenerate DA observed from sample A.	101
33. Probe intensity dependence of $\Delta T/T$ beat amplitude.	102
34. Control intensity dependence of degenerate DA of sample A.	104
35. Fitted quantum beat amplitudes as a function of control intensity	105
36. Control intensity dependence of the DA spectral response of sample A obtained at 10 K and $B = 3$ T.	106
37. Control field polarization dependence obtained in sample A at 10 K and $B = 3$ T.	108
38. Control intensity dependence of DA response with a fixed probe-pump delay, $\tau_1 = 210$ ps, and scanning control pulse.	109
39. DA response with a fixed probe-pump delay, $\tau_1 = 186$ ps, and scanning control pulse.	110
40. Two-color TRFR Spectra of the 13 nm GaAs MQW (sample B).	114
41. Two-color TRFR Spectra of 17.5 nm GaAs SQW (sample A) at 10 K.	115
42. The linear absorption, spin polarization rotation beats amplitude A_θ , transverse spin decoherence rate T_2^* , and electron spin g_e factor, measured as a function of probe detuning with sample A.	116
43. DA spectra of sample A obtained at $B = 0$ T and $T = 10$ K where the pump and probe have co- (solid line) and counter-circular (dashed line) polarization.	118

Figure	Page
44. Schematic of N -exciton energy eigenstates for σ^- excited HH transitions with related biexciton transitions under Voigt geometry magnetic field.	119
45. Calculated TRFR spectral responses.	121
46. DA spectra of InGaAs MQW (sample C) at 10 K.	122
47. Two-color TRFR Spectra of InGaAs QW at 10 K.	123
48. Two-color TRFR Spectra of sample C at 80 K.	124
49. DA spectra of InGaAs QW at 80 K.	125
50. A comparison of DA spin beat amplitude and TRFR spin beat amplitude spectra.	126
51. Probe intensity dependence of degenerate TRFR of sample A.	128
52. Structure of single Nitrogen-Vacancy Center of Diamond.	132
53. A typical PL spectrum of NV centers in diamond nanocrystals obtained at room temperature.	132
54. The energy diagram of the NV^- transition.	133
55. The SEM images of diamond crystals deposited on Si wafer.	135
56. Scanning laser fluorescence image of a diamond nanocrystal on the Si wafer.	138
57. PL spectrum of a single diamond microcrystal at 7.5 K with a 1.2 mW 532 nm excitation.	139
58. Micro PL spectrum obtained with a diamond nanocrystal sample B at 9 K, and micro PL spectrum obtained with a diamond nanocrystal sample A at 8 K.	140
59. A PL spectrum obtained from a collection of a large amount of nanocrystal sample A at 10 K. PLE is done by scanning a laser cross the NV^- zero-phonon absorption line indicated by the arrow. The emissions from phonon side bands at wavelength longer than 650 nm (shaded area) are detected.	142
60. A blinking NV center observed in repeated PLE scans. Data obtained from nanocrystal sample B at 10K, with an excitation laser power of 200 nW. The two peaks correspond to emissions from the same NV center.	143
61. Repeated scans of PLE obtained at 10 K from nanocrystal sample B, with an excitation laser power of 200 nW is shown in (b). The averaged spectrum is shown in (a).	144
62. Repeated scans of PLE obtained at 10 K from nanocrystal sample B, with an excitation laser power of 300 nW using a dye laser.	146
63. PLE spectra obtained at 10 K from nanocrystal sample B. The three representative scans are vertically offset for clarity.	147

Figure	Page
64. PLE spectrum of a zero phonon-line transition from a NV center at 10 K. A Lorentzian lineshape fitting is shown in red solid line, with a linewidth of 16 MHz.	148
65. A photon antibunching with a 532 nm excitation indicates a limited number of emitters under excitation.	149
66. A photon antibunching of NV center emissions obtained from nanocrystal sample B, with a 100 nW 639.2 nm excitation at 9 K.	150
67. An SEM image of a toroidal silica micro cavity on a silicon chip.	156

LIST OF TABLES

Table	Page
1. Matrix elements of dipole moment D_{cv}/D	21
2. Matrix elements of dipole moment D_{cv}/D for HH transition under transverse magnetic field in Voigt geometry.	36

CHAPTER I

INTRODUCTION

Thanks to the tremendous development of LASER technology since the 1960's, optical coherence can be initialized and synchronized with extremely high resolution [1]. Interest is growing in the effort of storing the optical coherence in atoms or solid state systems, which in turn can be used as a platform for coherent quantum control [2].

Coherence is a widely adopted concept and can mean different things under different circumstances. This dissertation is focused on electron spin coherence, which is one type of quantum coherences. Quantum coherence plays an essential role in quantum control, quantum information processing, and quantum information storage. For a quantum system, quantum coherence can be understood as a well-defined phase relationship between the probability amplitudes of two eigenstates in a superposition state. If the eigenstates in a superposition state correspond to different electron spin

states, we say that the system has an electron spin coherence. The coherence evolves in time and vanishes in a finite time. This vanishing time is called decoherence time.

Due to the complex manybody interactions in solids, common electronic quantum coherences in semiconductors are generally very short-lived. Under liquid helium temperature the dipole coherence vanishes within picosecond time scale. In spite of the fragile dipole coherence, the observation of Rabi oscillation in semiconductors suggests that decoherence in semiconductors can be overcome and optical manipulation of quantum coherence can be achieved [3]. Nevertheless, a system that will preserve the quantum coherence for a much longer time, preferably at room temperature, is highly desired.

A better quantum coherence in semiconductors is the spin coherence. More recent studies have focused on electron spin coherence, since compared with other excitonic coherences, electron spin coherence is exceptionally robust [4]. In semiconductors, conduction electron spin coherence displays a very long decoherence time compared to other forms of electronic quantum coherence. A submicrosecond spin decoherence time was reported in a 2-D electron gas system [5]. Electron spin coherence can also persist to room temperature. Due to these robust qualities, electron spin coherence promises to be a good candidate for future applications of quantum coherence [6].

Spin coherence can lead to applications such as electromagnetic induced transparency (EIT), slow light and coherent photon storage [2]. Furthermore, a

new active field called *spintronics* has emerged, and is well known to both the physics and engineering communities, in recent years. As a consequence, there has been an increasing interest in developing spin polarized semiconductor devices and exploiting the spins within the solid state systems for quantum information storage and computing. While new physics about the spin relaxation and spin decoherence processes are under extensive investigation, targeting on a better material and structure, studies for the purpose of active control and manipulation of spin degrees of freedom in solid state systems are also being carried out [7].

Among all the spin manipulation efforts, optical initialization and manipulation of the electron spin in semiconductors are shown to be an important and useful approach [4, 6, 8]. The process of the quantum coherence manipulation includes three steps. Firstly, quantum coherence has to be prepared. Secondly, a manipulation has to be done within the decoherence time with high precision both in time and phase. Thirdly, the resulting coherence information must be accurately readout and correctly interpreted. To meet all the requirements, an optical method is the best candidate due to the availability of extremely high precision optical coherence source and ultrafast laser technologies. On the other hand, semiconductors and their heterostructures provide a convenient platform compared to atomic systems thanks to the matured semiconductor industry. The combination of these two advantages is destined to lead to significant advancement in the future.

For the purpose of optical manipulation of electron spins in semiconductors, the nonlinear optical methods dominate. Thus an understanding of the coherent nonlinear optical processes associated with the electron spins is essential for further applications. Unlike an atomic system, manybody interactions in semiconductors can not generally be ignored. It is well known that exciton-exciton interactions playing an important role in the nonlinear optical responses of semiconductors. Therefore, how these manybody effects contribute to the nonlinear response of electron spin coherence is an important issue. In most studies of the electron spin coherence, however, this important issue has been overlooked. In the experimental studies presented in this dissertation, this problem has been emphasized. We have developed new techniques to investigate how unusual nonlinear optical responses of electron spins can be manifest through exciton-exciton interactions. This dissertation provides rich experimental results as well as new methods and understandings to the optical nonlinear processes associated with the electron spin coherence in an excitonic system. Furthermore, as shown in Chapter VI, these understandings can be exploited to manipulate the electron spin coherence. Before the presentation of the detailed experimental results, we shall first review the most studied problem associated with electron spin coherence – the spin relaxation mechanism.

Electron Spin Relaxation in Semiconductors

Electrons can be injected into the conduction band of semiconductors and their spins can be oriented using optical techniques, in which circularly polarized photons transfer their angular momenta to the electrons. The details can be seen from the optical dipole selection rules, as shown later in Chapter II. By controlling the polarization of the optical field one can create a spin population as well as a spin coherence with the conduction electrons, as discussed in Chapter III. In this section, a brief review on spin relaxation and decoherence mechanisms is presented.

Few interactions can couple to electron spin states directly. The spin relaxation time in semiconductors can be even longer than the photo-excited carrier lifetime, leading to a polarized photoluminescence in optical orientation experiments [9]. Several mechanisms are shown to be responsible for spin relaxation and spin dephasing in semiconductors. Most of them involve spin-orbit coupling combined with momentum scattering to provide a randomizing process. The four major mechanisms mostly considered in nonmagnetic electronic systems are Elliott-Yafet, Dyakonov-Perel, Bir-Aronov-Pikus, and hyperfine-interaction processes.

The Elliott-Yafet mechanism is due to spin-orbit coupling which leads to an admixture of spin states. It can be induced by lattice ions, impurities, or phonons. With momentum scattering, the spin-up and spin-down states can couple and lead to spin relaxation. This mechanism is considered important for metal and small band

gap semiconductors with large spin-orbit splitting, or with a high impurity scattering rates, but is considered less significant at higher temperatures.

The Dyakonov-Perel mechanism is due to the spin-orbit interaction in crystals without an inversion center. In such symmetry the spin states of electrons in the conduction band are not degenerate at $k = 0$. This spin splitting can be described as a k -dependent effective magnetic field. As a result, the momentum relaxation process will couple to the spin relaxation and dephasing. This mechanism dominates spin dephasing in middle-gap semiconductors at high temperatures. This effect is important in most cases and is the dominating mechanism in GaAs quantum wells (QWs).

The Bir-Aronov-Pikus mechanism arises from the exchange interaction between electrons and holes. This process is important for p-doped semiconductors at low temperatures. The hyperfine interaction is the magnetic interaction between the magnetic moments of electrons and nuclei. It is important for localized electrons of QWs, but in most cases it is very weak. The contributions of these proposed mechanisms for different semiconductor systems can be investigated by many magneto-optical experimental methods.

For probing and monitoring spin states for the study of spin relaxation and decoherence mechanisms of conduction electrons, both spectrally resolved methods and time-resolved methods are used. The magnetization spectral measurements such as electron spin resonance (ESR) [10] and measurements using the Hanle effect

combined with continuous wave (CW) optical orientation [11] are used to study the spin relaxation and to measure the electron g -factor. However, these methods require a relatively large carrier density, which limits their sensitivity. On the other hand, directly probing and manipulating the electron spins in the time domain is one of the major tasks of spintronics engineering.

In the time domain, the quantum coherence can be observed by the beating of the probability amplitudes in the time evolution of a superposition state. From this the spin relaxation and decoherence time can be directly measured. The time-resolved measurements on spin coherence induced quantum beats also provide a precise way to measure the g -factors. The theory of quantum beats from closely separated energy levels was first introduced by Breit in 1933 [12]. Early time-domain quantum beats studies were performed by shuttered spectral lamps which is what Alexandrov did in 1964 with the Zeeman sublevels in the neutral Cd atom by observing the fluorescence [13]. Compared to the time-resolved fluorescence [14], ultrafast nonlinear optical methods provide more information, higher signal/noise ratio, with less dependence on sample properties. In recent years, many different transient nonlinear optical methods have been used to study the electron spin coherence, such as transient differential absorption (DA), time-resolved Faraday rotation (TRFR) [15], time-resolved Kerr-rotation (TRKR) [16], and transient four-wave mixing (TFWM), to name a few.

These ultra-fast nonlinear optical methods allow the study of spin relaxation and spin decoherence at a relatively low excitation level. Generally, the results of

TRFR and TRKR can be understood as magneto-optical effects, where the rotation angle of linearly polarized probe field transmitted through (Faraday) or reflected by (Kerr) a magnetized sample is proportional to the amount of magnetization in the direction of the incident light. However, this simple model cannot account for the higher-order nonlinear processes observed in the experiments. In this dissertation we use a phenomenological model based on an effective density matrix formalism approach in an N -exciton picture to describe the pathways of nonlinear processes associated with excitonic manybody interactions. The understanding based on this model from the order-by-order perturbation theory is demonstrated in the experiments.

Nonlinear Optical Processes and Manybody Interactions

Optical nonlinearities arising from electron spin coherence can be measured through numerous methods and can be observed as quantum beat in different forms, such as differential absorption, four-wave mixing signal, and differential polarization rotation. The observed signals from different methods however, are expected to be correlated since they all originate from the same nonlinear polarization. On the other hand, it is important to understand what has been measured in each technique, and what each of these nonlinear optical signals can individually tell us.

As a matter of fact, a tremendous amount of research has been done on nonlinear optics in atomic systems. However, for systems like semiconductors, theoretical analysis always needs sophisticated models which include the effects of manybody interactions to completely describe the system. But due to the nature of excitonic transitions, in some situations, the nonlinear processes can be qualitatively described in terms of the simpler optical Bloch equations (OBE) of analogous atomic-like systems [17]. We can obtain basic physics from the analogous atomic-like system without involving manybody complexities at an early stage. Correlations and other interactions can then be introduced to enrich our model step-by-step, leading to effective semiconductor optical Bloch equations [18].

If we consider the interactions of excitons in addition to the simple dilute atomic-like model, just as two hydrogen atoms form a hydrogen molecule, two excitons can also form a molecular state called a biexciton (BX) due to Coulombic interactions with a binding energy in the order of several meV. A biexciton is a four-particle system consisting of two electrons with opposite spin and two holes. Biexciton states modify semiconductor optical properties dramatically [19]. Not only can extra nonlinearities be attributed to the existence of biexcitons [20], but also special quantum coherence experiments like EIT can be directly addressed to biexciton resonance [21]. More complicated many-exciton systems may also form, offering challenging but interesting systems to study [22].

Regardless of the similarities between excitons and atoms, excitons are subject to effects and interactions that are simply not found in atomic systems. As a collective excitation in a solid, excitons are created or annihilated during optical transitions. Compared to a closed atomic system, where atomic density is conserved during optical interactions, the density of excitons in semiconductor depends strongly on the excitation level. As a result, much stronger nonlinear optical effects can be found in excitonic systems than in purely atomic systems. With a high density of excitons, the increased scattering leads to effects such as excitation induced dephasing (EID) [23].

Both theoretical analysis and experimental results have shown that exciton-exciton correlations can contribute significantly to nonlinear optical responses [22, 24, 25]. Previous studies demonstrate that exciton-exciton correlations can contribute a fifth order spin coherence signal to the differential absorption signal [26]. So how exciton-exciton correlations contribute to TRFR is an interesting question.

Furthermore, exciton-exciton correlations can be also used as an assistance to achieve coherent manipulations of electron spin precession. This dissertation demonstrates a rare case where manybody interactions play an essential role in the optical coherent manipulation of nonlinear optical responses.

The following questions on nonlinear optical processes associated with electron spin coherence are of special interest and are addressed in this thesis:

- (a) From a nonlinear optics point of view, how does electron spin coherence contribute to the TRFR nonlinear optical signal?
- (b) How does the nonlinear optical response from electron spin coherence in semiconductor excitonic systems differ from a simple atomic-like model?
- (c) What is the significance of the correlated excitons in bound or unbound states in a nonlinear optical process associated with the spin coherence response in semiconductors?

Overview

This dissertation aims to provide a better understanding of optical interactions associated with electron spin coherence in undoped GaAs QWs.

Chapter II gives a brief review of semiconductor optics, which describes some basic concepts used throughout the thesis.

Chapter III starts with a semi-classical phenomenological treatment of the nonlinear optical response of electron spin coherence in a GaAs QW. An analytical calculation as well as a numerical simulation of quantum beats associated with the electron spin coherence in a V-type system is presented. A phenomenological model of the manybody interactions based on an N -exciton eigenstates is discussed.

Chapter IV introduces the QW samples used, as well as the experimental setup and techniques developed in this research.

Chapter V presents studies of magnetic field dependence, temperature dependence and excitation detuning dependence of the electron spin coherence, based on a degenerate TRFR experiment.

Chapter VI demonstrates an optical spin precession manipulation scheme that controls the amplitude as well as the phase of the quantum beats from electron spin coherence, by exploiting the relative phase between relevant Larmor precessions and by tipping the precessing spin at a specified time.

Chapter VII presents a theoretical analysis using a phenomenological N -exciton eigenstates model. The study indicates that the spin manipulation scheme discussed in Chapter VI can take advantage of the underlying exciton-exciton interactions inherent in a semiconductor and can be more effective in an excitonic system than in a corresponding atomic-like system. The higher order contributions to absorption quantum beats from different transition pathways are examined experimentally by three-pulse transient DA measurements.

Chapter VIII presents studies of the spectral responses from TRFR by performing a non-degenerate two-color pump-probe experiment. A multi-dispersive response of electron spin coherence in non-degenerate TRFR is observed. By comparing the results with a phenomenological simulation from the semiconductor Bloch equations, pronounced contributions from exciton resonance and exciton-exciton correlations are identified.

Chapter IX presents a study of the optical transitions for Nitrogen-Vacancy (NV) centers in diamond nanocrystals. This system features electron spin ground states that have an ultra-long spin relaxation time and decoherence time. Preliminary results of spectral diffusion and zero-phonon linewidth based on photoluminescence and photoluminescence excitation experiments are presented.

Chapter X presents a summary of the experimental results. Possible future work is also discussed there.

CHAPTER II

EXCITONIC TRANSITIONS IN GaAs QUANTUM WELLS

This chapter is aimed to give a brief summary and basic background on semiconductor optics for discussions in following chapters. Readers who are familiar with semiconductor optics can skip this chapter. Details can be found from Ref. [17, 27–29] and references therein.

Due to the diffraction of electrons in a periodic crystal lattice, the electron wavefunctions in the semiconductor forms an energy band structure in the reciprocal space. At zero temperature, the energy bands of semiconductor features an empty lowermost unoccupied band (called the conduction band) above an uppermost fully occupied band (called the valance band). The energy difference between the bottom of the conduction band and the top of the valance band is called the band gap energy (E_g). The band gap of semiconductors ranges from 0.27 eV for lead selenide (PbSe) at 300 K to 3.6 eV for zinc sulfide (ZnS) at 300 K. At room temperature commonly used semiconductors silicon (Si) has a band gap of 1.11 eV and gallium arsenide

(GaAs) has a band gap of 1.43 eV. As a result of being in this intermediate band gap range, semiconductor obtained its name, because in semiconductors, at none-zero temperatures a finite number of electrons can reach the conduction band by thermal excitation and provides some conductivity in between conductors and insulators. Due to the fact that commonly used light fields from near infrared (down to wavelength 5 micron) to near ultraviolet (up to wavelength 200 nm) happen to sit right within the range from 0.25 eV to 6.2 eV, semiconductors are a natural candidate for optical applications.

Semiconductors can be classified into two categories: direct band gap semiconductors and indirect band gap semiconductors. A direct band gap means that the minimum energy of the conduction band lies directly above the maximum energy of the valence band in the energy-momentum space. GaAs is a direct band gap semiconductor. In contrast, an indirect band gap is a band gap in which the minimum energy in the conduction band is shifted by a momentum vector relative to the maximum energy of valence band. Si is an indirect band gap semiconductor. The interband optical transitions in semiconductors are determined by the band edge structures. Because light (photons) carries very small momentum, in general, indirect band gap semiconductors have a much less efficient interband emission processes compare to direct band gap semiconductors.

GaAs is the major direct band gap semiconductor material in use today. At the Γ point, i.e., at $k = 0$, the p -like valence band has its maximum and the s -like

conduction band has its minimum. The optical transition between valence band and the conduction band is dipole allowed.

When an electron is excited from the valence band into the conduction band (by absorbing a photon for example), the missing electron in the valence band leaves a “hole” behind, of opposite electric charge. The electron in the nearly empty conduction band can be described as a nearly free electron with an effective mass m_e . For the almost full valence band, the missing electron can be described by a quasi particle, a hole, moving in the periodical crystal potential with an effective mass m_h .

For bulk GaAs the conduction band is isotropic and parabolic at the Γ point with a two-fold degeneracy due to the electron’s spin. The electron state can be labeled with the spin quantum number $s = \pm 1/2$. The valence band can be described by the total angular momentum J . $J = 1/2$ denote for two-fold degenerate split-off (SO) valence bands (or lower valence band). $J = 3/2$ denote for upper valence bands with a four-fold degeneracy at $k = 0$. For $k \neq 0$ the upper valence band further split into two bands which have different curvature in the $E - k$ dispersion. The $J_z = \pm 3/2$ bands have a smaller radius and are known as heavy hole (HH) bands standing for having a larger effective mass. The $J_z = \pm 1/2$ bands have a larger radius and are known as light hole (LH) bands standing for having a smaller effective mass.

Thanks to high electron mobility, GaAs features a very good high frequency response. As a result, GaAs is widely used in communication applications

such as in mobile phones and wireless fidelity (Wi-Fi) devices. Moreover, the matured molecular beam epitaxy (MBE) or metal-organic chemical vapor deposition (MOCVD) techniques allow high quality heterostructures of GaAs species to be grown. In addition to the direct band gap, the convenience of making artificial heterostructures gives GaAs the opportunity to become a very important material for optical applications.

Band Structure of GaAs Quantum Well

QW is an important example of quantum heterostructures. A particle in a QW is confined in a one-dimension potential well, where the de Broglie length of the particle is comparable, or larger than, the well width l_z . A semiconductor single QW (SQW) can be grown by having a material sandwiched between two layers of a material with a wider band gap. A series of QWs can be stacked together. If it has barriers thick enough to prevent overlaps of the wavefunctions in adjacent wells, it is called multiple QW (MQW). A complex layered structures of gallium arsenide in combination with aluminum arsenide (AlAs) or the alloy $\text{Al}_x\text{Ga}_{1-x}\text{As}$ can be grown to make different types of QWs. Because GaAs and AlAs have almost the same lattice constant, the layers have very little induced strain, which allows them to be grown at very high quality. Figure 1 shows a band structure of type I (electrons and holes are confined in the same material) GaAs QW.

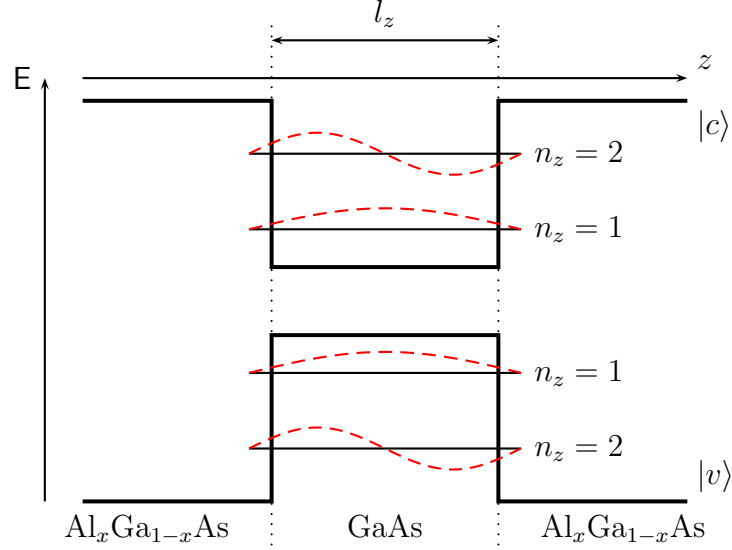


FIGURE 1. Schematic of type I GaAs quantum well.

As a result of the quantum confinement in the z direction, assuming infinitely high barriers on both side of QW, the energy of the particle in the well is quantized as

$$E_{n_z} = \frac{\hbar^2 \pi^2}{2m l_z^2} n_z^2, \quad n_z = 1, 2, 3 \dots \quad (2.1)$$

The energy band of the bulk material becomes a series of subbands with dispersion relation

$$E(\mathbf{k}) = E_{n_z} + \frac{\hbar^2 (k_x^2 + k_y^2)}{2m} \quad (2.2)$$

The energy band dispersion relation of GaAs and GaAs QWs close to the Γ point in the momentum space are shown in Fig. 2.

In a QW the degeneracy of LH and HH bands is further removed at $k = 0$ by the QW potential. Due to the confinement, with k in the confinement plane, the

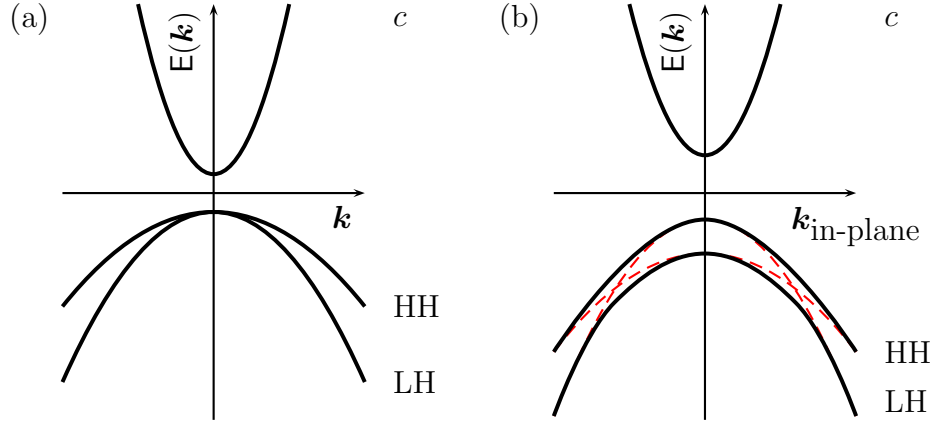


FIGURE 2. Band structure for bulk GaAs (left) and GaAs quantum wells (right). Label c stand for conduction band. Label HH stand for HH sub-bands. Label LH stand for LH sub-bands.

$J_z = 3/2$ state (HH band in the bulk) has a smaller effective mass compare to the $J_z = 1/2$ state (LH band in the bulk). For convenience they are still kept label as HH and LH bands, in spite of the reversed effective mass order close to $k_{\text{in-plane}} = 0$. Without consider mixing the HH and LH bands cross at finite $k_{\text{in-plane}}$, as the red dashed line shown in Fig. 2(b). In reality the HH ($J_z = 3/2$) and LH ($J_z = 1/2$) bands anti-cross and mix at a finite $k_{\text{in-plane}}$. For interband optical transitions close to $k = 0$, HH transition has a smaller energy than the LH transition in GaAs QW.

Optical Selection Rules

The optical transition of GaAs QW from the valance band state $|v\rangle$ to the conduction band state $|c\rangle$ can be approximated by an electric dipole interaction with

an electromagnetic field, $\mathbf{E}(\mathbf{r}, t)$, the perturbation energy is given by

$$V = -e\mathbf{R} \cdot \mathbf{E}(\mathbf{r}, t) = \mathbf{D} \cdot \mathbf{E} \quad (2.3)$$

The optical selection rules are given by evaluating the dipole moment between conduction band state and valance band states,

$$\mathbf{D}_{cv} = \langle c | \hat{\mathbf{D}} | v \rangle \quad (2.4)$$

Taking the quantization axis along with the wave vector \mathbf{k} as well as the crystal axis (001) in z direction, an electron state in the conduction band can be described by a Bloch wave function

$$\psi_m^c = u_m e^{i\mathbf{k} \cdot \mathbf{r}}, \quad m = \pm 1/2 \quad (2.5)$$

where the Bloch amplitudes u_m correspond to two spin states and can be written as

$$u_{1/2}^c = S \uparrow, \quad u_{-1/2}^c = S \downarrow \quad (2.6)$$

The S denotes the s -type wavefunction, the arrows denotes for spin directions.

Likewise the Bloch amplitudes of HH valance band electron states can be described as

$$u_{3/2}^{hh} = -\frac{1}{\sqrt{2}}(P_X + iP_Y) \uparrow \quad (2.7)$$

$$u_{-3/2}^{hh} = \frac{1}{\sqrt{2}}(P_X - iP_Y) \downarrow \quad (2.8)$$

and the Bloch amplitudes of LH valance band electron states can be described as

$$u_{1/2}^{lh} = \frac{1}{\sqrt{3}} \left[-\frac{1}{\sqrt{2}}(P_X + iP_Y) \downarrow + \sqrt{2}P_Z \uparrow \right] \quad (2.9)$$

$$u_{-1/2}^{lh} = \frac{1}{\sqrt{3}} \left[\frac{1}{\sqrt{2}}(P_X - iP_Y) \uparrow + \sqrt{2}P_Z \downarrow \right] \quad (2.10)$$

where P_X, P_Y, P_Z denote the p -type wavefunctions in x, y, z symmetry[9, 30].

The spin functions are normalized and orthogonal for different spin states.

The non-vanishing dipole matrix elements include terms of the form:

$$\langle S|D_x|P_X\rangle = \langle S|D_y|P_Y\rangle = \langle S|D_z|P_Z\rangle \quad (2.11)$$

The matrix element of dipole moment between conduction band states and HH, LH valance band states then are found in Table 1, where the $\hat{e}_x, \hat{e}_y, \hat{e}_z$ are the unit vectors in coordinates x, y, z directions.

TABLE 1. Matrix elements of dipole moment D_{cv}/D .

c		$\langle 1/2, +1/2 $	$\langle 1/2, -1/2 $
HH	$ 3/2, +3/2\rangle$	$-\sqrt{1/2}(\hat{e}_x + i\hat{e}_y)$	0
	$ 3/2, -3/2\rangle$	0	$\sqrt{1/2}(\hat{e}_x - i\hat{e}_y)$
LH	$ 1/2, +1/2\rangle$	$\sqrt{2/3}\hat{e}_z$	$-\sqrt{1/6}(\hat{e}_x + i\hat{e}_y)$
	$ 1/2, -1/2\rangle$	$\sqrt{1/6}(\hat{e}_x - i\hat{e}_y)$	$\sqrt{2/3}\hat{e}_z$

For an optical field interacting with GaAs near the band edge with a low excitation level, only the near-region of $k = 0$ needs to be considered. We can ignore the mixing of bands at larger k for both bulk GaAs and GaAs QW. J_z can be used to identify HH and LH states. The optical dipole transition selection rules are shown in Fig. 3, where an atomic-like energy level diagram is used to label the band structures at $k = 0$.

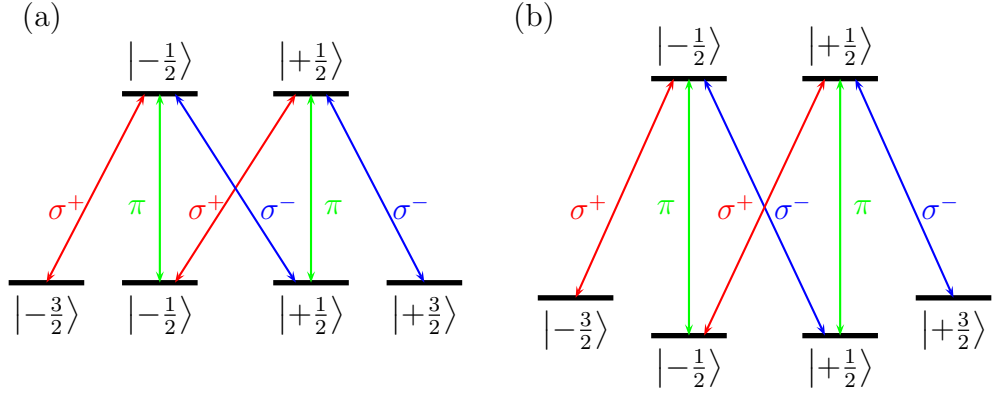


FIGURE 3. Optical selection rule for (a) bulk GaAs and (b) GaAs quantum wells. The states are labeled by electron J_z .

The optical selection rules are the same in bulk or QW form of GaAs. Consider z as the propagation direction of the optical field as well as the normal direction to the QW confinement plane. In Fig. 3 we use σ^+ and σ^- to represent the clockwise (right-handed) and counter-clockwise (left-handed) circularly polarized lights, respectively. We use π to represent an optical field which has a component polarized in the z direction. For the π polarization it can be a field linearly polarized in the plane of

incidence when the incident field is off-normal direction to the surface. This field can also be achieved in a TM waveguide mode [31].

From the diagram shown in Fig. 3 one can see that the two HH subbands are coupled to the two different electron spin states in the conduction band with two orthogonal circularly polarized optical fields, respectively. These well-defined transitions allow direct manipulation of electron spin in GaAs QW through the polarization selection of optical fields. The rest of this thesis is actually focused on HH transitions. However, due to the significance of the Coulomb interactions between the negative charged electrons and positive charged holes, we are actually working with a quasiparticle called an exciton.

Exciton States in Semiconductor

Close to the band edge of a direct gap semiconductor such as GaAs, the optical transitions are dominated by excitonic effects. The optical process of exciting an electron to the conduction band will leave behind a positive charged hole as a quasiparticle particle with an effective mass in the valance band. By Coulomb interaction, the electron and the hole can form an atomic-like bound state called an exciton (X), much like how an electron and a proton form a hydrogen atom. Such a Coulomb-correlated electron-hole pair is an elementary excitation.

The exciton can be treated as a bounded two-particle system. The energy

states of this hydrogen-like system in the bulk material is given by [27]

$$E_x = E_g - Ry^* \frac{1}{n^2} + \frac{\hbar^2 \mathbf{K}^2}{2M}, \quad n = 1, 2, 3 \dots \quad (2.12)$$

where E_g is the bandgap,

$$Ry^* = \left(\frac{\mu}{m\varepsilon_0^2} \right) \times 13.6 \text{ eV} \quad (2.13)$$

is the exciton binding energy,

$$M = m_e + m_h \quad (2.14)$$

is the translational mass of the exciton,

$$\mathbf{K} = \mathbf{k}_e + \mathbf{k}_h \quad (2.15)$$

is the wave vector of the exciton.

So in the two-particle picture the energy states of an exciton in semiconductor can be shown as in Fig. 4. The crystal ground state $|g\rangle$ is a state without exciton.

In semiconductors, the binding energy of excitons Ry^* lies in the range from 1 meV to 200 meV, much less than the band gap E_g . The binding energy of excitons in bulk GaAs is about 4.9 meV. The excitonic Bohr radius varies in the range from 1 nm to 50 nm, which is larger than the lattice constant. The excitons in semiconductors are not associated within a single unit cell. These types of excitons are called Wannier excitons. The Bohr radius of exciton in bulk GaAs is about 11.2 nm [28].

Both HH sub-bands and LH sub-bands can provide holes to bind with an electron in conduction band, forms light- and HH excitons. As described in previous

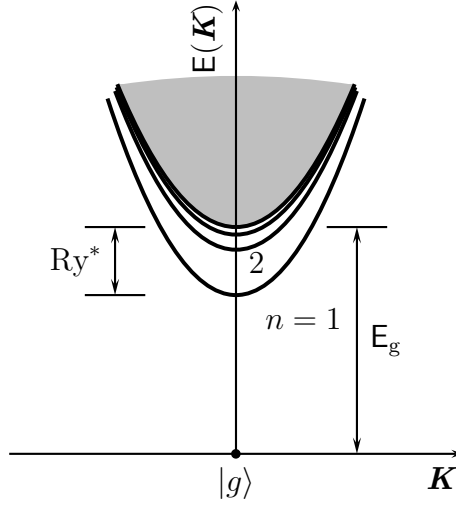


FIGURE 4. The energy bands of an exciton.

sections, these two kinds of excitons in the QWs further split into different energies. For each subband the excitons are quantized in the z direction with quantization energy $E_Q(n_z)$, the exciton energy can be described as [27]

$$\begin{aligned} E_{\text{x-2D}}(\mathbf{K}, n_z, n) &= E_g + E_Q(n_z) - Ry^* \frac{1}{(n - \frac{1}{2})^2} + \frac{\hbar^2 \mathbf{K}^2}{2M} \\ n_z &= 1, 2, 3 \dots, \quad n = 1, 2, 3 \dots \end{aligned} \quad (2.16)$$

The binding energy is found to be four times larger than the 3D case. The binding energy of excitons gives a Rydberg series of atomic-like resonance below the band gap. In this work only the $n = 1, n_z = 1$ HH exciton is studied.

In the low excitation density regime, the HH excitons in GaAs QWs can be modeled as a non-interacting atomic-like system. However due to the large Bohr radius of excitons, the wavefunctions of excitons begin to overlap at intermediate

excitation density. The interactions of excitons promote the nonlinearities of the system. For this reason an significant optical nonlinear process emerge at a much lower light field intensity compared to atomic systems. An important impact of these many-particle interactions in the electron-hole pair system of semiconductors is the formation of two-exciton states, which is to be discussed in the next section and also through the major parts of this thesis.

Biexciton and Two-Exciton States

Much alike hydrogen atoms forming a hydrogen molecule, in an excitonic system, Coulomb interactions between excitons can lead to the formation of bound or unbound two-exciton state. These two-exciton states play a central role in coherent nonlinear optical processes associated directly with the excitonic coherence [22, 32–34].

A biexciton (BX or X_2) can be considered as an excitonic molecule. It consists of two electrons and two holes, or two excitons. By forming a bound state, a biexciton resonance occurs at the lower energy side of the exciton resonance by a binding energy E_{BX} . One important property of the biexciton is that the two electrons (holes) are of opposite spin.

Two electron-hole pairs can also form unbounded two-exciton states. The study of the effects of the bound and unbound two-exciton states in the third-order

optical response is especially interesting in GaAs system. A phenomenological N -exciton model can be used to describe the interactions between the excitons. For the HH transition exciton can be labeled with electron spin. An N -exciton energy eigenstates diagram for HH thus can be draw as in Fig. 5. In this diagram the other two dark exciton states $|\pm 2\rangle = |\pm 3/2, \pm 1/2\rangle$ are not included since the transition from ground state to them are optically forbidden.

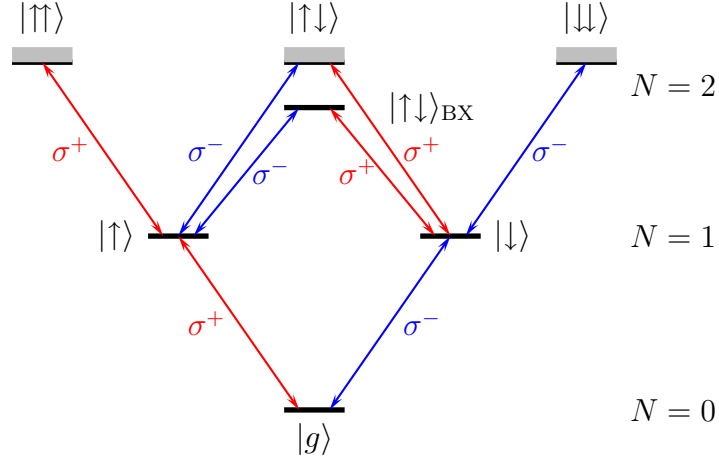


FIGURE 5. Schematic of N -exciton states for HH excitons. The ground state is labeled by $|g\rangle$. The one-exciton states are labeled by the electron spins. The two-exciton states include a bound biexciton state and three unbound two-exciton continuum states, labeled by the paired electron spins.

We choose the energy of $|g\rangle$ to be zero. The $N = 1$ subspace is the one-exciton subspace. A circularly polarized σ^+ (σ^-) photon couples the ground zero exciton state to $|+1\rangle$ ($|-1\rangle$) exciton. The $N = 2$ subspace is the two-exciton subspace, where the biexciton can be formed by two opposite circularly polarized photons. Note that in biexciton the two hole spins are also opposite from each other. The formation

of bound biexciton state can induce an absorption resonance in the DA spectra, as shown later. The nonlinearities arising from biexcitons are also significant. With the same or slightly higher resonance energy, the contributions from unbound two exciton states are also shown to be important.

Summary

In this chapter we reviewed some basic concepts used in this thesis. The excitonic transitions dominate the band to band transitions in semiconductors. The HH exciton transition in GaAs QWs are of special interest to this dissertation, because of the well-defined optical selection rules of coupling optical field with the electron spin states in the conduction band.

CHAPTER III

ELECTRON SPIN COHERENCE IN GaAs QUANTUM WELLS

This chapter is aimed to cover a brief review and a basic theoretical model on the understanding of the nonlinear response from electron spin coherence.

Electron Spin Coherence Through Optical Excitation

A quantum coherence can be initialized via a dipole allowed transition of a two level atom, where a monochromatic electromagnetic wave $E \cos(\nu t)$ can create a so-called dipole coherence between the ground state and the excited state, as shown in Fig. 6. The two level atom thus can then be written in a superposition state of

$$|\psi\rangle = c_g(t)|g\rangle + c_e(t)|e\rangle \quad (3.1)$$

It is well known that the probability of finding the atom in the excited state is $|c_e(t)|^2 = \cos^2(\bar{\Omega}t)$, where $\bar{\Omega} = \sqrt{\delta^2 + \Omega^2}$ is the generalized Rabi frequency (assuming the electron is initially in the excited state). It is so called Rabi Oscillation. $\Omega = \mu E/\hbar$

is the Rabi frequency, where μ is the dipole moment between the two levels, $\delta = \nu - \omega$ is the detuning between the optical frequency ν and the transition frequency ω .

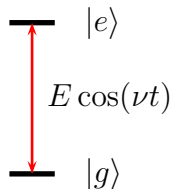


FIGURE 6. Dipole coherence in two-level system.

If we can use spin state to label these two eigenstates, the coherence therein can be called spin coherence. The spin coherence can be induced by dipole coupling of two spin states to a common ground state (a V-type three-level system) or to a common excited state (a Λ -type three-level system), as shown in Fig. 7, where the spin coherence corresponds to a state of spin superposition

$$|\psi\rangle = c_{\uparrow}|\uparrow\rangle + c_{\downarrow}|\downarrow\rangle \quad (3.2)$$

or an off-diagonal density matrix element $\rho_{\uparrow\downarrow}$. (See in the following sections in this chapter.)

An example of spin coherence is an electron with spin aligned in z direction subjected to a transverse magnetic field, say in x direction. In classical picture this spin will undergo a Larmor precession along x direction. The spin projection in the z direction produces a cosine oscillating amplitude as a function of time. The classical Larmor spin precession model is illustrated in Fig. 8.

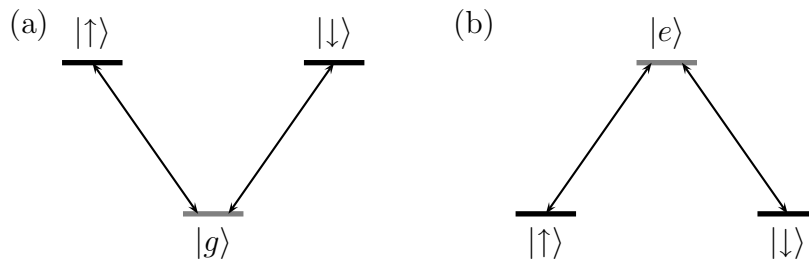


FIGURE 7. Excitation of spin coherence through two dipole allowed transitions: (a) a V-type three-level system; (b) a Λ -type three-level system.

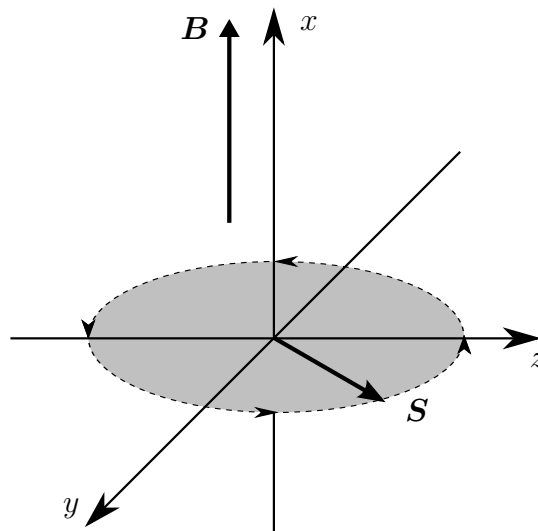


FIGURE 8. A classical Larmor spin precession model. Assume the total angular momentum \mathbf{S} only includes the electron spin aligned in z direction, while a magnetic field is in the x direction.

For a free electron, the magnetic moment is given by

$$\mathbf{M} = -g_e\mu_B\mathbf{S} \quad (3.3)$$

where $\mu_B = \frac{e\hbar}{2m_e}$ is the Bohr magneton, g_e is the free electron g -factor which is close to 2. The negative sign indicates the magnetic moment for an electron is antiparallel to the spin \mathbf{S} . The in-plane g -factor of the conduction band electrons of GaAs, however, is observed to be negative [35]. So in GaAs for electrons in the s -like conduction band, the magnetic moment actually is parallel to the electron spin.

The energy of a magnetic moment \mathbf{M} in a field \mathbf{B} is

$$E = -\mathbf{M} \cdot \mathbf{B}. \quad (3.4)$$

The classical Larmor precession is described by

$$\frac{d\mathbf{S}}{dt} = \mathbf{M} \times \mathbf{B}. \quad (3.5)$$

One can find the projection of \mathbf{M} along the z direction is

$$M_z = \cos \omega_L t, \quad (3.6)$$

where

$$\omega_L = g_e \mu_B B \quad (3.7)$$

is the precession Larmor frequency.

This spin precession can also be understood as a quantum coherence between the two spin states. The probability of finding the spin- z electron in the spin- x energy eigenstate is given by

$$\langle S_x | S_z \rangle = \cos \omega_L t \quad (3.8)$$

where the ω_L is given by the energy difference between the two spin- x eigenstates

$$\hbar\omega_L = \hbar\omega_+ - \hbar\omega_- \quad (3.9)$$

The direct way to polarize a spin particle in a given direction is by applying a constant magnetic field along that direction. But for the purpose of manipulating the precession, i.e. the coherence, optical techniques are preferred. For example, one can use circularly polarized light to inject electron spin of a certain orientation in semiconductors through optical absorption [9, 36]. Inducing electron spin coherence is also possible using similar approaches. For example, one can use a circularly polarized light to induce an electron spin coherence through the HH absorption of a GaAs QW in Voigt geometry external magnetic field.

GaAs QW Subject to an External Magnetic Field in Voigt Geometry

As shown in the Chapter II, a particularly interesting system for studying spin coherence is the HH transition in QWs, where due to the quantum confinement and the spin-orbital coupling the highest HH sub-band features well-defined spin symmetry. To induce electron spin coherence in the conduction band via HH transitions, the QW needs to be placed in an external magnetic field in Voigt geometry, where the magnetic field is parallel to the plane of the QW, orthogonal to the optical field propagation direction, as shown in Fig. 9. In this situation, a superposition state of two spin states can be generated by a circularly polarized optical field.

A quantum beats arises from the time evolution of the induced spin coherence. These quantum beats, combined with spin relaxation and dephasing processes, lead to damped oscillations in time-resolved photoluminescence, absorbance and circular polarization birefringence.

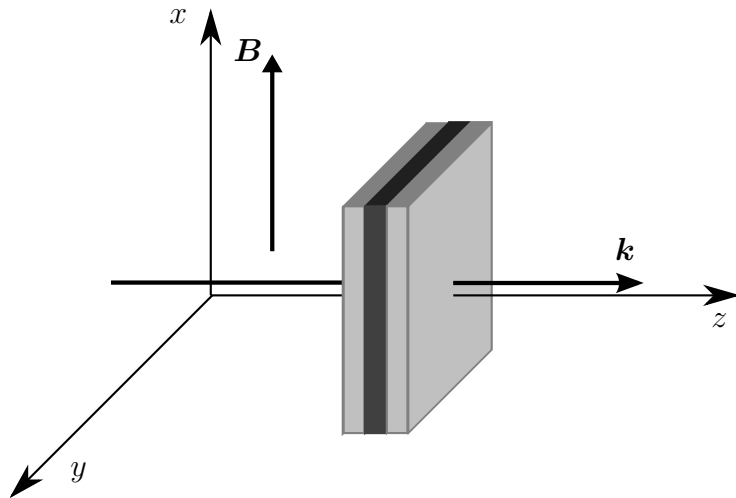


FIGURE 9. The Voigt geometry: the magnetic field is in the plan of the quantum well along the x -axis; the optical field \mathbf{k} is in the growth (001) direction of the quantum well along the z -axis.

As discussed in the last section, this quantum coherence can be classically understood in the picture of spin precession [14, 15]. The initialized spin-superposition state corresponds to a spin state which lies along the growth or the (001) direction, which is the direction of propagation for incident light. This spin or corresponding magnetization will precess when a magnetic field \mathbf{B} is applied perpendicular to the axis of spin orientation (transverse magnetic field). As shown later using

a perturbation calculation, the amplitude of beats should be proportional to the intensity of the pump.

The application of an external magnetic field along x -axis modifies the band structure by introducing a Zeeman energy splitting in the s -like conduction band. Thereby the degeneracy of the electron spin state is removed. The x direction becomes a quantization direction for the conduction electrons and s_x becomes a good quantum number.

The hole states with in-plane magnetic field is rather complicated [37, 38]. With a small field strength compared to the energy splitting of HH and LH, we can approximately still use J_z as a good quantum number, which means we can treat the electrons in the HH subbands still aligned along z direction.

The linear Zeeman Hamiltonian for the electron in the conduction band at low fields is given by

$$H_{Zeeman} = g_e \mu_B \mathbf{B} \cdot \mathbf{s} \quad (3.10)$$

The Zeeman splitting energy is given by

$$\Delta E_{Zeeman} = g_e \mu_B B = \frac{e\hbar}{2m_e} g_e B = \hbar \omega_L \quad (3.11)$$

For evaluation of non-vanishing dipole matrix elements between the HH valance band and the s -like conduction band, we express the conduction band states

in the spin- z basis, such that

$$|+1/2\rangle_x = \frac{1}{\sqrt{2}}(|+1/2\rangle_z + |-1/2\rangle_z) \quad (3.12)$$

$$|-1/2\rangle_x = \frac{1}{\sqrt{2}}(|+1/2\rangle_z - |-1/2\rangle_z) \quad (3.13)$$

The matrix element of dipole moment between conduction band states and HH valance band states are found in Table 2, where the $\hat{e}_x, \hat{e}_y, \hat{e}_z$ are the unit vectors in coordinates x, y, z .

TABLE 2. Matrix elements of dipole moment D_{cv}/D for HH transition under transverse magnetic field in Voigt geometry.

c	$\langle \frac{1}{2}, +\frac{1}{2} _x, \text{spin } \rightarrow$	$\langle \frac{1}{2}, -\frac{1}{2} _x, \text{spin } \leftarrow$
HH $ \frac{3}{2}, +\frac{3}{2}\rangle_z, \text{spin } \uparrow$	$-\frac{1}{2}(\hat{e}_x + i\hat{e}_y)$	$-\frac{1}{2}(\hat{e}_x + i\hat{e}_y)$
$ \frac{3}{2}, -\frac{3}{2}\rangle_z, \text{spin } \downarrow$	$\frac{1}{2}(\hat{e}_x - i\hat{e}_y)$	$-\frac{1}{2}(\hat{e}_x - i\hat{e}_y)$

We decompose the HH transition dipole moment into the circular polarization basis, such that

$$\boldsymbol{\mu} = \mu^+ \hat{e}_+ + \mu^- \hat{e}_- \quad (3.14)$$

where the circular base vectors can be written in the x and y base vectors

$$\text{Right-circularly polarized field: } \hat{e}_+ = \frac{1}{\sqrt{2}}(\hat{e}_x + i\hat{e}_y) \quad (3.15)$$

$$\text{Left-circularly polarized field: } \hat{e}_- = \frac{1}{\sqrt{2}}(\hat{e}_x - i\hat{e}_y) \quad (3.16)$$

A common dipole factor is defined as

$$\mu \equiv \frac{1}{2}D \quad (3.17)$$

The effect of modification on optical selection rules by the transverse external magnetic field for the HH transition is shown in Fig. 10. The conduction electron spin states are coupled to a common valance band state.

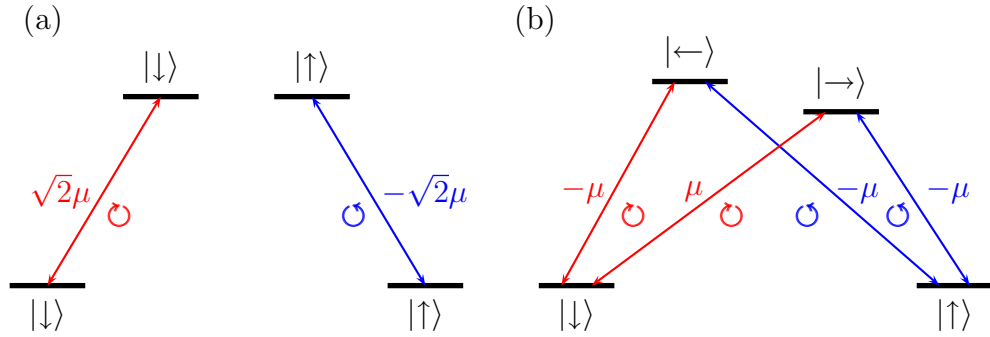


FIGURE 10. (a) Optical selection rules for HH transition of GaAs QW without magnetic field. (b) Optical selection rules for HH transition of GaAs QW subject to an external magnetic field in Voigt geometry. The states are labeled by electron spin.

In the experimental studies of spin coherence, if the spin decoherence time is long, as compared to the lifetime of carriers (the exciton recombination time), quantum beats can be observed in the time-resolved spontaneous fluorescence measurements. However, the spin decoherence time is not always comparable to, or longer than the lifetime of carriers. Thus, transient nonlinear optical spectra would be convenient to measure the spin precession. For a correct interpretation of nonlinear spectra of electron spins in semiconductors, it is important to study the nonlinear susceptibilities related to the electron spin coherence.

Nonlinear Optical Polarization

Within the scope of this dissertation, the optical field is described by classical Maxwell equations. The electrons and excitons in the semiconductor QWs are described using quantum density matrix formalism, which is described later.

The interaction between an electromagnetic field and macroscopic media can be described by Maxwell equations. Considering a nonmagnetic material contains no free charges and no free currents, for a transverse infinite plane wave field ($\nabla \cdot \mathbf{E} = 0$) one finds

$$\nabla^2 \mathbf{E} - \frac{1}{c^2} \frac{\partial^2 \mathbf{E}}{\partial t^2} = \frac{1}{c^2} \frac{\partial^2 \mathbf{P}}{\partial t^2} \quad (3.18)$$

The polarization \mathbf{P} can be split into its linear and nonlinear parts as

$$\mathbf{P} = \mathbf{P}^{(1)} + \mathbf{P}^{\text{NL}} \quad (3.19)$$

$\mathbf{P}^{(1)}$ is the part of \mathbf{P} that depends linearly on the electric field strength \mathbf{E} . Consider an anisotropic material with nonlinear responses to the electro-magnetic field, the i^{th} component of the polarization density \mathbf{P} , in general, is related to the components of the electric field \mathbf{E} according to

$$P_i/\epsilon_0 = \sum_j \chi_{ij}^{(1)} E_j + \sum_k \chi_{ijk}^{(2)} E_j E_k + \sum_{kl} \chi_{ijkl}^{(3)} E_j E_k E_l + \dots \quad (3.20)$$

To simplify our problem the material is treated as isotropic, such that the magnitude of the polarization density \mathbf{P} can be expressed as a power series in the

field strength E with a series of nonlinear electric susceptibility $\chi^{(n)}$ as

$$P = \chi^{(1)}E + \chi^{(2)}E^2 + \chi^{(3)}E^3 + \dots \quad (3.21)$$

With the semiclassical model and approximation outlined above, the electric field is described by Maxwell equations as a classical complex value. The dynamics of the system is calculated by solving the coupled equations of \mathbf{E} and \mathbf{P} .

The material can be modeled as a collection of well-isolated dipole molecules, i.e. without charge overlapping. In general, if the polarization of one dipole molecule subject to an electric field is \mathbf{P}_a , then the polarization is given by

$$\mathbf{P} = n_a \mathbf{P}_a \quad (3.22)$$

where n_a is the number density of the atoms in a unit volume of a material.

Quantum Beats from a Three-Level V System

In this section we will discuss how to describe the nonlinear optical signal in the transient pump-probe experiments. Our goal is to provide a semi-classical phenomenological model as a starting point to understand our experimental results.

Let's consider a three level system as shown in Fig. 11. In this V system a common ground state $|c\rangle$ is coupled with two non-degenerate excited upper states $|a\rangle$, and $|b\rangle$ with an optical field \mathbf{E} . The unperturbed Hamiltonian of this system can be

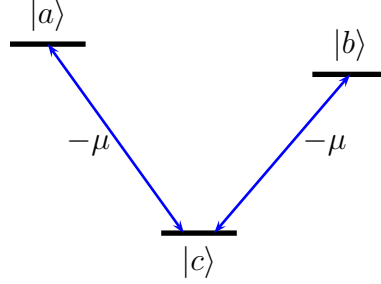


FIGURE 11. Energy diagram of a three-level V system.

written as

$$H_0 = \sum_n \hbar\omega_n |n\rangle\langle n| = \begin{pmatrix} \hbar\omega_a & 0 & 0 \\ 0 & \hbar\omega_b & 0 \\ 0 & 0 & \hbar\omega_c \end{pmatrix} \quad (3.23)$$

For convenience we can set the ground state energy to zero, i.e. $\omega_c = 0$.

Assume this three level system is coupled with a σ^- left-circular polarized monochromatic plane wave optical field,

$$\mathbf{E} = E(t)\hat{e}_- = \frac{1}{2} \left(\tilde{E}(t)e^{-i\omega t} + c.c. \right) \hat{e}_- \quad (3.24)$$

where

$$\tilde{E}(t) = \mathcal{E}(t)e^{i\mathbf{x}\cdot\mathbf{k}} \quad (3.25)$$

The $\tilde{E}(t)$ describes the slowly varying amplitudes of the electric fields. The $\mathcal{E}(t)$ is the time envelop of the electric fields amplitude (real).

The dipole matrix elements for the σ^- field is given by the selection rule. This V-type system is a sub system in the HH transition under the external magnetic field

of Voigt geometry, as shown in Fig. 10(b). For convenience the dipole matrix elements couple to the two upper states are taken to be equal and real. So

$$\mu^- = \begin{pmatrix} 0 & 0 & -\mu \\ 0 & 0 & -\mu \\ -\mu & -\mu & 0 \end{pmatrix} \quad (3.26)$$

Thus the Hamiltonian of this system can be written as

$$H = H_0 + H' = H_0 - \boldsymbol{\mu} \cdot \mathbf{E} = \begin{pmatrix} \hbar\omega_a & 0 & \mu E(t) \\ 0 & \hbar\omega_b & \mu E(t) \\ \mu E(t) & \mu E(t) & 0 \end{pmatrix} \quad (3.27)$$

The density matrix used to describe the three-level system is:

$$\rho = \sum_{i,j} \rho_{ij} |i\rangle\langle j| = \begin{pmatrix} \rho_{aa} & \rho_{ab} & \rho_{ac} \\ \rho_{ba} & \rho_{bb} & \rho_{bc} \\ \rho_{ca} & \rho_{cb} & \rho_{cc} \end{pmatrix} \quad (3.28)$$

The diagonal matrix elements ρ_{aa} , ρ_{bb} and ρ_{cc} gives the populations of levels $|a\rangle$, $|b\rangle$ and $|c\rangle$, respectively. We assume a closed system, such that

$$\rho_{aa} + \rho_{bb} + \rho_{cc} = 1 \quad (3.29)$$

The off-diagonal elements $\rho_{ac} = \rho_{ca}^*$ and $\rho_{bc} = \rho_{cb}^*$ describe the dipole coherence from the dipole allowed transitions. The off-diagonal element $\rho_{ab} = \rho_{ba}^*$ describe the

nonradiative Raman coherence. If $|a\rangle$ and $|b\rangle$ stand for the two spin state, then ρ_{ab} describes the spin coherence.

By using the density matrix equation

$$\frac{d}{dt}\rho = \dot{\rho} = \frac{i}{\hbar} [\rho, H] = \frac{i}{\hbar} (\rho H - H\rho) \quad (3.30)$$

We can obtain a set of differential equations:

$$\dot{\rho}_{aa}(t) = -\frac{i\mu E(t)}{\hbar} (\rho_{ac} - \rho_{ac}^*) \quad (3.31)$$

$$\dot{\rho}_{bb}(t) = -\frac{i\mu E(t)}{\hbar} (\rho_{bc} - \rho_{bc}^*) \quad (3.32)$$

$$\begin{aligned} \dot{\rho}_{ac}(t) &= -i\omega_a \rho_{ac} - \frac{i\mu E(t)}{\hbar} (\rho_{aa} - \rho_{cc} + \rho_{ab}) \\ &= -i\omega_a \rho_{ac} - \frac{i\mu E(t)}{\hbar} (2\rho_{aa} + \rho_{bb} + \rho_{ab} - 1) \end{aligned} \quad (3.33)$$

$$\begin{aligned} \dot{\rho}_{bc}(t) &= -i\omega_b \rho_{bc} - \frac{i\mu E(t)}{\hbar} (\rho_{bb} - \rho_{cc} + \rho_{ba}) \\ &= -i\omega_b \rho_{bc} - \frac{i\mu E(t)}{\hbar} (2\rho_{bb} + \rho_{aa} + \rho_{ab}^* - 1) \end{aligned} \quad (3.34)$$

$$\dot{\rho}_{ab}(t) = -i(\omega_a - \omega_b) \rho_{ab} + \frac{i\mu E(t)}{\hbar} (\rho_{bc}^* - \rho_{ac}) \quad (3.35)$$

We can define

$$\omega_L \equiv \omega_a - \omega_b = \frac{\Delta E_{Zeeman}}{\hbar} \quad (3.36)$$

$$\delta_a \equiv \nu - \omega_a \quad (3.37)$$

$$\delta_b \equiv \nu - \omega_b = \delta_a + \omega_L \quad (3.38)$$

where ω_L is the Larmor frequency proportional to the Zeeman splitting energy, δ_a and δ_b is the detuning of the optical field frequency to the transition frequencies.

We make the substitutions

$$\rho_{ac} = \tilde{\rho}_{ac} e^{-i\nu t} \quad (3.39)$$

$$\rho_{bc} = \tilde{\rho}_{bc} e^{-i\nu t} \quad (3.40)$$

to factor out the rapidly varying components which oscillate at the optical frequency.

We introduce the Rabi frequency Ω of the optical field as

$$\Omega(t) = \frac{\mu \tilde{E}(t)}{\hbar} \quad (3.41)$$

For our experiments we only consider a nearly-resonance condition, where detuning between the optical field frequency ν and the exciton transition resonance frequency ω_a and ω_b is small. Assuming that $|\nu - \omega_{a,b}| \ll \nu + \omega_{a,b}$, we can make the rotating-wave approximation (RWA). Physically this approximation is valid because during the interaction time of about 5 ps, the contribution of fast oscillating part (on femto-second (fs) time scales) averages out to nearly vanish.

Finally we add phenomenological population decay terms Γ_a and Γ_b as well as dephasing terms γ_a , γ_b and γ_{ab} in this system. After all above modifications, we arrive at a set of optical Bloch equations (OBE):

$$\dot{\rho}_{aa} = -\Gamma_a \rho_{aa} - \frac{i}{2} (\Omega^* \tilde{\rho}_{ac} - c.c.) \quad (3.42)$$

$$\dot{\rho}_{bb} = -\Gamma_b \rho_{bb} - \frac{i}{2} (\Omega^* \tilde{\rho}_{bc} - c.c.) \quad (3.43)$$

$$\dot{\tilde{\rho}}_{ac} = (i\delta_a - \gamma_a) \tilde{\rho}_{ac} - \frac{i}{2} \Omega (2\rho_{aa} + \rho_{bb} + \rho_{ab} - 1) \quad (3.44)$$

$$\dot{\tilde{\rho}}_{bc} = (i\delta_b - \gamma_b) \tilde{\rho}_{bc} - \frac{i}{2} \Omega (2\rho_{bb} + \rho_{aa} + \rho_{ab}^* - 1) \quad (3.45)$$

$$\dot{\rho}_{ab} = -(i\omega_L + \gamma_{ab}) \rho_{ab} - \frac{i}{2} (\Omega^* \tilde{\rho}_{ac} - \Omega \tilde{\rho}_{bc}^*) \quad (3.46)$$

Solving these differential equations gives us the time evolution of the three-level V system. Now let's use an order by order perturbation approximation method in the expansion of optical fields.

$$\rho = \rho^{(0)} + \rho^{(1)} + \rho^{(2)} + \rho^{(3)} + \dots \quad (3.47)$$

We need to evaluate $\rho^{(n)}$ from $n = 0$ zero order, to the $n = 3$ third order, by

solving the following equations:

$$\dot{\rho}_{aa}^{(n+1)} = -\Gamma_a \rho_{aa}^{(n+1)} - \frac{i}{2} (\Omega^* \tilde{\rho}_{ac}^{(n)} - c.c.) \quad (3.48)$$

$$\dot{\rho}_{bb}^{(n+1)} = -\Gamma_b \rho_{bb}^{(n+1)} - \frac{i}{2} (\Omega^* \tilde{\rho}_{bc}^{(n)} - c.c.) \quad (3.49)$$

$$\dot{\tilde{\rho}}_{ac}^{(n+1)} = (i\delta_a - \gamma_a) \tilde{\rho}_{ac}^{(n+1)} - \frac{i}{2} \Omega \left(2\rho_{aa}^{(n)} + \rho_{bb}^{(n)} + \rho_{ab}^{(n)} - 1 \right) \quad (3.50)$$

$$\dot{\tilde{\rho}}_{bc}^{(n+1)} = (i\delta_b - \gamma_b) \tilde{\rho}_{bc}^{(n+1)} - \frac{i}{2} \Omega \left(2\rho_{bb}^{(n)} + \rho_{aa}^{(n)} + \rho_{ab}^{*(n)} - 1 \right) \quad (3.51)$$

$$\dot{\rho}_{ab}^{(n+1)} = -(i\omega_L + \gamma_{ab}) \rho_{ab}^{(n+1)} - \frac{i}{2} (\Omega^* \tilde{\rho}_{ac}^{(n)} - \Omega \tilde{\rho}_{bc}^{*(n)}) \quad (3.52)$$

After we have the $\rho^{(n)}$, we will be able to evaluate the nonlinear polarization due to the optical fields, and in turn get the nonlinear optical responses of this system.

The n th order polarization can be evaluated by

$$P^{(n)} \hat{e}_- = N \text{Tr} (\rho^{(n)} \mu^-) \hat{e}_- \quad (3.53)$$

where N is the number density of the material.

We assume the system initially is in the ground state $|c\rangle$, all density matrix elements vanish at zero order except that

$$\rho_{cc}^{(0)} = 1 \quad (3.54)$$

It is easy to see that the first order terms are given by

$$\dot{\rho}_{aa}^{(1)} = -\Gamma_a \rho_{aa}^{(1)} \quad (3.55)$$

$$\dot{\rho}_{bb}^{(1)} = -\Gamma_b \rho_{bb}^{(1)} \quad (3.56)$$

$$\dot{\tilde{\rho}}_{ac}^{(1)} = (i\delta_a - \gamma_a) \tilde{\rho}_{ac}^{(1)} + \frac{i}{2} \Omega \quad (3.57)$$

$$\dot{\tilde{\rho}}_{bc}^{(1)} = (i\delta_b - \gamma_b) \tilde{\rho}_{bc}^{(1)} + \frac{i}{2} \Omega \quad (3.58)$$

$$\dot{\rho}_{ab}^{(1)} = -(i\omega_L + \gamma_{ab}) \rho_{ab}^{(1)} \quad (3.59)$$

To obtain an analytical solution we assume a delta pulse field ($\mathcal{E}(t) = \delta(t)$) interacting with the system at $t = 0$, such that

$$\Omega = \Omega_0 \delta(t) \quad (3.60)$$

The solutions for the first order are

$$\rho_{aa}^{(1)} = 0 \quad (3.61)$$

$$\rho_{bb}^{(1)} = 0 \quad (3.62)$$

$$\tilde{\rho}_{ac}^{(1)} = \frac{i}{2} \Omega_0 \Theta(t) e^{(i\delta_a - \gamma_a)t} \quad (3.63)$$

$$\tilde{\rho}_{bc}^{(1)} = \frac{i}{2} \Omega_0 \Theta(t) e^{(i\delta_b - \gamma_b)t} \quad (3.64)$$

$$\rho_{ab}^{(1)} = 0 \quad (3.65)$$

where $\Theta(t)$ is the Heavyside step function. The non-vanishing first order terms $\tilde{\rho}_{ac}^{(1)}$ and $\tilde{\rho}_{bc}^{(1)}$ give the linear dipole polarization response of the system. It dephases quite fast as the dipole dephasing rates $\gamma_{a,b}$ are very large. In fact, the dipole dephasing time

$$T_{da} = \frac{1}{\gamma_a}, \quad T_{db} = \frac{1}{\gamma_b}, \quad (3.66)$$

is generally within 10 ps.

As we proceed to the second order, after substituting in the first order solutions we find the equations for the second order density matrix are

$$\dot{\rho}_{aa}^{(2)} = -\Gamma_a \rho_{aa}^{(2)} - \frac{i}{2} (\Omega^* \tilde{\rho}_{ac}^{(1)} - c.c.) = -\Gamma_a \rho_{aa}^{(2)} + \frac{\Omega_0^2}{2} \delta(0) \quad (3.67)$$

$$\dot{\rho}_{bb}^{(2)} = -\Gamma_b \rho_{bb}^{(2)} - \frac{i}{2} (\Omega^* \tilde{\rho}_{bc}^{(1)} - c.c.) = -\Gamma_b \rho_{bb}^{(2)} + \frac{\Omega_0^2}{2} \delta(0) \quad (3.68)$$

$$\dot{\tilde{\rho}}_{ac}^{(2)} = (i\delta_a - \gamma_a) \tilde{\rho}_{ac}^{(2)} \quad (3.69)$$

$$\dot{\tilde{\rho}}_{bc}^{(2)} = (i\delta_b - \gamma_b) \tilde{\rho}_{bc}^{(2)} \quad (3.70)$$

$$\dot{\rho}_{ab}^{(2)} = -(i\omega_L + \gamma_{ab}) \rho_{ab}^{(2)} - \frac{i}{2} (\Omega^* \tilde{\rho}_{ac}^{(1)} - \Omega \tilde{\rho}_{bc}^{*(1)}) \quad (3.71)$$

we have the second order solutions

$$\rho_{aa}^{(2)} = \frac{1}{2}\Omega_0^2\Theta(t)e^{-\Gamma_a t} \quad (3.72)$$

$$\rho_{bb}^{(2)} = \frac{1}{2}\Omega_0^2\Theta(t)e^{-\Gamma_b t} \quad (3.73)$$

$$\tilde{\rho}_{ac}^{(2)} = 0 \quad (3.74)$$

$$\tilde{\rho}_{bc}^{(2)} = 0 \quad (3.75)$$

$$\rho_{ab}^{(2)} = \frac{1}{2}\Omega_0^2\Theta(t)e^{-i\omega_L t}e^{-\gamma_{ab} t} \quad (3.76)$$

So we obtained a spin coherence term $\rho_{ab}^{(2)}$ which oscillates at the frequency of ω_L in the second order. We also see the population decay back to the ground state $|c\rangle$ after the stimulated absorption at $t = 0$.

Similarly it can be shown, for a σ^+ coupled sub three-level system, to the second order the population density matrix elements are in the same forms, but the spin coherence elements are oscillating at an opposite phase:

$$\rho_{ab}^{(2)} = \frac{1}{2}\Omega_0^2\Theta(t)e^{i\omega_L t}e^{-\gamma_{ab} t}. \quad (3.77)$$

Measurements of Spin Coherence

To measure the spin coherence, we add a measurement field $\Omega_1\delta(\tau)$ (the probe field) with the same polarization, and same frequency but different field amplitude

Ω_1 . We assume a large delay

$$\tau \gg T_{da}, \tau \gg T_{db}. \quad (3.78)$$

such that all dipole coherence from pump field are dephased and we can take

$$\tilde{\rho}_{ac}^{(2)}(\tau) \simeq 0 \quad (3.79)$$

$$\tilde{\rho}_{bc}^{(2)}(\tau) \simeq 0 \quad (3.80)$$

Assume a long lived spin coherence time (a small γ_{ab}), which is the case for the experiment, include this probe field and calculate the third order density matrix from equations for $t = \tau$:

$$\dot{\rho}_{aa}^{(3)}|_{t=\tau} = -\Gamma_a \rho_{aa}^{(3)}(\tau) \quad (3.81)$$

$$\dot{\rho}_{bb}^{(3)}|_{t=\tau} = -\Gamma_b \rho_{bb}^{(3)}(\tau) \quad (3.82)$$

$$\dot{\rho}_{ac}^{(3)}|_{t=\tau} = (i\delta_a - \gamma_a) \tilde{\rho}_{ac}^{(3)}(\tau) - \frac{i}{2} \Omega_1 \left(2\rho_{aa}^{(2)}(\tau) + \rho_{bb}^{(2)}(\tau) + \rho_{ab}^{(2)}(\tau) \right) \quad (3.83)$$

$$\dot{\rho}_{bc}^{(3)}|_{t=\tau} = (i\delta_b - \gamma_b) \tilde{\rho}_{bc}^{(3)}(\tau) - \frac{i}{2} \Omega_1 \left(2\rho_{bb}^{(2)}(\tau) + \rho_{aa}^{(2)}(\tau) + \rho_{ab}^{*(2)}(\tau) \right) \quad (3.84)$$

$$\dot{\rho}_{ab}^{(3)}|_{t=\tau} = -(i\omega_L + \gamma_{ab}) \rho_{ab}^{(3)}(\tau) \quad (3.85)$$

We can obtain the solution for the $\rho^{(3)}(\tau)$

$$\rho_{aa}^{(3)}(\tau) = 0 \quad (3.86)$$

$$\rho_{bb}^{(3)}(\tau) = 0 \quad (3.87)$$

$$\tilde{\rho}_{ac}^{(3)}(\tau) = -\frac{i}{4}\Omega_0^2\Omega_1 (2e^{-\Gamma_a\tau} + e^{-\Gamma_b\tau} + e^{-\gamma_{ab}\tau}e^{-i\omega_L\tau}) \quad (3.88)$$

$$\tilde{\rho}_{bc}^{(3)}(\tau) = -\frac{i}{4}\Omega_0^2\Omega_1 (2e^{-\Gamma_b\tau} + e^{-\Gamma_a\tau} + e^{-\gamma_{ab}\tau}e^{i\omega_L\tau}) \quad (3.89)$$

$$\rho_{ab}^{(3)}(\tau) = 0 \quad (3.90)$$

Here we only consider the detection of the mixed field in the direction of the probe optical field. Converting the slow-varying $\tilde{\rho}_{ac}$ and $\tilde{\rho}_{bc}$ back with Eqns. (3.39) and (3.40) one obtains the third order polarization as

$$\begin{aligned} P^{(3)}\hat{e}_- &= N\text{Tr}(\rho^{(3)}\mu^-)\hat{e}_- \quad (3.91) \\ &= -N\mu\left(\rho_{ac}^{(3)} + \rho_{bc}^{(3)}\right)\hat{e}_- + c.c. \\ &= \mathbf{P}_- + \mathbf{P}_-^* \end{aligned}$$

where

$$\mathbf{P}_- = \frac{i}{4}N\mu\Omega_0^2\Omega_1 (3e^{-\Gamma_a\tau} + 3e^{-\Gamma_b\tau} + e^{-\gamma_{ab}\tau} \cos(\omega_L\tau)) e^{-i\nu\tau}\hat{e}_- \quad (3.92)$$

Quantum beats in the polarization can be clearly seen from the third term. The electromagnetic field from this polarization further mixes with the probe field and is

detected in the far field. The differential transmission signal at a large pump-probe delay τ is given by

$$\begin{aligned}
 DT &\sim \int dt (|E_1 + iP_-|^2 - |E_1|^2) \\
 &\sim \text{Im} \int dt E_1^* P_- \\
 &\sim \Omega_0^2 \Omega_1^2 (6e^{-\Gamma\tau} + e^{-\gamma_{ab}\tau} \cos(\omega_L\tau))
 \end{aligned} \tag{3.93}$$

Where $\Gamma_a = \Gamma_b = \Gamma$ is assumed.

From Eqn. (3.93) it can be seen that the DT quantum beats amplitude scales linearly to the pump and probe intensity. However, looking closely one finds the pure imaginary third order polarization result from the delta pulse indicate that there are no refractive index change induced by the pump, which is not the case in the real TRFR measurements. To account for this reality, we have to consider the optical pulse with a finite duration and a finite band width in frequency domain. However this correction makes the analytical calculation very difficult. Thus, a numerical integration is used to calculate the coupled differential equations [39]. By using numerical simulation a responses as a function of detuning can also be obtained.

Figure 12 presents a numerical integration result using a finite pulse width of 5 ps in time domain, for both pump and probe field, to the third order of the applied fields. The average transition frequency of two dipole transitions is set to 375 THz. A equal dipole dephasing rate of 0.2 THz is assumed for both

transitions. A Larmor precession period of 69.8 ps is used, together with a spin dephasing time of 320 ps, according to the results of experimental observations. An exciton lifetime of 1 ns is assumed. Both transient DA ($\Delta T/T$) and TRFR responses are calculated. The details about DA and TRFR measurements is presented in Chapter IV. The amplitudes of quantum beats indicated in the right column of graphs are the amplitude of the spin beats contribution at the zero pump probe delay, A_T and A_θ , which are defined later in Eqn. (7.3) and Eqn. (5.2), respectively.

Manybody Effects Corrections

Previous discussions did not include the interactions between the excitons. As introduced in Chapter II, the manybody interactions plays crucial roles in the optical responses of semiconductors. First, the valance band hole relaxation is very efficient and fast, even under low temperature. Hence the sub three-level system can not be treated as a closed system. For this study both hole states can be considered as equally populated at a long delay after the excitation of pump. Secondly, the formation of two-exciton states actually provides other pathways to the coupling of spin coherence towards the material nonlinear polarizations. The details of these coupling effects on the responses of the DA and TRFR measurements will be discussed in the following chapters.

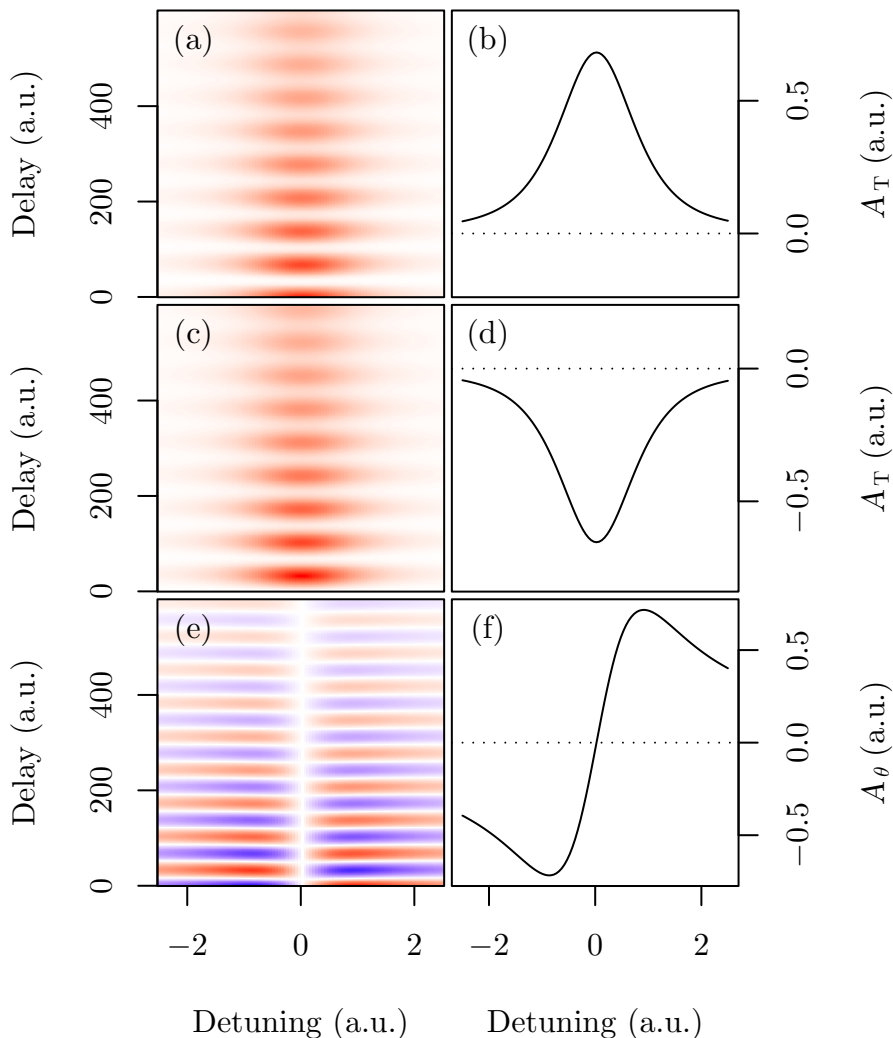


FIGURE 12. Numerical simulation results of DA and TRFR measurements. Red color indicates a positive signal. Blue color indicates a negative signal. Pump is fixed at the HH absorption transition center. Probe is detuned from the pump. (a) DA response from co-circularly polarized pump and probe. (b) Absorption spin quantum beats amplitude spectrum from co-circularly polarized pump and probe. (c) DA response from counter-circularly polarized pump and probe. (d) Absorption spin quantum beats amplitude spectrum from counter-circularly polarized pump and probe. (e) Two-color TRFR response. (f) Polarization rotation spin quantum beats amplitude spectrum.

Summary

In this chapter we discussed how an electron spin coherence/precession associated with HH transitions can be induced in a GaAs QW. This spin coherence/precession creates an oscillating nonlinear polarization and thus can be observed in the transient nonlinear DA and TRFR experiments. The phenomenological atomic-like non-interacting three-level model gives a general idea about the nonlinear response associated with electron spin coherence through the calculation by density matrix formalism. However the manybody interactions in semiconductors are so important that in real nonlinear optical measurements the contributions from two-exciton states can not be ignored. The roles of two-exciton states will be discussed in Chapter VIII.

CHAPTER IV

SAMPLES AND EXPERIMENTAL TECHNIQUES

This chapter presents the features of the time-domain experimental setup and samples used in this dissertation.

Semiconductor QW Samples

In this electron spin coherence study, primarily three different high quality QWs samples had been used.

Sample A is a high quality undoped (001) single QW grown by molecular beam epitaxy (MBE). It contains 1 period of 17.5 nm GaAs wells and 15 nm $\text{Al}_{0.3}\text{Ga}_{0.7}\text{As}$ barriers. Its absorption spectrum at 10 K is shown in Fig. 13.

Sample B is a high quality undoped (001) GaAs multi-QWs sample contains 15 periods of 13 nm GaAs wells and 15 nm $\text{Al}_{0.3}\text{Ga}_{0.7}\text{As}$ barriers. Its absorption spectrum at 10 K is shown in Fig. 14.

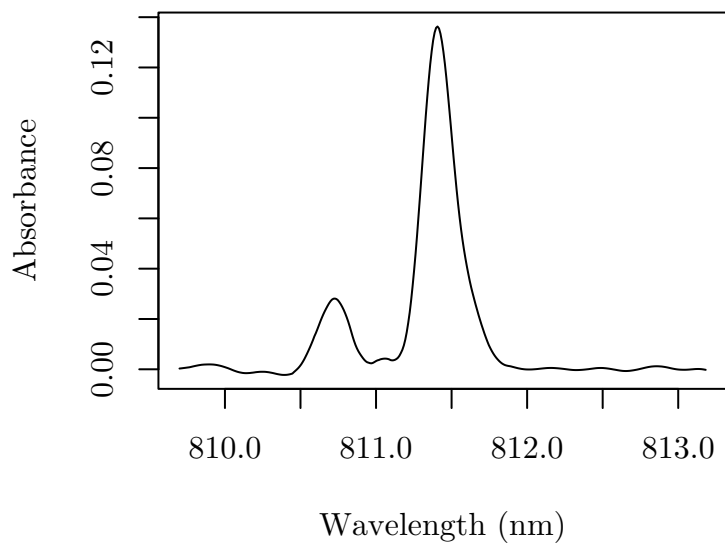


FIGURE 13. Linear absorption spectrum for a 17.5 nm GaAs SQW (sample A) at 10 K.

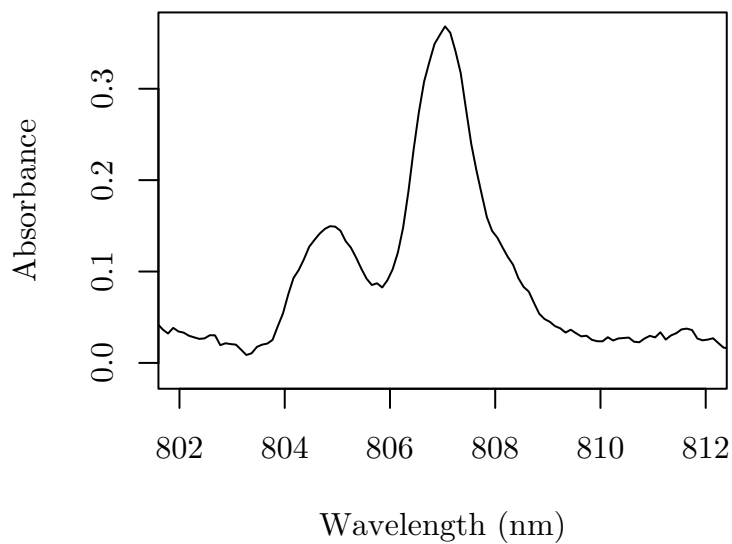


FIGURE 14. Linear absorption spectrum for a 13.0 nm GaAs MQW (sample B) at 10 K.

The sample C is a high quality undoped (001) multi InGaAs QWs grown by MBE. It contains 10 periods of 8 nm $\text{In}_{0.04}\text{Ga}_{0.96}\text{As}$ wells and 230 nm GaAs barriers. This sample features an isolated HH resonance far apart from other excitonic transitions, as shown in Fig. 15. It was provided by H.M. Gibbs group at the University of Arizona.

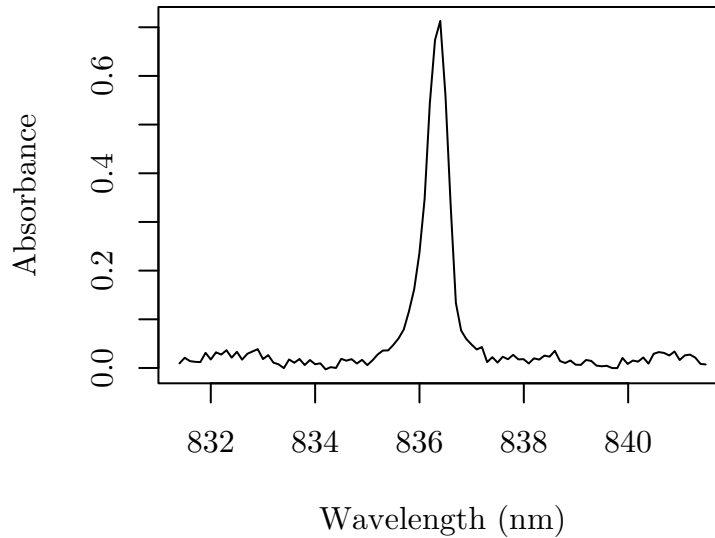


FIGURE 15. Linear absorption spectrum for an 8 nm InGaAs MQW (sample C) at 10 K.

These QWs samples were mounted on *c*-axis normal sapphire discs. This is important for polarization sensitive measurements such as TRFR, because the polarization of light field at nearly normal incidence is preserved. The substrates of QW were removed by first mechanical lapping and then using selective chemical etching to allow transparent measurement. The semiconductor QWs were placed in

a transverse external magnetic field (Voigt geometry), to allow optical initialization of electron spin coherence.

Laser System

The laser system used for these experiments consisted of a mode-locked Ti:sapphire laser (Spectra-Physics Tsunami) pumped by a 10 W laser (Coherent Verdi V-10) at 532 nm. The Ti:sapphire laser was typically run at a spectral bandwidth of $7 \sim 8$ nm, and deliver a mode-locked pulse with duration of 150 fs. The pulse repetition rate was 82 MHz. For 7 W input pump power, the average output power from the Ti:sapphire was approximately 1W at 807 nm.

The output from the Ti:sapphire laser was linearly polarized. Zeroth-order quartz half wave plates (HWP) were used to rotate the polarization into desired direction. Circular polarizations of the pump and probe (also including a control beam in three-pulse experiments) were generated using zeroth-order quartz quarter wave plates (QWP), optimized for use at 830 nm. By properly adjusting the QWPs, the polarizations could be made right-circular (σ^+ or \odot) or left-circular (σ^- or \ominus). Variations from optimized circular polarization were less than 5%.

External Pulse Shaper

An ultrafast time-resolved optical technique often sacrifices the spectral resolving power for the time domain resolution. For a system evolves with slow time variation signature, one can have a trade-off, i.e., obtain a limited spectral resolution and maintain a limited time resolution at the same time. One can use a pulse with the spectral-width just narrow enough to resolve and distinguish the interested resonances of the system, while the finite time duration of the pulse still provide the ability to study the time evolution dynamics at different detuning between the optical field and the transition frequency. A convenient way to achieve this experimentally is to use external pulse shaper on fs pulses to deliver ps pulses.

For our experiments, the ultra-fast pulses generated from the Tsunami Ti:sapphire mode-locked laser system are transform limited. But the spectral linewidth ($7 \sim 8\text{nm}$) is too large to spectrally resolve closely spaced optical transitions, for example, the localized exciton and the mobile exciton, the exciton and biexciton, etc. To obtain spectrally narrow pulses needed for the experiments, this dissertation used two external pulse shapers to provide independently re-shaped and tunable pump and probe pulses.

The external pulse shapers are based on a design by David Alavi. Each pulse shaper consisted of a Spectrogon gold coated blazed grating at near infrared with

1200 lines/mm, a high power bi-convex 300 mm focusing lens, a slit (with both the width and lateral location can be adjusted), and a mirror, as shown in Fig. 16.

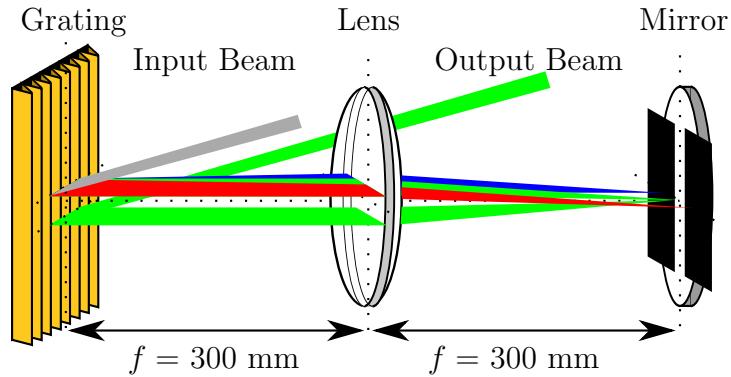


FIGURE 16. Schematic of the pulse shaper apparatus.

The input beam is diffracted from the grating to spatially separate its frequency components. The angle of incidence measured with respect to grating normal should be more than 60 degree to achieve a full cover of the input beam over the grating lines. The first order diffracted beam is focused onto a mirror, with the lens placed one focal length from the grating and one focal length from the mirror, so that each frequency is focused to a resolution limited point in the rear focal plane on the mirror. A small vertical shift of the input beam from the optical axis of the lens is introduced, and the mirror is adjusted such that the reflected output beam is shift at the same amount opposite to the optical axis on the grating. In such a way the incident and the filtered beams could be spatially separated. A vertical slit is made

with two razor blades and is placed close to the mirror to select the desired spectral bandwidth of the pulses. The slit is adjustable in position and width, and functions as a spatial filter. After reflecting off the mirror, the remaining spectral components of the beam return through the lens to the grating where they are recombined and an shaped pulse beam output is returned in the same but slightly vertically shifted direction as the incident beam.

Proper alignment and adjustment of the pulse shaper is important to avoid pulse broadening due to differing path lengths of the spatially separated spectral components and pulse chirping. By adjusting the relative distances between the grating, lens, and mirror, nearly Fourier-transform limited pulses could be obtained. This is verified by measuring the spectral bandwidth using a spectrometer and the temporal width using autocorrelation or cross-correlation techniques. The minimum filtered spectral bandwidth obtained with this setup is approximately 0.2 nm. Attempting to close the slit further results in an increase in spectral bandwidth due to spatial diffraction from the slit. For most of the experiments presented in this dissertation, spectral width of the pump was about 0.3 nm, with pulse duration of 6 ps \sim 7 ps, as measured by cross-correlation with the probe pulse.

Super-Conducting Magnetic System

In most of our studies we used external magnetic field to modify the energy level structures of the exciton levels.

Some preliminary studies were carried out in a small Janis cryostat by attaching a 1-inch diameter permanent magnet with B up to 0.5 T (Tesla). The small magnet was appropriately oriented to the sample holder on cold finger. The distance from probe spot to the small magnet was used to estimate the strength of the magnetic field. Spin quantum beats from electron spin coherence was observed in time-domain pump-probe experiments. However because the field strength is not easy to control, also due to the small electron g -factor of the undoped GaAs QWs, systematic studies are carried out by an Oxford superconducting magnetic system (Spectromag SM 4000-8).

A large range of magnetic field strength up to 8 T is available for this superconducting magnetic system. This allows magnetic field dependent studies on electron spin coherence in GaAs-QWs. The high range of magnetic field over 7 T needs the operation of a lambda refrigerator. In this dissertation, most of data were taken at 3 T. The homogeneity of the central field over 10 mm diameter spherical volume is 0.6%. Samples were mounted on a c-axis sapphire disks in Voigt geometry in the dynamic variable temperature insert. This variable temperature insert can

support a sample temperature from 1.5 K to 300 K, which allows the temperature dependent studies.

In all measurements, pump and probe fields were focused onto samples using far-field optics. Typical focal lengths $f_{\text{probe}} = 200$ mm and $f_{\text{pump}} = 300$ mm were used ($f_{\text{probe}} = 100$ mm and $f_{\text{pump}} = 150$ mm for small magnet). For a three-pulse experiment, the focal length for the control beam was $f_{\text{control}} = 250$ mm. Typical focused spot size were 2×10^{-4} cm² for the pump, 1×10^{-4} cm² for the control and 8×10^{-5} cm² for the probe, approximately. Appropriate polarization optics were used for each beam to allow for polarization dependent measurements.

Transient Differential Absorption Spectroscopy

The GaAs QW samples were held on the variable temperature insert in the sample chamber of the super-magnet helium cryostat. The probe beam transmitted through the sample was collected and sent through a spectrometer (Jobin-Yvon SPEX 320) with 0.05 nm resolution. The resulting spectrally-resolved signal was detected using a photomultiplier tube (Hamamatsu R928). Absorption spectra in the presence or absence of the pump were measured using the relationship:

$$\alpha(\lambda)L = -\ln \frac{T(\lambda)}{T_0(\lambda)} \quad (4.1)$$

where $\alpha(\lambda)$ is the absorption coefficient as a function of the probe wavelength λ , L is the thickness of the absorbing region of the sample, $T(\lambda)$ is the measured

intensity of the probe after passing through the sample, and $T_0(\lambda)$ is the intensity of the probe passed through the sapphire disc only without the sample. We will refer to the quantity αL as the absorbance when presenting experimental data.

For the pump-probe nonlinear differential absorption measurement, as shown in Fig. 17, a pump induced absorbance difference can be measured by modulating the pump intensity and by detecting the transmission T of a probe beam with a lock-in amplifier.

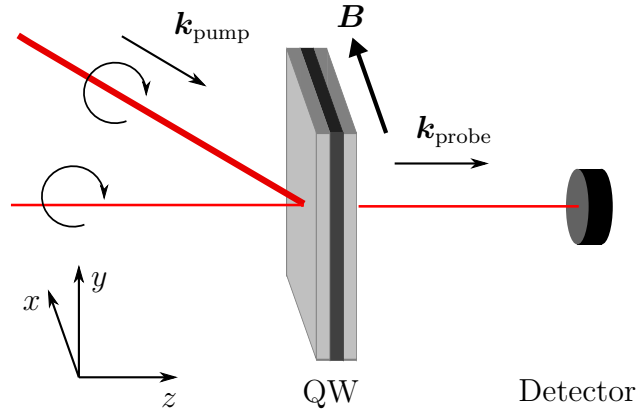


FIGURE 17. Schematic of the transient DA apparatus.

A differential transmission signal is defined as

$$\Delta T = T_{\text{pump-on}} - T_{\text{pump-off}} \quad (4.2)$$

For a small αL and small ΔT , the normalized differential transmission $\Delta T/T$ is approximately $-\Delta\alpha L$, because

$$\frac{\Delta T}{T} \approx \exp(-\alpha_{\text{pump-on}}L) - \exp(-\alpha_{\text{pump-off}}L) \approx -\Delta\alpha L \quad \text{for } \alpha L \ll 1 \quad (4.3)$$

For time domain transient measurements, the probe pulse arrives on the sample at a delayed time t_2 compared to the arriving time of pump pulse t_1 , where the time evolution of the nonlinear optical responses is measured as a function of the delay $\tau = t_2 - t_1$.

Time-Resolved Faraday Rotation (TRFR)

TRFR is widely used for spin relaxation and decoherence measurements on transparent semiconductor QWs, due to the fact that the time evolution of an optically induced birefringence can be measured as a polarization rotation evolution. It is a pump-probe nonlinear optical experiment. A circularly polarized pump pulse initializes an optical spin orientation in the QWs. A delayed linearly polarized probe pulse then mixes with the time evolved nonlinear polarization. By examining the resulting polarization rotation of the probe beam, which carries the evolution information the of spin states, one can study the spin relaxation or decoherence process.

Faraday rotation in nonmagnetic semiconductors is generally quite small, on the order of a few tens of microradians (μrad) to several miliradians (mrad) [40], where the excited electron-hole pair density is about 10^8 cm^{-3} , which makes the detection of spin very difficult. Therefore, extremely sensitive measurement is usually required in these experiments. The polarization rotation of probe field can be conveniently

measured by a balanced optical bridge [41]. Thanks to the nature of balanced detection, TRFR features a high signal/noise ratio so that a high sensitivity can be obtained. Therefore, TRFR is a very popular technique to measure and manipulate spin coherence.

Spin coherence induced nonlinear responses can be detected by various nonlinear optical methods [26, 42]. In a transient differential absorption experiment, a quantum beat is observed in the absorption difference between pump on and pump off. This absorption beat is associated with the imaginary part of nonlinear susceptibility. On the contrary, TRFR measures polarization rotation of the probe field induced by the pump pulses, which is related to the changes induced by the pump pulse in the real part of nonlinear susceptibility. In the experiments, a modulated (mechanically chopped) circularly polarized pump beam excites spin coherence in the sample at t_1 . A linearly polarized probe pulse pass through sample at t_2 . The probe polarization rotation angle is measured by the balanced optical bridge after the sample as a function of pump probe delay ($\tau = t_2 - t_1$).

Consider a sample with length L at origin $z = 0$ with a linear polarized probe field propagating along z direction. Before incident to the sample the field is described as

$$\begin{aligned} \mathbf{E}(0, t) &= \sqrt{2}E_0 \exp i(-\omega t)\hat{e}_x \\ &= E_0 \exp i(-\omega t)\hat{e}_+ + E_0 \exp i(k_z z - \omega t)\hat{e}_- \end{aligned} \quad (4.4)$$

where the field is decomposed in the circularly polarization basis defined by equations (3.15) and (3.16).

In the presence of a pump field, a birefringence as well as an absorbance imbalance in the two circular polarization bases can be described by non-equal n_+ , n_- and α_+ , α_- . Then after passing through the sample, the probe field can be described as

$$\begin{aligned} E(L, t) = & E_0 \exp(-\alpha_+ L) \exp i \left(\frac{2\pi}{\lambda} n_+ L - \omega t \right) \hat{e}_+ \\ & + E_0 \exp(-\alpha_- L) \exp i \left(\frac{2\pi}{\lambda} n_- L - \omega t \right) \hat{e}_- \end{aligned} \quad (4.5)$$

Because the differential absorption normally is very small ($\sim 10^{-3}$), the α_+ and α_- can be taken as equal to α . The resulting field can be approximated as

$$\begin{aligned} E(L, t) & \simeq E_0 \exp(-\alpha L) \exp i \left(\frac{2\pi}{\lambda} n_+ L - \omega t \right) \hat{e}_+ \\ & + E_0 \exp(-\alpha L) \exp i \left(\frac{2\pi}{\lambda} n_- L - \omega t \right) \hat{e}_- \\ & = \sqrt{2} E_0 \exp(-\alpha L) (\cos \Delta\theta \hat{e}_x - \sin \Delta\theta \hat{e}_y) \\ & \quad \times \exp \left(\frac{2\pi}{\lambda} \frac{n_+ + n_-}{2} L - \omega t \right) \end{aligned} \quad (4.6)$$

where

$$\Delta\theta = \frac{2\pi}{\lambda} \frac{n_+ - n_-}{2} L \quad (4.7)$$

is the polarization rotation angle.

As illustrated in Fig. 18, a balanced optical bridge is used to measure the polarization rotation of probe field. It is formed by a polarization beam splitter cube (PBS) with two independent nearly-identical slow photo detectors. The two detectors measure intensities of each beam. A half-wave plate is used to balance the bridge for the probe field without the pump field. In an experiment with a X polarized probe field, the half-wave plate was rotated by an angle of approximately 22.5° to the x -axis so that the X polarized probe field without pump field is rotated to 45° respected to the PBS x axis. The signal from the two detectors are balanced to zero, i.e., $I_{p, \text{pump_off}} - I_{s, \text{pump_off}} = 0$.

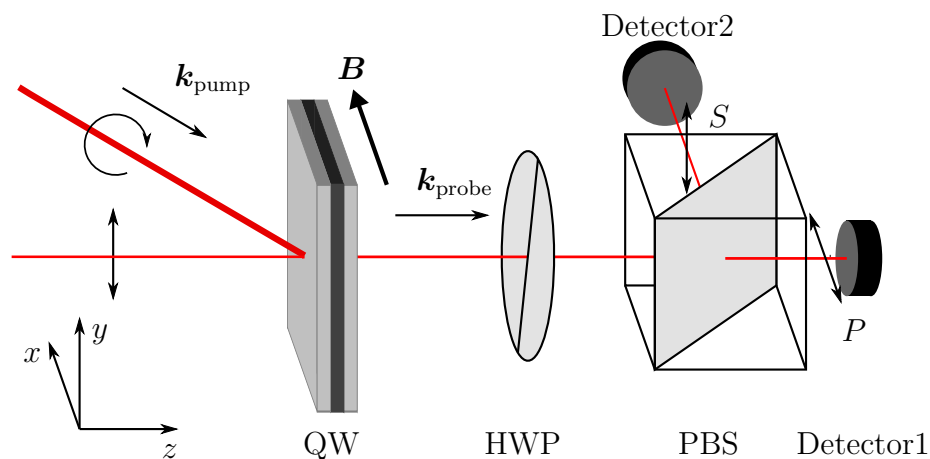


FIGURE 18. Schematic of the TRFR apparatus.

It can be shown that with a small polarization rotation, the rotation angle is given by

$$\Delta\theta = \frac{I_p - I_s}{2(I_p + I_s)} \quad (4.8)$$

With a modulated pump beam, any unbalanced signal can be lock-in detected which corresponds to a pump-induced circular birefringence. Due to the high signal/noise ratio for the balanced detection, this method is very sensitive and can measure a polarization rotation with μrad sensitivities.

Overview of Experimental Setup

Figure 19 shows a schematic of the experimental setup. The output from the Ti:sapphire laser was split into pump and probe beams. Flip mirrors are used in the setup for the experimental convenience to switch the detection methods between linear spectrum, DA, and TRFR. A spectrum can be obtained using a spectrometer with a photomultiplier tube (PMT). The optical polarizations are set by the wave-plates.

The pump field is spectrally filtered, as described in previous sections. The probe field is also spectrally filtered. The lateral position of the vertical slits for external pulse shapers were controlled by motorized actuators with 40 nm space lateral resolution. The resulting optical beam detuning is approximately linear to the position of the slits. Thus the detuning of the filtered optical fields can be calibrated by the spectrometer.

A third control beam is split from the probe for the experiments described in Chapter VI and Chapter VII. A motorized scanning linear translation stage with 1 μm resolution was placed in the pump beam to scan the delay between the pump

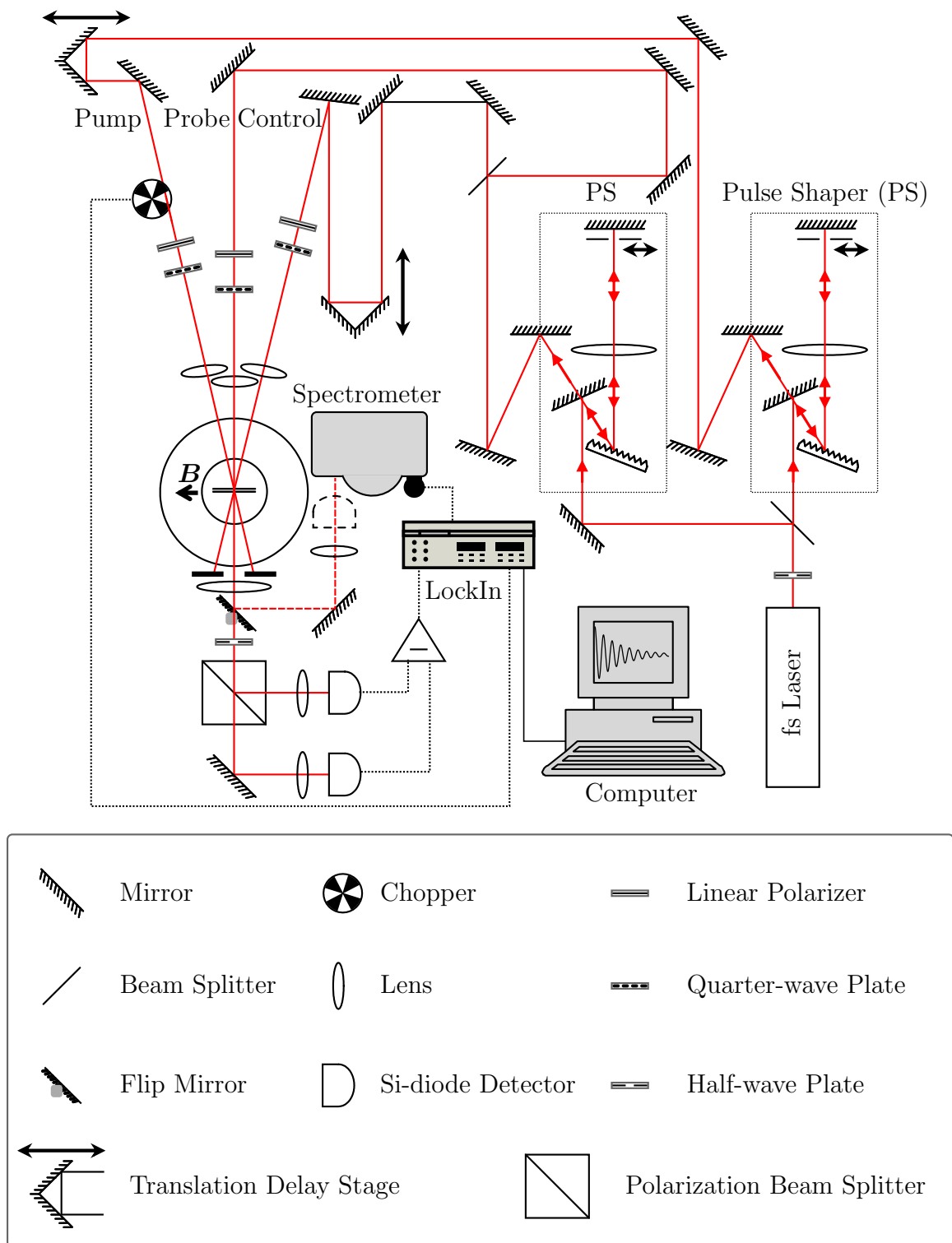


FIGURE 19. Schematic of the experimental apparatus.

and probe pulses. Another motorized scanning linear translation stage with 1 μm resolution was placed in the control beam to scan the delay between control and probe pulses. The zero delay position is set by measuring the cross-correlation of the pump and probe pulses using a LBO crystal to generate a nonlinear sum-frequency signal, or is set just by measuring the zero-field DA signal by the sample itself. The timing of pulses is described in Chapter VI.

CHAPTER V

ELECTRON SPIN COHERENCE OBSERVED IN TRFR

The primary experimental tool for probing electron spin coherence has been TRFR, which directly measures coherent spin evolution [15]. Specifically, TRFR measures birefringence created by a circularly polarized pump field, which leads to a polarization rotation in a linearly polarized probe field. The rotation angle $\Delta\theta$ is measured with a lock-in method and is given by

$$\Delta\theta = \theta_{\text{pump-on}} - \theta_{\text{pump-off}} \propto (\Delta n_+ - \Delta n_-) \quad (5.1)$$

TRFR is a very sensitive measurement compared to the DA measurement, due to the usage of a balanced optical bridge, as illustrated in Chapter IV. In this chapter we will explore the quantum beats arising from electron spin coherence by a degenerate TRFR experiment, in which pump and probe are at the same spectral position at the HH absorption line center. The results presented in this chapter agree with earlier studies.

Magnetic Field Dependence

As described in Eqn. (3.7), the observed beating frequency is proportional to the external magnetic field. The magnetic field dependence for the 13 nm GaAs MQW (sample B) is shown in Fig. 20. The beating frequency, i.e., the Larmor frequency ω_L , can be retrieved with a very high precision by fitting the polarization rotation beats with the function:

$$\Delta\theta = A_\theta \cos(\omega_L t) \exp[-t/T_2^*] \quad (5.2)$$

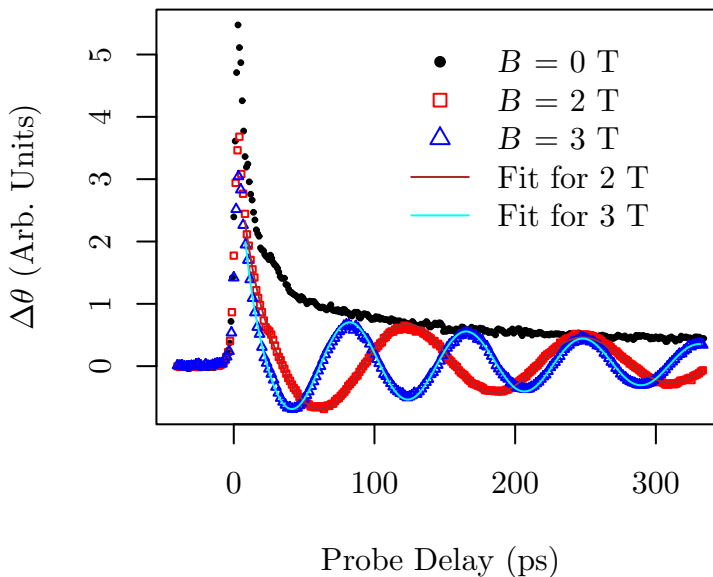


FIGURE 20. TRFR quantum beats from the 13 nm GaAs MQW (sample B) at 10 K measured as a function of magnetic field.

Both $|g_e|$ and the ensemble transverse spin decoherence time T_2^* can be obtained from the TRFR responses. For the data shown in Fig. 20, the beating periods

obtained for $B = 2$ T and 3 T are 124.5 ps and 82.8 ps, respectively, corresponding to a Zeeman splitting of 0.03318 meV and 0.04992 meV. $|g_e|$ at 2 T and 3 T is thus 0.2869 and 0.2878, respectively. The decoherence time T_2^* is 324.3 ps and 377.0 ps, for $B = 2$ T and 3 T fields, respectively. This result is similar to that shown in earlier studies [14]. The electron's precession frequency shows a nearly linear dependence to the external magnetic field, which indicates that an electron contained in an exciton can precess in a transverse magnetic field like a free electron. This is due to a rapid hole spin-flip. Within the exciton, the electron-hole exchange interaction describes the correlation between electron and hole spins. This correlation is very weak in GaAs QW, leads to a small electron-hole exchange splitting energy δ . A hole spin-flip rate much larger than δ/\hbar leads to vanishing average exchange fields from the holes [43, 44].

Temperature Dependence

With the sensitivity of the TRFR technique, a spin quantum beat can still be observed even at an elevated temperature. Figure 21 illustrates a series of TRFR data taken with the sample B at different temperatures. It can be seen that even at room temperature the spin coherence is still preserved for a significant length of time. In contrast, the DA measurements of the same sample under the same condition are

very noisy when temperatures were over 50 K, and the spin quantum beats eventually became hard to measure at high temperatures with DA method (data not shown).

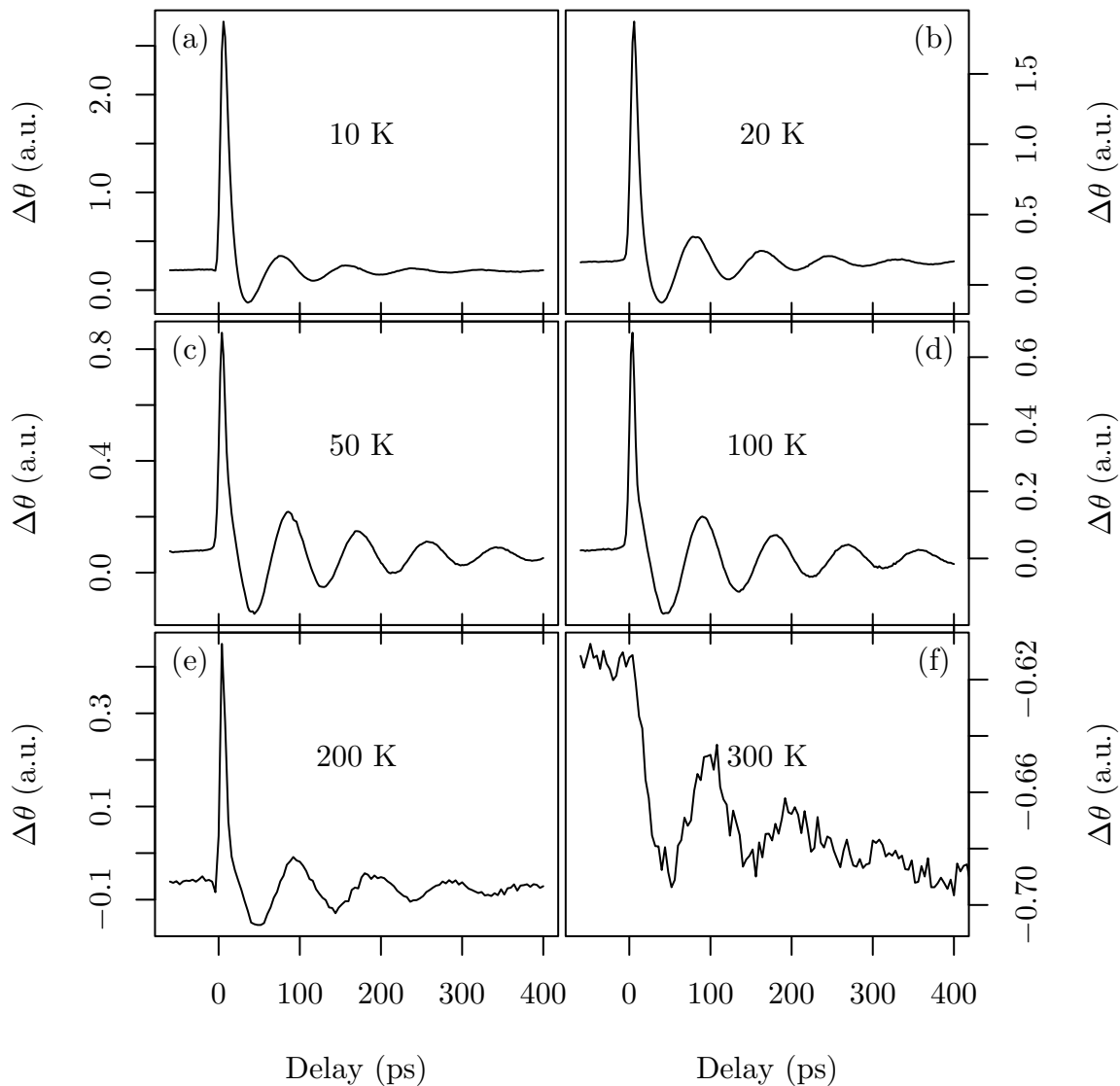


FIGURE 21. Degenerate TRFR responses obtained in a 13 nm GaAs MQW (sample B) at various temperatures. Temperatures are labeled in the figure. The magnetic field is set to 3 T. Pump and probe are tuned to the HH absorption line center.

Figure 22 shows the temperature dependence of the magnitude of the electron g -factor and the transverse spin decoherence time T_2^* . The magnitude of the g -factor shows a monotonic decrease as the temperature increases, and the T_2^* shows an increase as the temperature increases from 10 K. There are several theoretical investigations which provide analytical and numerically simulated results comparable with TRFR experiments [45]. A comprehensive analysis of electron spin coherence for HH exciton transitions in QWs in Voigt geometry is given under kinetic theory with density matrix formalism [46]. The author calculates and numerically simulates the spin dephasing in GaAs QWs, and discusses various dephasing mechanisms and temperature dependence in this system. Our results qualitatively agree with the published studies [35].

The strength and orientation of the external field and other factors, like temperature, have very interesting impacts on the g -factors and spin decoherence mechanisms, and have been extensively studied. A comprehensive discussion regarding these topics, however, is beyond the scope of this dissertation.

Detuning Dependence for Degenerate Pump–Probe

Figure 23 presents a measurement of the electron spin decoherence process of the 13 nm GaAs MQW (sample B), where both pump and probe are degenerate in energy and are at different detunings from the exciton absorption line center. The

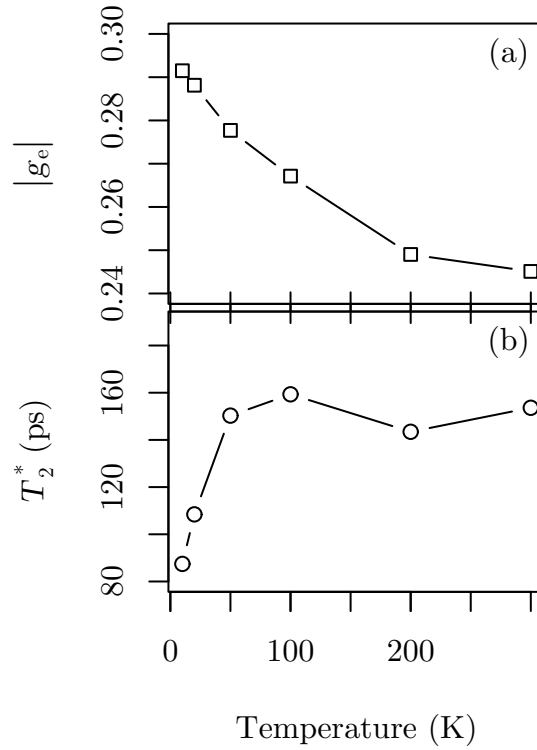


FIGURE 22. Temperature dependence of $|g_e|$ and T_2^* .

spectral lineshape of the pump and probe are plotted as the shaded areas in Fig. 23(a), together with the absorption spectrum. A_θ , T_2^* and $|g_e|$ are obtained by fitting the degenerate TRFR responses with Eqn. (5.2), and are shown in Figs. 23(b), (c) and (d), respectively. A significantly longer decoherence time is observed at an energy slightly lower than the HH exciton line center, which is associated with the localized excitons. When the pump and probe are tuned at a position between HH and LH resonances, quantum beats obtained feature a phase opposite to those obtained when the pump and probe are at the HH or LH resonance. Overall, A_θ , T_2^* and $|g_e|$ depend strongly on the excitation energy. Note that T_2^* and $|g_e|$ obtained when the beat

amplitude A_θ nearly vanishes, are not very reliable due to the poor signal/noise ratio (i.e., the data set with the highest pump/probe energy).

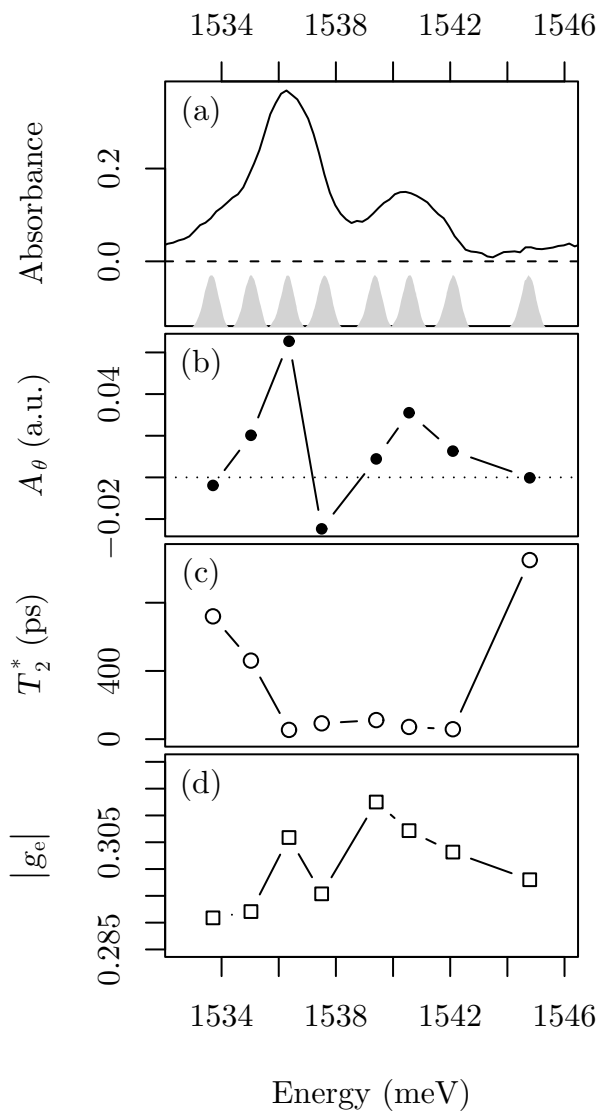


FIGURE 23. Detuning dependence of degenerate TRFR. The spectral shape of degenerate pump and probe pulses at different detunings are indicated as shaded areas in (a). (a) the absorbance of sample B at 10 K; (b) the polarization rotation beats amplitude A_θ as a function of detuning; (c) the transverse spin decoherence time T_2^* as a function of detuning; (d) the amplitude of g-factor $|g_e|$ as a function of detuning.

The above result clearly indicates that a broadband pump field will cause multiple excitonic systems to be excited, which will complicate the interpretation of the experimental result. In addition, it is interesting to note that from the simple non-interacting atomic-like model, the degenerate TRFR should vanish when both pump and probe are resonant with the relevant optical transitions, as shown in Fig. 12. However, this is not what had been observed in the experiment. This suggests that a simple non-interacting atomic-like model is not adequate to describe this system.

A typical TRFR experiment in magnetic semiconductor QW is performed with degenerate fs laser pulses, which cover the exciton resonance, resolving a ps scale beating frequency due to the large g -factor of the electrons [15]. However it is well known that resonances with very small spectral separation, like localized excitons, biexcitons, trions, or shallow donors, can all play important roles, provided that the optical field is nearly resonant to those resonances. To obtain the spectral information while retaining the desired time domain quantum beats, a two-color pump-probe technique can be used.

For the two-color pump-probe experiment, the probe field and pump field are independently filtered and tunable. The spectrally narrowed pump is tuned to the absorption HH center so that only electron spin coherence associated with the mobile HH excitons is excited by the pump field. Nearly degenerate TRFR responses can be obtained by tuning the probe field at various energies. This technique allows to single out the spectral response for the studies of exciton interaction effects in TRFR,

and to avoid the complications due to the LH resonance and localized excitons. A detailed study of the nearly degenerate TRFR response is presented in Chapter VIII.

Summary

The TRFR is a powerful tool to study the electron spin coherence. Quantum beat responses arising from electron spin coherence are observed from 10 K to room temperature in an undoped GaAs QW. The spin decoherence time at 10 K is in the order of 100 ps.

In spite of rapid progress in studies of coherent spin manipulation, how manybody interactions affect and manifest in TRFR remains an open question. The temporal TRFR response corresponds to electron spin precession and can be understood without invoking manybody effects [47]. In Chapter VIII we will have a detailed discussion on the effects of exciton interactions in TRFR. But before the presentation of more detailed experimental results on TRFR, in the following chapters, we shall first discuss a spin manipulation scheme and the related manybody effects in the DA experiments.

CHAPTER VI

MANIPULATING SPIN PRECESSION WITH OPTICAL PULSES

Recently, there has been an increasing interest in employing nonlinear optical techniques to control optical and transport processes in semiconductors. Interference between one- and two-photon absorption pathways has been exploited for the optical generation of electrical as well as spin currents [48–51]. Various techniques have also been used to manipulate carrier population, electron-phonon interaction, and biexciton coherence [52–58]. An earlier study based on Faraday rotation has used optical Stark effects generated by an optical pulse below the band gap to manipulate electron spin precession [6].

This chapter presents a new optical method to manipulate electron spin precession. In this scheme, a third optical pulse, in addition to a conventional pump-probe setup, is used to manipulate electron spin precession by tipping the spin away from its original precession plane. The amplitude, as well as the phase of

the DA quantum beats from electron spin coherence, can be manipulated through the intensity, timing, or polarization of the control field.

Spin Control in a Precession Picture

The three-pulse DA can be analyzed within the limit of a spin precession model, as illustrated in Fig. 24. First, a pump pulse generates a spin polarization oriented along the z -axis (normal to the QW plane). The spin then precesses in the $y - z$ plane around the external magnetic field along the x -axis. Secondly, a control pulse tips the spin polarization induced by the pump away from the $y - z$ plane, with a tipping angle ϑ . The tipping angle ϑ is set by the control pulse intensity. Finally, the DA response, which includes the spin precession information, is measured by a probe pulse.

The timing of the three-pulse DA experiment is illustrated in Fig. 25(a). A pump pulse arrives at t_1 . A control pulse arrives at a later time, t_2 . A probe pulse arrives at t_3 . For convenience in the later discussion, we define the various delays as

$$\tau_1 = t_3 - t_1, \quad \text{delay between probe and pump;} \quad (6.1)$$

$$\tau_2 = t_3 - t_2, \quad \text{delay between probe and control.} \quad (6.2)$$

In the experiment, the intensity of the pump beam is modulated and lock-in detection is used to measure the change in the absorption of the probe induced

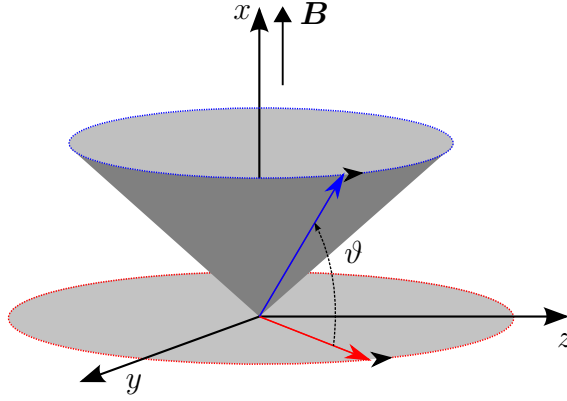


FIGURE 24. Schematic of tipping a precessing spin by an optical pulse. Red arrow indicates the precessing spin initialized by a pump pulse. Blue arrow indicates the precessing spin tipped by a control pulse.

by the pump, as shown in Fig. 25(b). This approach eliminates nonlinear optical contributions that are induced by the coupling between the control and probe but without involving the pump. In addition, the DA response is measured as a function of τ_1 with a fixed τ_2 , avoiding complications due to quantum beats arising from spin precessions initiated by the control pulse.

After the tipping by control pulse, the spin can be decomposed into two orthogonal components: a perpendicular component and a parallel component, with respect to the external magnetic field. The amplitudes of the perpendicular and parallel components of the tipped spin polarization are $S_{\perp} = S_0 \cos \vartheta$ and $S_{\parallel} = S_0 \sin \vartheta$, respectively, where S_0 is the amplitude of the spin polarization induced by the pump. The spin precession continues for the perpendicular component, but stops for the parallel component. The phase of the quantum beats associated with

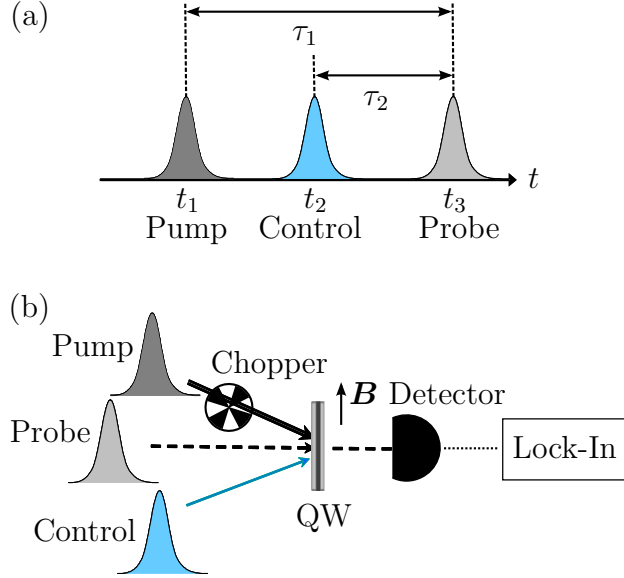


FIGURE 25. (a) Pulse sequence for three-pulse DA measurement. (b) Schematic of the three-pulse DA setup.

the perpendicular and parallel components are thus characterized by $\cos \omega_L(t_3 - t_1)$ and $\cos \omega_L(t_2 - t_1)$, respectively, where ω_L is the Larmor frequency. The temporal behavior of the overall quantum beats can be described by

$$\begin{aligned}
 I_{QB}(t) = & \alpha S_{\perp} \cos \omega_L(t_3 - t_1) \exp \left[-\frac{t_3 - t_1}{T_2^*} \right] \\
 & + \beta S_{\parallel} \cos \omega_L(t_2 - t_1) \exp \left[-\frac{t_2 - t_1}{T_2^*} \right]
 \end{aligned} \tag{6.3}$$

where α and β are determined by details of the nonlinear optical processes. Apparently the two spin components share the same decoherence time, based on the observation in the experiments.

Equation (6.3) illustrates that the overall quantum beats depend on the relative phase of the Larmor precessions and also on the relative contributions from

the two spin components. It can be rewritten into a form in terms of the delay variables τ_1 and τ_2 used in the experiments:

$$I_{QB}(t) = \alpha S_{\perp} \cos \omega_L \tau_1 \exp \left[-\frac{\tau_1}{T_2^*} \right] + \beta S_{\parallel} \cos(\omega_L \tau_1 - \omega_L \tau_2) \exp \left[-\frac{\tau_1 - \tau_2}{T_2^*} \right] \quad (6.4)$$

It can be seen from Eqn. (6.4), that the effect of varying the timing of a control pulse, is to change the relative phase between the parallel and the perpendicular components. As we will discuss in detail below, with a proper relative phase for the Larmor precessions, we can manipulate the amplitude as well as the phase of the quantum beats by varying the tipping angle of the control pulse.

The experimental studies were carried out in sample A, a high quality undoped (001) 17.5 nm single QW sample grown by molecular beam epitaxy. All measurements were carried out at a temperature of 10 K and at an external magnetic field of 3 Tesla. All three pulses – pump, probe and control, were filtered by external pulse shapers to derive narrow bandwidth optical pulse trains from a femtosecond mode-locked Ti:Sapphire laser. The resulting nearly transform limited pulses had a spectral bandwidth of 0.6 meV and a duration of 5 ps. All three laser pulses used in DA were positioned at the HH exciton absorption line center to avoid contributions from strongly localized excitons.

Controlling the Amplitude of the Quantum Beats

In the following, we will explore the dependence of the quantum beats on the control–probe delay. Figure 26 shows the DA responses as a function of τ_1 obtained with increasing control intensities and with a fixed delay τ_2 set to $\omega_L\tau_2 = \pi$ and $\omega_L\tau_2 = 2\pi$, respectively. The DA responses in Fig. 26 feature pronounced quantum beats induced by the electron spin coherence. The quantum beats correspond to an electron Zeeman splitting of 0.067 meV and a spin decoherence time of 0.3 ns. The timing of the control pulse is actually shown as a dip in the DA response for data with high control intensity in Fig. 26, when the pump overlaps with the control in time.

The results in Figures 26(a) and 26(b) demonstrate the control of the quantum beat amplitude by varying the tipping angle of the control pulse, when the delay between control–probe satisfies the relations:

$$\omega_L\tau_2 = 2n\pi \tag{6.5}$$

or

$$\omega_L\tau_2 = (2n + 1)\pi \tag{6.6}$$

where $n = 0, 1, 2, 3, \dots$

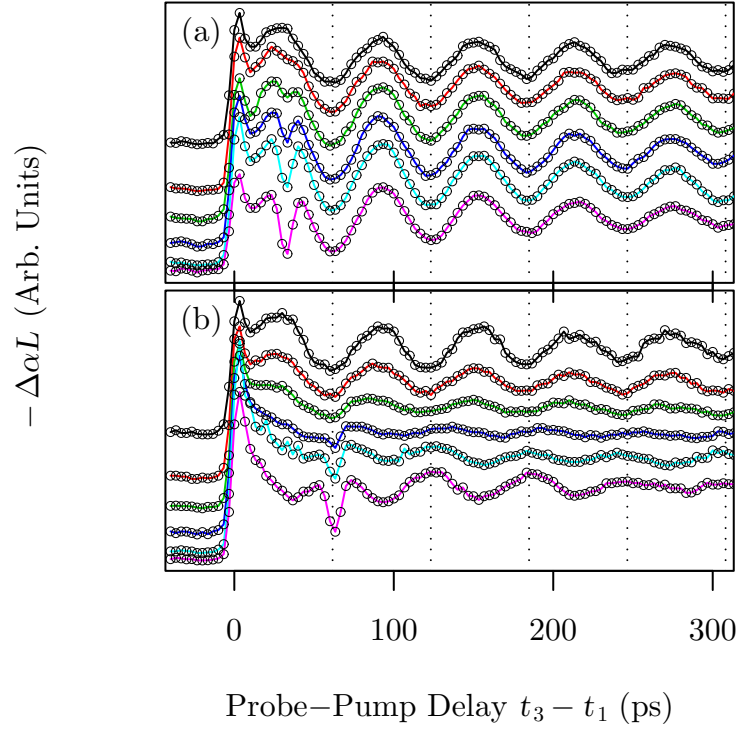


FIGURE 26. DA responses as a function of the pump-probe delay with a fixed delay, τ_2 , between the control and probe. The quantum beat amplitudes are changed as a function of control intensity. (a) $\omega_L\tau_2 = \pi$; (b) $\omega_L\tau_2 = 2\pi$. The control intensities used in each sub-figure from the top to the bottom curves are $0, I_0, 2I_0, 3.5I_0, 5I_0, 10I_0$ with $I_0 = 0.3 \text{ W/cm}^2$. The average pump and probe intensities are 0.12 W/cm^2 and 0.09 W/cm^2 , respectively. The responses are vertically offset for clarity. Dotted lines are guides for the eye.

For the cases satisfying Eqn. (6.5), the amplitude of the quantum beats increases with increasing control intensity, while the phase of the quantum beats remains unchanged.

In comparison, for conditions satisfying Eqn. (6.6), the amplitude of the quantum beats decreases with increasing control intensity and eventually flips sign. These behaviors elucidate the dependence of the quantum beats on the relative phase of the Larmor precessions and can be understood in the context of Eqn. (6.3). From

experiment, we observed that for $\omega\tau_2 = \pi$, quantum beats arising from the parallel and perpendicular spin components have the same phase, while for $\omega\tau_2 = 2\pi$, quantum beats from the two spin components are 180° out of phase. These results indicate a sign difference between α and β .

Controlling the Phase of the Quantum Beats

For the control-probe delays not satisfying Eqn. (6.5) or Eqn. (6.6), varying the relative contributions of the two spin components to quantum beats via the tipping angle of the control pulse also leads to a corresponding change in the phase of the overall quantum beats. For example, when the fixed delay τ_2 is set to $\omega\tau_2 = \pi/2$ or $\omega\tau_2 = 3\pi/2$, the quantum beats from the two spin components have a phase difference of $-\pi/2$ or $\pi/2$, respectively. The experimental results are shown in Fig. 27(a) and Fig. 27(b), respectively. These results demonstrate the phase control of the quantum beats.

The relative contributions of the two spin components in quantum beats, $\frac{|\alpha S_\perp|}{|\alpha S_\perp| + |\beta S_\parallel|}$ and $\frac{|\beta S_\parallel|}{|\alpha S_\perp| + |\beta S_\parallel|}$, can be determined by numerically fitting these quantum beat responses to Eqn. (6.3). As shown in Fig. 28, the relative contribution from the parallel spin component increases with control intensity. For I_{control} near 1 W/cm^2 , the two spin components contribute nearly equally to the quantum beats, which is in agreement with the near vanishing of quantum beats at this intensity

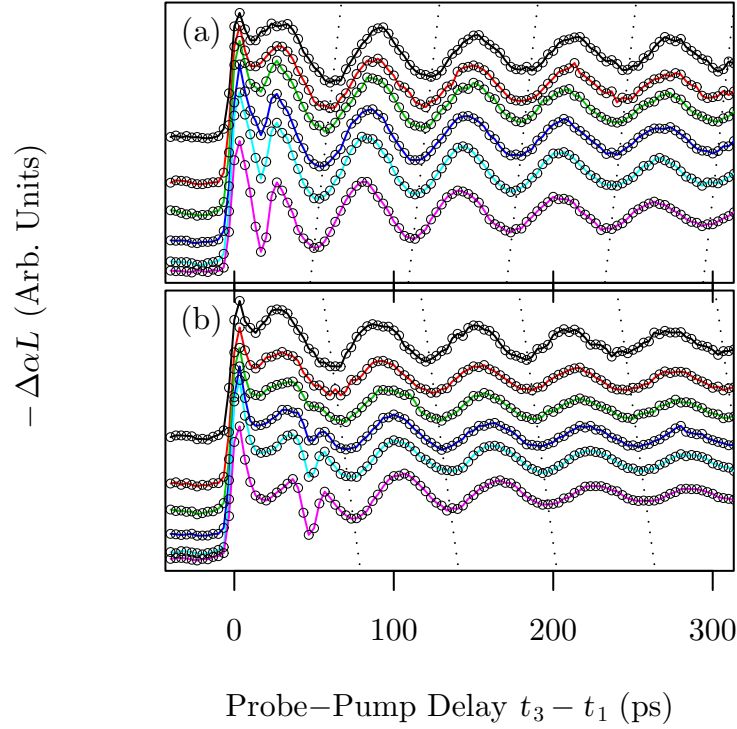


FIGURE 27. DA responses as a function of the pump-probe delay with a fixed delay, τ_2 , between the control and probe. The quantum beat phase is changed as a function of control intensity. (a) $\omega_L\tau_2 = \pi/2$; (b) $\omega_L\tau_2 = 3\pi/2$. The control intensities used in each sub-figure from the top to the bottom curves are $0, I_0, 2I_0, 3.5I_0, 5I_0, 10I_0$ with $I_0 = 0.3 \text{ W/cm}^2$. The average pump and probe intensities are 0.12 W/cm^2 and 0.09 W/cm^2 , respectively. The responses are vertically offset for clarity. Dotted lines are guides for the eye.

shown in Fig. 26(b). At $I_{\text{control}} = 6 \text{ W/cm}^2$, the quantum beats become dominated by contributions from the parallel spin component.

To confirm the contribution from the parallel spin component, an experimental investigation on the dependence of the quantum beat phase on the fixed delay, τ_2 , between the control and probe had been carried out. For the parallel spin component, the phase of the quantum beats depends only on the delay between the pump and

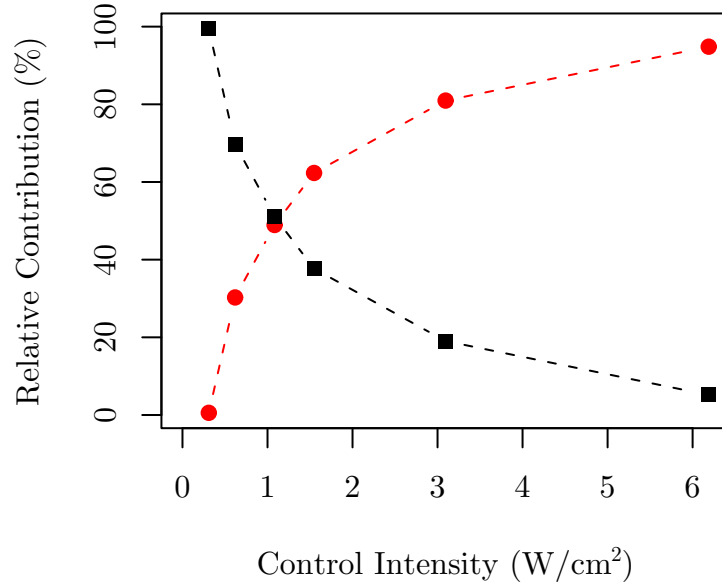


FIGURE 28. The relative contribution to quantum beats from the parallel (circles) and perpendicular (squares) spin components as a function of the control intensity.

control, $t_2 - t_1$, and is independent of the timing of the probe since the spin precession stops after the control. Figure 29(a) shows the DA responses as a function of τ_1 obtained at various fixed τ_2 and with $I_{\text{control}} = 6 \text{ W/cm}^2$. Figure 29(b) plots the same experimental results as in Fig. 29(a), but effectively as a function of the delay between the pump and control, i.e., by subtracting the fixed delay τ_2 from τ_1 . All the quantum beats plotted in Fig. 29(b) have the same phase. The quantum beat phase is thus independent of the timing of the probe pulse, demonstrating that these quantum beats arise nearly completely from the parallel spin component, which confirms the result of the numerical analysis shown in Fig. 28.

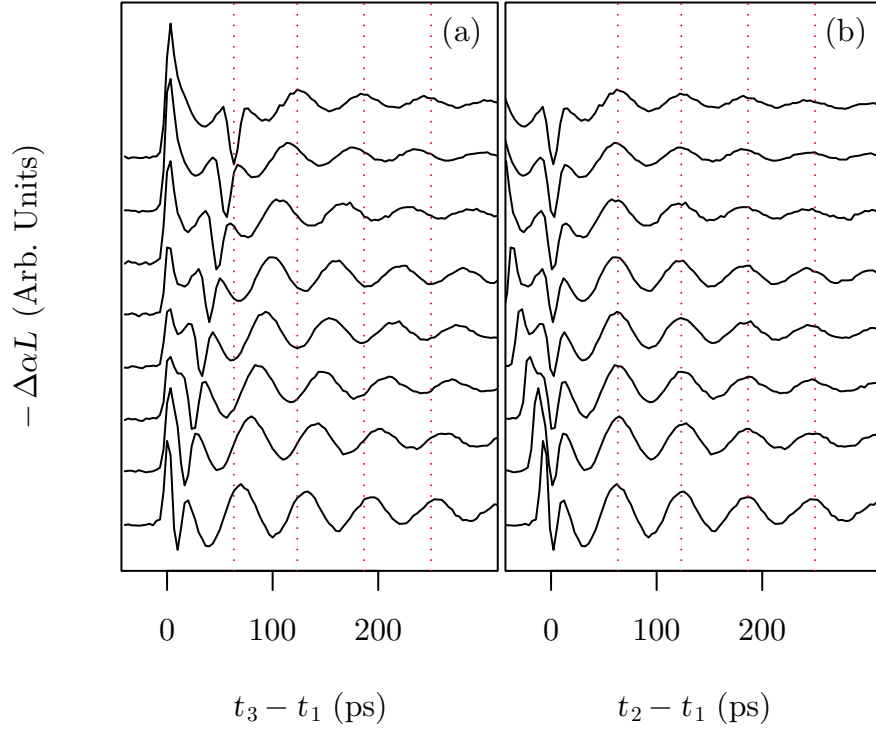


FIGURE 29. (a) DA responses as a function of the pump-probe delay at a fixed τ_2 given by 61 ps, 54 ps, 46 ps, 38 ps, 31 ps, 23 ps, 15 ps, and 7ps (from the top to the bottom curves). The average pump, control, and probe intensities are 0.12 W/cm^2 , 6 W/cm^2 , and 0.09 W/cm^2 , respectively. (b) The same group of data as in Fig. 29(a) but plotted as a function of the pump-control delay. The responses are vertically offset for clarity. Dotted lines are guides for the eye.

Note that the two spin components contribute nearly equally to the quantum beats at a control intensity of 1 W/cm^2 , which corresponds to an energy flux per pulse of 10 nJ/cm^2 and a peak field strength of 1 kV/cm . In comparison, for an atomic-like three-level system, theoretical analysis using order-by-order perturbation shows that the average control intensity needed to have equal contributions from the two spin components is approximately 5 W/cm^2 . For the numerical estimate, a matrix

element r_{cv} of 0.575 nm was used, which yields good agreement between theory and experiment for exciton Rabi oscillation and for exciton optical Stark splitting [3, 25]. This indicates that the dominating parallel component for DA responses at a high control intensity cannot be explained as a result of a nearly $\pi/2$ tipping angle ϑ . The effect of an almost pure parallel component contribution is related with an enhanced magnitude for the coefficient β , which is much larger compared to the coefficient α . This enhancement is due to the optical nonlinear processes arising from exciton-exciton interactions, which will be discussed in details later, in the Chapter VII.

Polarization Dependence

In addition to the intensity and timing, the behavior of the quantum beats also depends on the polarization of the control pulse. Figure 30 presents the result obtained with a co-circularly polarized pump and probe. The intensities for both pump and probe field are kept low such that a linear dependence of $\Delta T/T$ response on pump intensity is maintained, while the response is independent of the probe field intensity. The control pulse overlaps with the probe pulse in both time and energy. With a control pulse in the same circular polarization to the pump and probe, the phase of the quantum beat is shifted by π . With a control pulse of opposite circular polarization but otherwise under same condition, the phase of quantum beat is the same as the 3rd order response without control, but is in opposite phase to the co-

circular control case. Note the changes in the signal background levels as a result of control input. The phase of the quantum beats can be flipped by switching the polarization of the control pulse.

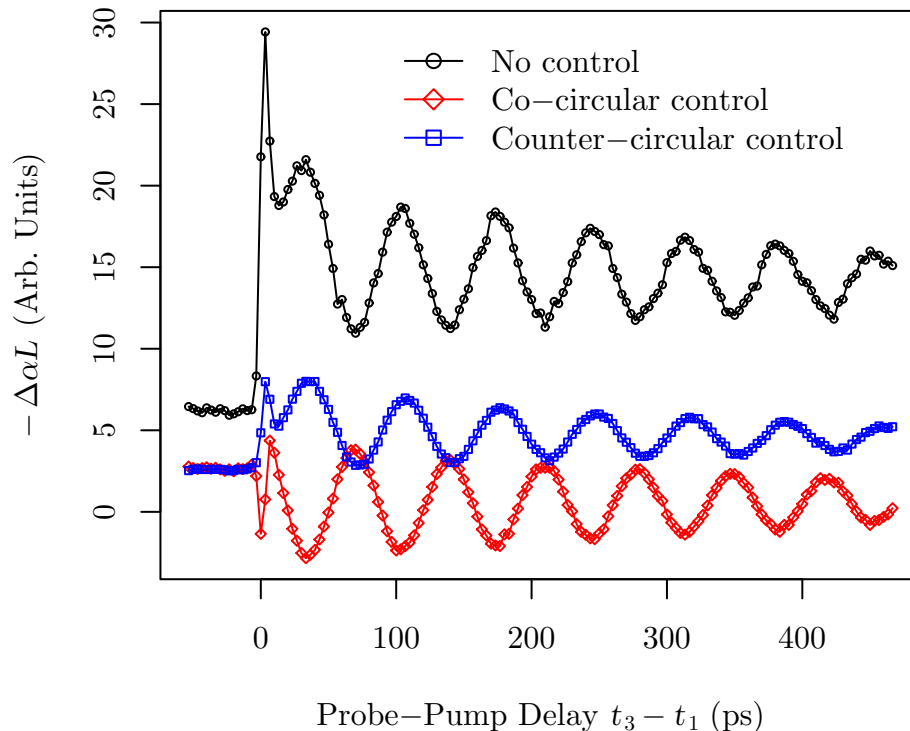


FIGURE 30. The absorption quantum beats of 17.5 nm GaAs SQW obtained at $B = 3$ T and $T = 10$ K. The energy flux density for co-circularly polarized pump and probe pulse is 4 nJ/cm^2 and 3 nJ/cm^2 , respectively. For the responses obtained with a control pulse, a 200 nJ/cm^2 energy flux density control pulse in same or opposite circular polarization is used. The control-probe delay τ_2 is set to zero.

Summary

In this chapter, an experimental study on the optical control of quantum beats induced by the electron spin coherence in a semiconductor QW is presented. In this scheme, an additional control pulse is added to a conventional pump-probe setup to manipulate the coherent spin dynamics. In comparison to earlier coherent control studies, the spin manipulation exploits the phase of the Larmor spin precession, instead of the optical phase of the pump or control pulses. The amplitude and especially the phase of the quantum beats can be controlled by varying the intensity or the tipping angle of the control pulse. This tipping allows the use of contributions to nonlinear optical responses from both parallel and perpendicular spin components to control the amplitude and phase of the quantum beats.

As shown in extensive earlier studies, coherent nonlinear optical responses in semiconductors are strongly modified by the underlying manybody interactions [59, 60]. As we will discuss in detail in the next chapter, the manifestation of the spin manipulation is enhanced by the underlying exciton-exciton interactions. The successful control of the quantum beats provides a rare example, where manybody interactions in an interacting many-particle system enhance instead of impeding the manipulation of quantum coherence.

CHAPTER VII

HIGHER ORDER NONLINEAR PROCESSES IN ABSORPTION

QUANTUM BEATS

Chapter VI showed that by changing the intensity, delay, and polarization of a control pulse, one could manipulate the nonlinear responses from electron spin coherence. This chapter presents additional experimental and theoretical studies on the effects of exciton manybody interactions. These studies further indicate that the previous spin manipulation scheme takes advantage of the underlying exciton-exciton interactions. As a result, this scheme can be more effective in an excitonic system than in a corresponding atomic-like system. In addition, it is possible to experimentally identify the nonlinear optical contributions from different channels of exciton-exciton interactions.

Quantum Beats from an N -exciton System

To understand the role of exciton-exciton interactions in the spin manipulation process, we have used an order-by-order perturbation analysis based on the phenomenological model of N -exciton energy eigenstates [22]. Let's consider the case that all optical fields have the same circular polarization σ^- . The non-vanishing dipole matrix elements are shown in the optical selection rule diagram in Fig. 31.

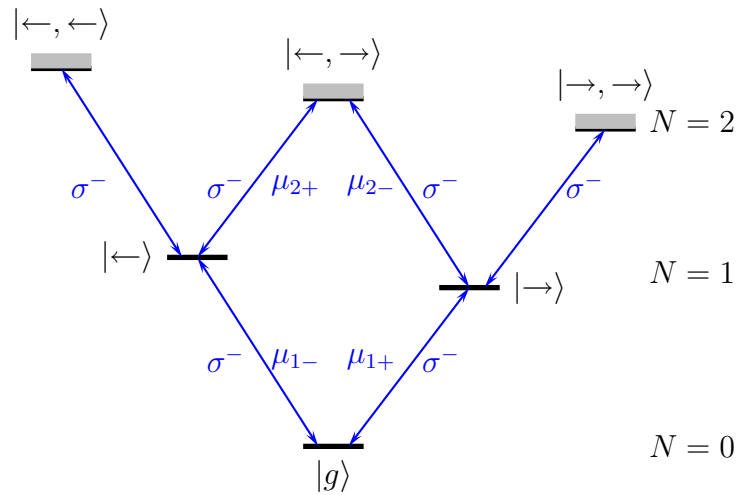


FIGURE 31. Optical selection rule for the transitions between the conduction and the $J_z=3/2$ valence bands in a magnetic field along the x-axis, illustrated in N -exciton energy eigenstates of ground, one-exciton, and two-exciton states. States are labeled by electron spin.

Figure 31 shows the energy eigenstates of the relevant excitonic system. $|g\rangle$ is the ground state. $|\rightarrow\rangle$ and $|\leftarrow\rangle$ are one-exciton states with electron spins $s_x = 1/2$ and $-1/2$, respectively. $|\leftarrow, \leftarrow\rangle$, $|\leftarrow, \rightarrow\rangle$, $|\rightarrow, \rightarrow\rangle$, are the two-exciton states

with electron spins $s_x = -1/2$ and $-1/2$, $s_x = -1/2$ and $1/2$, and $s_x = 1/2$ and $1/2$, respectively. Note that all excitons involve the same valence band state with $J_z = 3/2$. In this excitonic picture, the electron spin coherence corresponds to a coherent superposition of $|\rightarrow\rangle$ and $|\leftarrow\rangle$.

In this scheme, as discussed in early chapters and shown in Fig. 11, the pump as well as the control field couple to both electron spin states in the conduction band, as allowed by the dipole selection rule of the HH interband transition in the presence of an external magnetic field. The relevant nonlinear optical processes are to the second order of the pump field and the second or higher even orders of the control field, which eliminates the dependence of spin dynamics on the optical phase of the pump and the control pulses. In an order-by-order perturbation analysis, the pump pulse excites an electron spin coherence, $\rho_{\rightleftharpoons}^{(2)}$. To obtain analytical solutions, we assume that the duration of the incident laser pulses is short compared to the exciton linewidth and the electron Zeeman splitting. Using effective density matrix equations, we have

$$\rho_{\rightleftharpoons}^{(2)}(t) = \frac{\mu_1 + \mu_1 - \varepsilon_1^2}{4\hbar^2} \exp[(i\omega - \gamma)(t - t_1)], \quad (7.1)$$

where γ is the decay rate for the spin coherence and ε_1 , ε_2 , and ε_3 are the time integrated area of the electric field amplitude for the pump, control, and probe, respectively. The relevant dipole matrix elements are indicated in Fig. 31 and are assumed to be real. The control pulse couples to the spin coherence, $\rho_{\rightleftharpoons}^{(2)}$, generating electron spin coherence as well as population and two-exciton coherence terms, all

of which are to the fourth or higher order of the applied fields (second order to the pump field and second or higher even order to the control field). For simplicity, we limit our discussion to the second order of the control field. The fourth order spin coherence is then given by

$$\begin{aligned} \rho_{\rightleftharpoons}^{(4)}(t) &= -\frac{\mu_{1+}\mu_{1-}(\mu_{1+}^2 + \mu_{1-}^2 + \mu_{2+}^2 + \mu_{2-}^2)\varepsilon_1^2\varepsilon_2^2}{16\hbar^4} \\ &\times \exp[(i\omega - \gamma)(t - t_1)]. \end{aligned} \quad (7.2)$$

The net perpendicular spin component is determined by $\rho_{\rightleftharpoons} = \rho_{\rightleftharpoons}^{(2)} + \rho_{\rightleftharpoons}^{(4)}$. As shown in Eqns. (7.1) and (7.2), $\rho_{\rightleftharpoons}^{(2)}$ and $\rho_{\rightleftharpoons}^{(4)}$ feature the same Larmor precession but always interfere with each other destructively.

Effects of exciton-exciton interactions on the spin manipulation and on the control of the quantum beats can be understood by examining the role of the two-exciton states. As shown in Eqn. (7.2), the additional coupling of $\rho_{\rightleftharpoons}^{(2)}$ to $|\leftarrow, \rightarrow\rangle$ nearly doubles the magnitude of $\rho_{\rightleftharpoons}^{(4)}$, leading to a significant reduction in the net perpendicular spin component, which can be viewed as an effective increase in the tipping angle of the control pulse. Quantum beats associated with $\rho_{\rightleftharpoons}$ arise from the coupling of $\rho_{\rightleftharpoons}$ to the probe field via the ground state $|g\rangle$ and via the two-exciton state $|\leftarrow, \rightarrow\rangle$. These two processes interfere with each other destructively and can cancel each other out in the limit that the relevant one- and two-exciton transitions are identical. This cancellation leads to a weak response from the perpendicular spin component.

The parallel spin component can be understood as including contributions from various fourth order populations induced via interactions between the control and $\rho_{\pm\pm}^{(2)}$. For relatively large τ_2 , effects of the two-exciton coherence can be ignored due to its rapid decoherence. These populations contain the information of Larmor precession occurring before the arrival of the control pulse, which also leads to quantum beats in the DA response. For the parallel spin component, the coupling of the populations to two-exciton states $|\rightarrow, \rightarrow\rangle$ and $|\leftarrow, \leftarrow\rangle$ becomes important, as shown in Fig. 31. Coupling of $\rho_{\pm\pm}$ to these states are not allowed because of optical selection rules. These two-exciton states feature strong exchange interactions between excitons, minimizing the destructive interference between the relevant one- and two-exciton transitions. As a result, the exciton-exciton interactions enhance the relative contribution to quantum beats from the parallel spin component.

Note that exciton population and electron spin coherence involving spin-flipped holes with $J_z = -3/2$ can also contribute to the DA response via transitions to two-exciton states that involving both $J_z = 3/2$ and $J_z = -3/2$ holes. For simplicity and to illustrate how exciton-exciton interactions affect the spin manipulation process, the above discussion does not include the analysis of nonlinear optical processes related to two-exciton states involving spin-flipped holes.

Probe Intensity Dependence of Two-pulse DA

In the third order limit, which means that the nonlinear polarization is to the second order of the pump field and to the first order of the probe field, the amplitude of $\Delta T/T$ shows a linear intensity dependence on the pump field but independent on the probe intensity. In a study of probe intensity dependence on an un-doped 17.5 nm GaAs SQW (sample A), an fifth order nonlinear optical process in the absorption spin beats is observed in two-pulse DA, as shown in Fig. 32. Similar phenomena are also observed with an un-doped 13 nm GaAs MQW (sample B).

The transient DA spectra in Fig. 32 can be numerically fit to the model equation

$$\begin{aligned}
 -\Delta\alpha L \simeq \frac{\Delta T}{T} = & A_b + A_0 \exp\left[-\frac{\tau}{T_0}\right] + A_1 \exp\left[-\frac{\tau}{T_1}\right] \\
 & + A_T \exp\left[-\frac{\tau}{T_2^*}\right] \cos(2\pi\omega_L\tau)
 \end{aligned} \tag{7.3}$$

In this model $\tau = t_1 - t_2$ is the time delay between pump and probe pulse. A_b is obtained from averaging signals of negative τ delay and is treated as a constant background. The fast decay contribution due to coherent interactions of pump and probe field are simply modeled as a single exponential decay term with amplitude A_0 and a decay time constant T_0 . The long-lived incoherent contribution related to population relaxation is modeled as a single exponential decay term with amplitude A_1 and a decay time constant T_1 . The contribution from electron spin coherence is

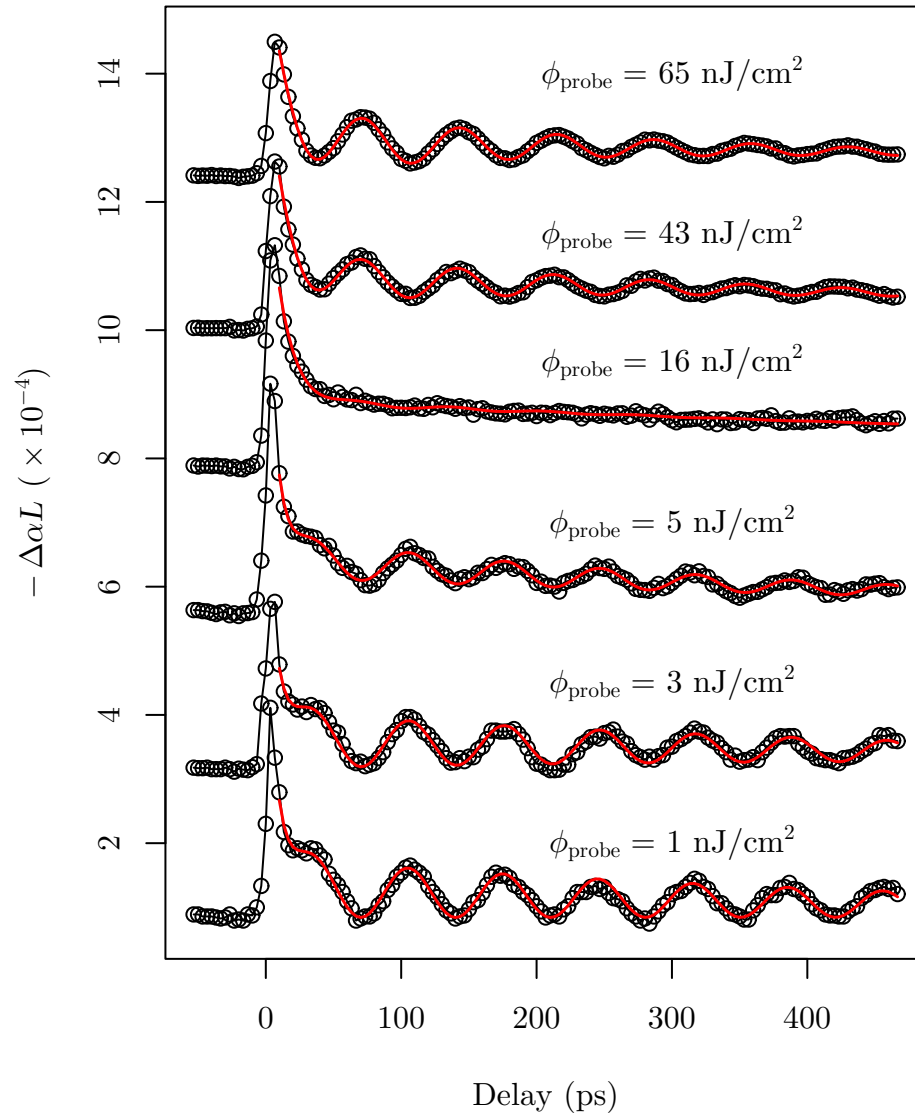


FIGURE 32. Probe intensity dependence of degenerate DA observed from sample A, obtained at 10 K and $B = 3$ T with a pump pulse energy flux density of $\phi_{\text{pump}} = 4$ nJ/cm². The probe intensity is indicated in the figure. The responses are vertically offset for clarity. The solid red lines presents the fitted curves based on Eqn. (7.3).

described by an exponentially damped cosine function, with an amplitude A_T , a spin beating frequency ω_L , and a decoherence time T_2^* .

By numerically fitting the probe intensity dependent data, the spin beat amplitude A_T as a function of probe intensity is plotted in Fig. 33. At low probe intensities, a $\chi^{(3)}$ response was observed, where quantum beat signal, $\Delta T/T$, is independent of the probe intensity. At an intermediate probe intensity, the absorption quantum beats vanish and reemerge with a reversed sign and an overall linear dependence on the probe intensity, corresponding to a $\chi^{(5)}$ process. At higher probe intensity, the quantum beat amplitude reaches a maximum and then decreases at even higher probe intensity. Note that the x -axis has a logarithmic scale.

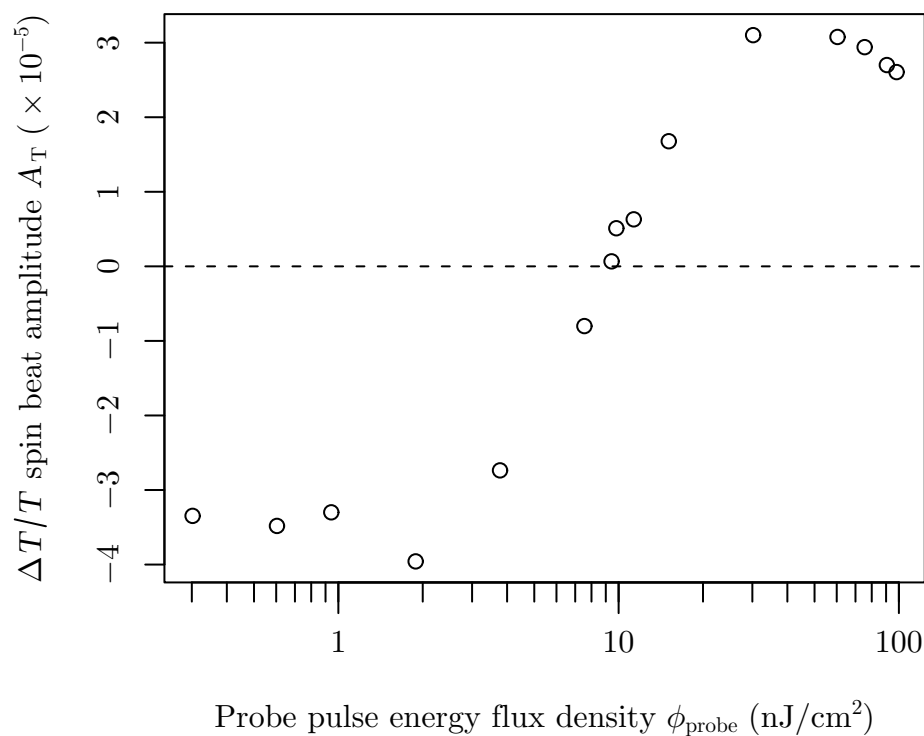


FIGURE 33. Probe intensity dependence of $\Delta T/T$ beat amplitude.

Control Intensity Dependence

The probe intensity dependence shown in previous section can be checked with the three-pulse DA experiment described in detail in Chapter VI. By setting a zero control-probe delay ($\tau_2 = 0$), the probe pulse field in the two-pulse DA experiment is replaced by a combination of both a control and a probe field. By varying the intensity of the control pulse independently to the probe field, the three-pulse DA experiment elucidates the cancellation and enhancement through the coupling of spin coherence and population to the two-exciton states.

Figure 34 shows the results obtained by overlapping the control pulse with the probe pulse in the time domain and by varying the intensity of the control. With both the pump and the probe intensity kept as low as in the third order response regime, nonlinear responses observed exhibit behaviors similar to those in Fig. 32.

Figure 35 plots the amplitude of the quantum beats as a function of the control intensity. As expected, the control intensity dependence is similar to the probe intensity dependence discussed earlier. Figure 34 essentially reproduces the two-pulse experimental results. Together with the two-pulse probe intensity dependence, the observed vanishing and emerging of DA quantum beats experimentally elucidate the cancellation scheme previously discussed.

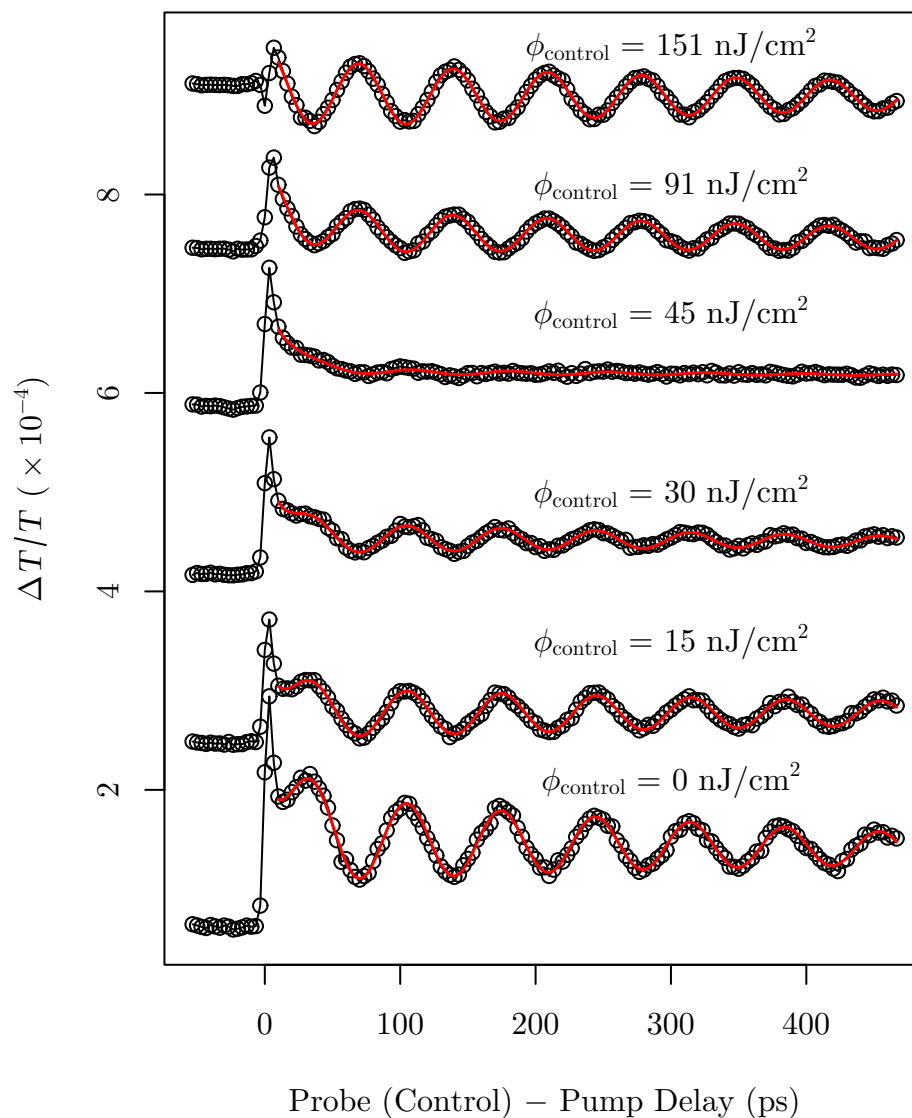


FIGURE 34. Control intensity dependence of degenerate DA of sample A obtained at 10 K and $B = 3$ T with pump pulse energy flux density of 0.8 nJ/cm² and probe pulse energy flux density of 1 nJ/cm². Control pulse energy flux densities are labeled in the figure. The responses are vertically offset for clarity. Red solid lines are results of numerical fits.

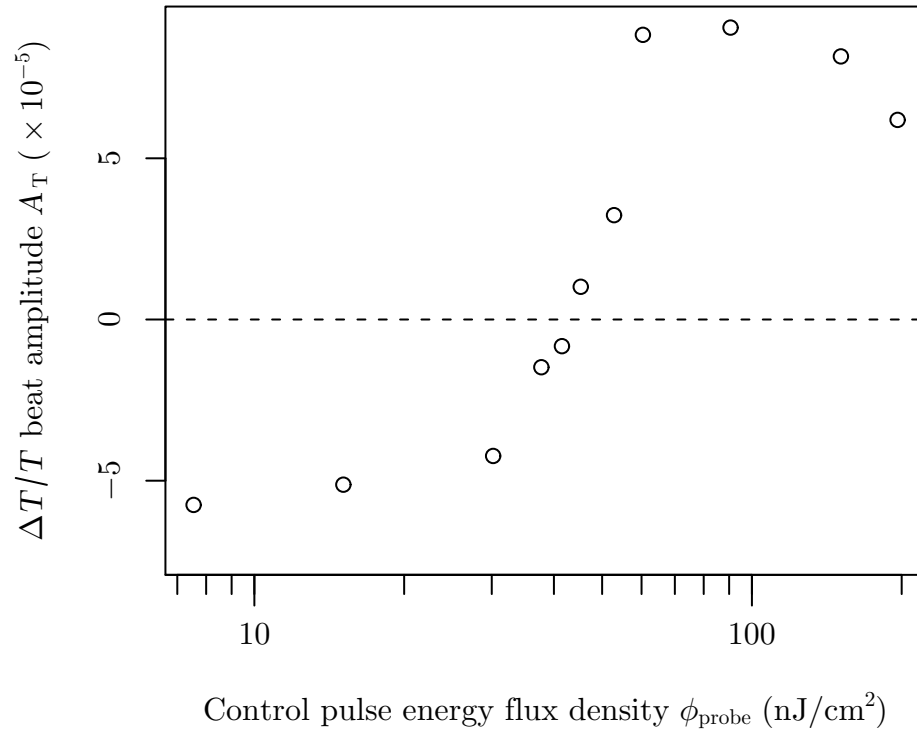


FIGURE 35. Fitted quantum beat amplitudes as a function of control intensity. The degenerate three pulse DA data of the 17.5 nm GaAs SQW (sample A) are obtained at 10 K and $B = 3$ T, with pump pulse energy flux density of 0.8 nJ/cm² and probe pulse energy flux density of 1 nJ/cm². The dashed line indicates the absolute level of quantum beat amplitude in the 3rd order. The dotted lines are guides for the eye.

Spectral Response of Absorption Spin Beats

To obtain a picture of the higher order nonlinear processes associated with the two-exciton state in spectral domain, a combination of two-color pump and probe experiment and three-pulse measurement was carried out. In this experiment, the pump field is positioned at the HH absorption line center. The probe and control is degenerate in energy. The delay between the probe and control are set to zero. The

spectral position of the probe and control is tuned cross the HH transition to obtain a series of 41 quantum beat responses at different probe (control) detuning. By fitting each of those responses with Eqn. (7.3), a spectrum of A_T is obtained. Figure 36 shows the spectral response of the DA quantum beats amplitude as a function of detuning between the probe and pump at different control intensities obtained with a 17.5 nm SQW (sample A).

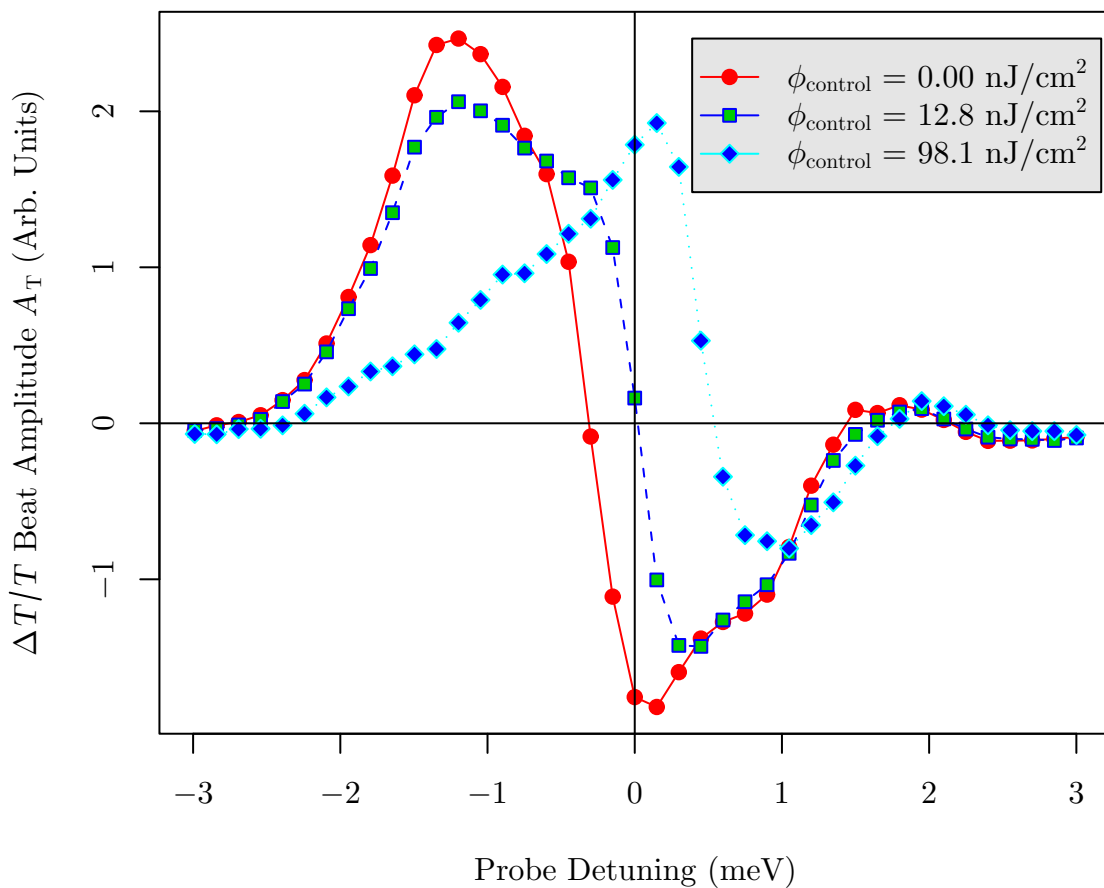


FIGURE 36. Control intensity dependence of the DA spectral response of sample A obtained at 10 K and $B = 3$ T, with pump pulse energy flux density of 0.8 nJ/cm^2 and probe pulse energy flux density of 1 nJ/cm^2 .

The spectral DA response in Fig. 36 reflects contributions from the coupling of the electron spin coherence to the ground state as well as the unbound two-exciton states. As discussed earlier (also see Fig. 31), the two contributions have the opposite sign and feature slightly different resonance frequencies, leading to a dispersive DA lineshape. At a high excitation level, the two-exciton states shift to higher energy. The corresponding shift in the DA lineshape reflects the underlying manybody interactions.

The coupling of control and probe field to the ground state and two-exciton states also depends on the polarization of the optical fields. Figure 37 shows that two different combinations of field polarizations give opposite quantum beat amplitudes over the whole spectra. Note that for these measurements, the probe fields have the same polarization as the control fields. The DA spectrum obtained with mixed field polarizations involves coupling of electron spin coherence to spin-flipped hole states, which will not be discussed in detail here.

Explicit Observation of a $\chi^{(5)}$ Quantum Beat

The spin precession control scheme presented in the previous chapter shows the data obtained with a fixed control–probe delay. The higher order contributions from the parallel spin components, i.e., from the coupling of the spin population terms to the strongly correlated two-exciton states, dominate the signal only at high control

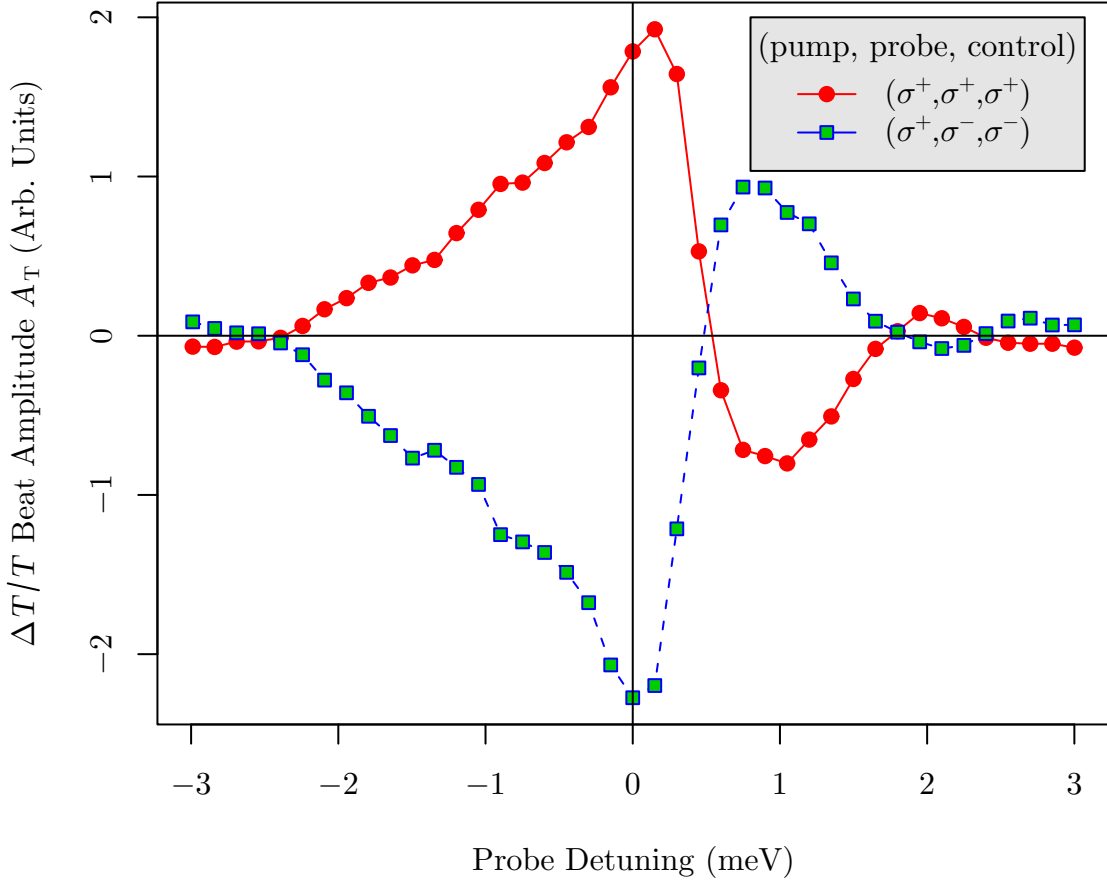


FIGURE 37. Control field polarization dependence obtained in sample A at 10 K and $B = 3$ T, with pump pulse energy flux density of 0.8 nJ/cm^2 and probe pulse energy flux density of 1 nJ/cm^2 . Control pulse energy flux density were 98.1 nJ/cm^2 for both polarizations.

intensities. According to Eqn. (6.3), by fixing the delay between probe and pump, a parallel component can be explicitly observed. The nonlinear optical response from the perpendicular spin component leads to a flat background in this case.

Figure 38 shows a measurement with a fixed probe–pump delay at $\omega_L \tau_1 \simeq 6\pi = 210 \text{ ps}$. The parallel components are readily observed at low control intensities. This

allows direct probing of contributions from the population terms and their dynamics in the time domain. One can see that the parallel component is linearly dependent on the control intensity when the control intensity is low, which indicate a pure $\chi^{(5)}$ process.

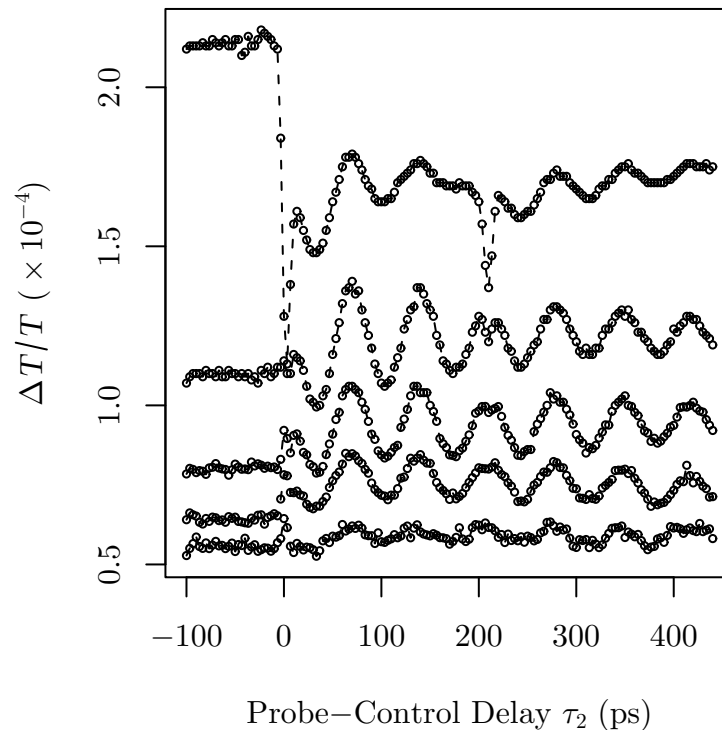


FIGURE 38. Control intensity dependence of DA response with a fixed pump–probe delay, $\tau_1 = 210$ ps, and scanning the control pulse. Data were obtained at 10 K and $B = 3$ T with sample A, with pump pulse energy flux density of 4 nJ/cm^2 and probe pulse energy flux density of 2.7 nJ/cm^2 . The control pulse energy flux used in each data from the bottom to the top curves are ϕ_0 , $4\phi_0$, $8\phi_0$, $12\phi_0$, $52\phi_0$, with $\phi_0 = 3.8 \text{ nJ/cm}^2$. The curves are vertically offset for clarity.

This experiment can also be viewed as scanning control–pump delay, because the delay between the probe and pump is fixed. Three regions can be identified, as

shown in Fig. 39. Region I is for the control pulse arriving at the sample before the pump and probe. In this case, the control field contributes to the second order, and the pump field contributes to the fourth order. Region II is for the control pulse arriving at the sample after the pump but before the probe. Region III is for the control pulse arriving at the sample after the probe pulse, which does not contribute to the signal because the decoherence rate is much larger than the repetition rate of the laser. Region II can be viewed as the time window, within which optical manipulations of spin can be accomplished. The largest possible size of this window is determined by the decoherent rate of the electron spin.

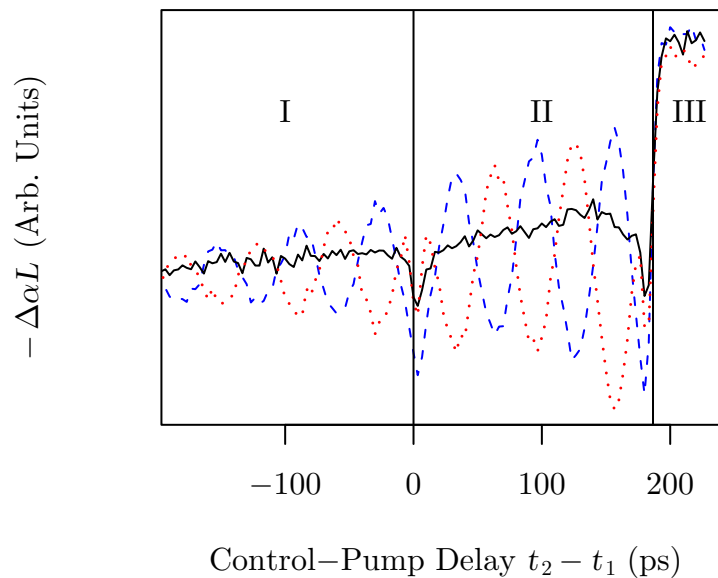


FIGURE 39. DA response with a fixed probe-pump delay, $\tau_1 = 186$ ps, and scanning control pulse. Data were obtained at 10 K and $B = 3$ T with sample A. Pump pulse energy flux density is 0.8 nJ/cm² and probe pulse energy flux density is 1 nJ/cm². The control pulse energy flux used in each data are all equal to 13 nJ/cm². The polarization for pump and probe are both in σ^+ . The control polarizations are linear (solid line), σ^+ (dashed line), σ^- (dotted line), respectively.

Summary

In this chapter we discussed an N -exciton phenomenological model for the understanding of the spin tipping mechanism in the three pulse DA scheme. Coupling spin coherence to the ground state and to the $|\leftarrow, \rightarrow\rangle$ two-exciton state leads to a reduction in the DA response of perpendicular spin component. This can be viewed as an effective increase in the tipping angle of the control pulse in the three-pulse DA experiment. The parallel spin component DA response is enhanced by coupling the spin populations to two-exciton states $|\leftarrow, \leftarrow\rangle$ and $|\rightarrow, \rightarrow\rangle$. Additional experimental results of these nonlinear optical processes are also presented.

As shown in the previous chapter and in this chapter, manybody interactions play an important role in nonlinear optical processes of electron spin coherences in semiconductors. In the following chapter, an experimental study on the effects of exciton interactions in TRFR is presented. It will be shown that compared with DA experiments, these interactions play crucial, but qualitatively different roles in TRFR.

CHAPTER VIII

**CONTRIBUTIONS FROM EXCITON INTERACTIONS OBSERVED
IN TRFR**

The importance of manybody interactions in coherent spin manipulation is already evident in earlier TRFR studies of coherent spin transfer between molecularly-bridged quantum dots [61, 62]. To investigate the roles of exciton-exciton interactions in TRFR, this chapter presents a hybrid time and spectral domain study on the transient spectral responses of quantum beats associated with electron spin coherence. The transient spectral responses are obtained using a two-color pump-probe technique. The observed dispersive responses of spin beats reveal the underlying exciton-exciton interactions through both the bound (biexciton) as well as the unbound two-exciton states.

Two-color Time-Resolved Faraday Rotation

For most studies of spin coherence, performing a degenerate pump and probe experiment is straightforward, in which pump and probe fields come from the same laser and are identical in their spectral lineshape. However, for a nonlinear optical experiment, the spectral response also provides important information about the system's nonlinearity [63]. In the simple limit that the nonlinear optical response arises only from Pauli blocking, the spectral TRFR response should be characterized by a dispersive lineshape centered at the exciton resonance, as one can learn from the numerical simulation shown in Fig. 12(f).

The spectral TRFR response can be obtained with a “two-color” approach. Experimentally, the pump field is positioned at the HH absorption line center. The spectral position of probe is tuned cross the HH transition, to obtain a series of quantum beat responses at different probe detuning. By fitting each of the responses with Eqn. (5.2), a spectrum of A_θ is obtained.

Figure 40 presents a two-color nearly degenerate TRFR spectra of the 13 nm GaAs MQW (sample B) at 10 K with a 3 T magnetic field in x direction. A total of 41 TRFR responses at different probe detunings are plotted in a 2-D color contour graph. A double zero-crossing oscillation phase flip is clearly observed, one at ~ -2 meV detuning on the low energy side, and another one close to zero detuning.

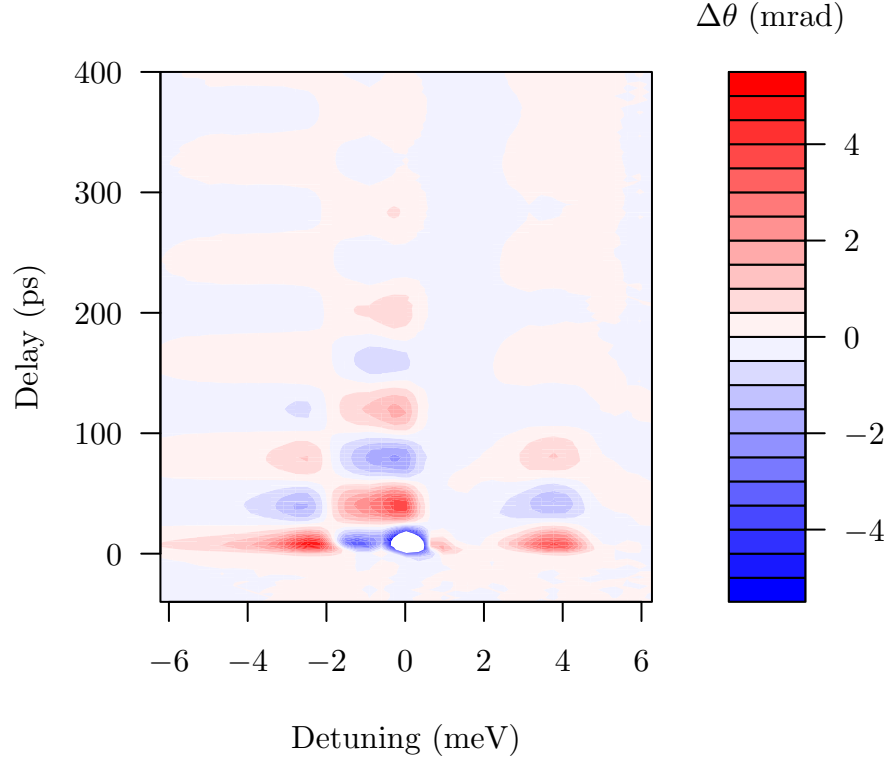


FIGURE 40. Two-color TRFR Spectra of the 13 nm GaAs MQW (sample B) at 10 K, with $B = 3$ T. σ^+ polarized pump pulse energy flux density is $\phi_{\text{pump}} = 5 \text{ nJ/cm}^2$. Linearly polarized probe pulse energy flux density is $\phi_{\text{probe}} = 4 \text{ nJ/cm}^2$. Red color indicates a positive signal. Blue color indicates a negative signal. The white area represents data with an out-of-range negative value compared to the scale on the right side.

Figure 41 shows nearly degenerate TRFR responses obtained from the 17.5 nm GaAs SQW (sample A) at $T = 10$ K and $B = 3$ T. A total of 45 TRFR responses at different probe detunings are plotted in a 2-D color contour graph. For this high quality QW sample, the spectral response of nearly degenerate TRFR is much clearer. Again, a double zero-crossing oscillation phase flip is clearly observed, one at ~ -1.7 meV detuning on the low energy side of HH resonance, and another one close to zero detuning.

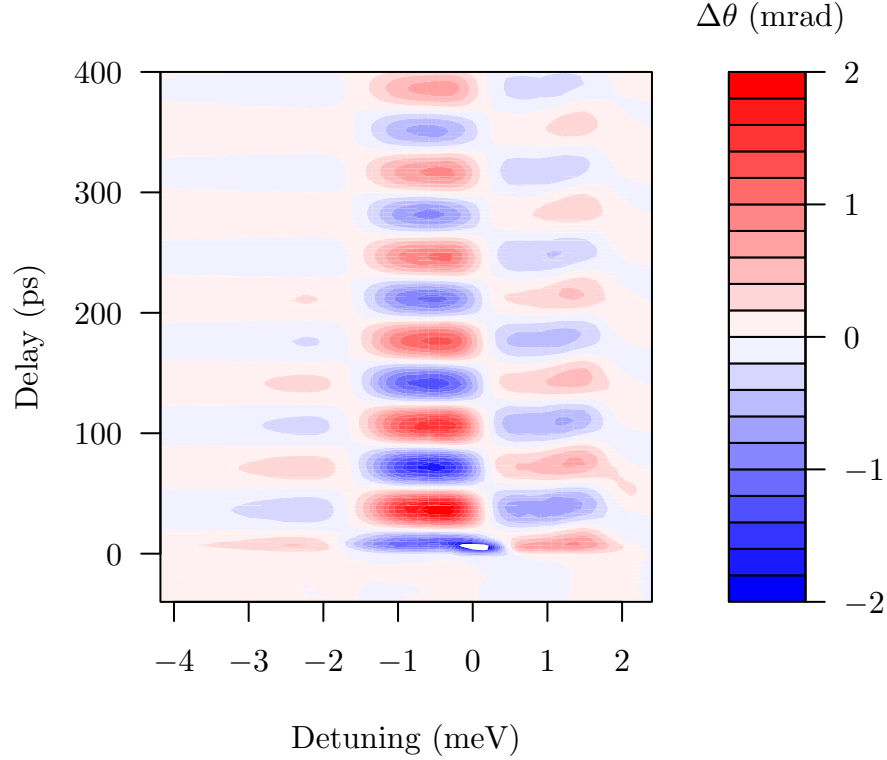


FIGURE 41. Two-color TRFR Spectra of 17.5 nm GaAs SQW (sample A) at 10 K, with $B = 3$ T. σ^+ polarized pump pulse energy flux density is $\phi_{\text{pump}} = 5 \text{ nJ/cm}^2$. Linearly polarized probe pulse energy flux density is $\phi_{\text{probe}} = 4 \text{ nJ/cm}^2$. Red color indicates a positive signal. Blue color indicates a negative signal. The white area represents data with an out-of-range negative value compared to the scale on the right side.

Figure 42(b) plots the spectral TRFR response obtained by numerically fitting the coherent oscillations in the temporal TRFR response. The sign changed twice in A_θ , which indicates that the phase in the oscillation shifted by π twice, at zero and -1.7 meV detuning, respectively. Note that the quantum beats with a probe detuning near the LH resonance is heavily influenced by the LH transition, numerical fits in this spectral region is no longer valid.

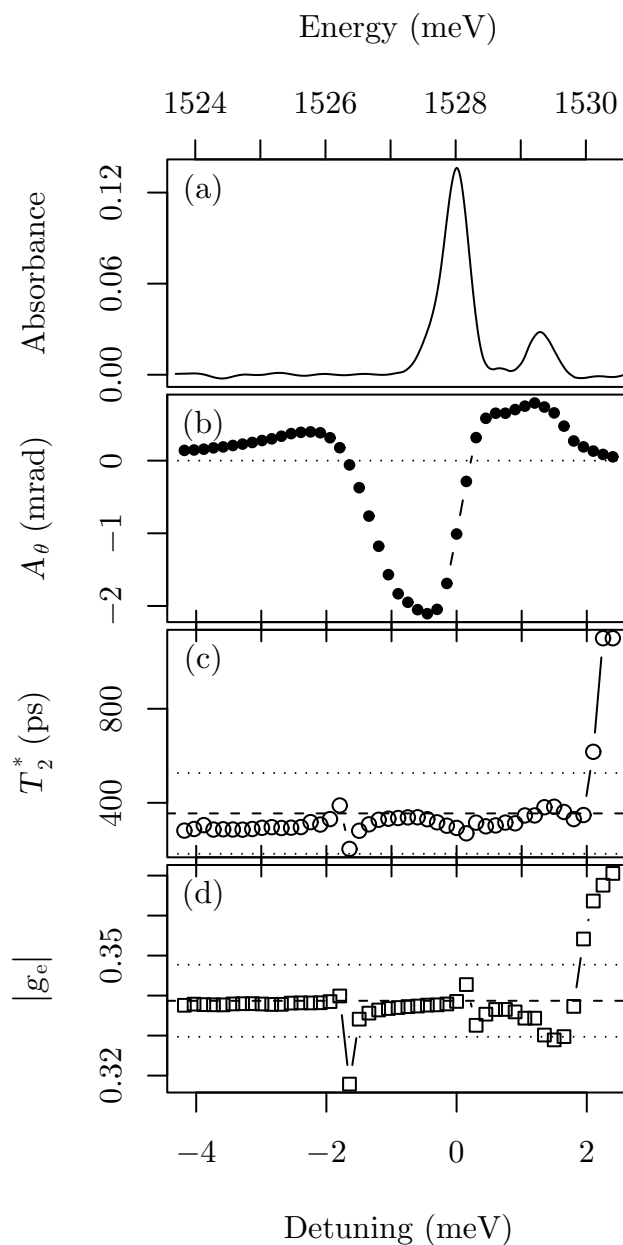


FIGURE 42. The linear absorption (a), spin polarization rotation beats amplitude A_θ (b), transverse spin decoherence rate T_2^* (c), and electron spin g_e factor (d), measured as a function of probe detuning with sample A. Spectra in (b), (c), (d) are obtained by fitting with data in Fig. 41. The dashed line in (b) indicates a zero rotation angle. The dashed lines in (c) and (d) indicate the averaged value over all data points. The dotted lines in (c) and (d) indicate the standard deviation range. All graphs are aligned at same energies.

Figures 42(a) and (b) show that the phase flip close to zero detuning is aligned with the HH resonance energy. It suggests that this dispersive behavior is related to the HH resonance, as described by the simple atomic-like model. As a consequence, the dispersive lineshape at the lower energy side shall arise from another optical resonance. Overall, the observed spectral TRFR response in Fig. 41 can be viewed as consisting of two dispersive lineshapes with opposite dispersion: one centered near the exciton resonance and the other centered near 1.7 meV below the exciton resonance. The dispersive lineshape below the exciton resonance is near the energy of the exciton to biexciton transition, suggesting that the TRFR response is related to biexcitons.

TRFR Response from Bound Two-Exciton States

The formation of bound two-exciton states – biexcitons – can be clearly seen in the counter circularly polarized DA measurements. Figure 43 shows DA spectra obtained at $T = 10\text{ K}$ and $B = 0\text{ T}$. An induced absorption resonance 1.6 meV below the HH exciton resonance appears when the pump and probe have counter circular polarization but vanishes when the pump and probe have the same circular polarization, which clearly reveals the presence of a biexciton state. The induced resonance corresponds to the exciton to biexciton transition. The dispersive lineshape below the exciton resonance shown in Fig. 41 is centered near the energy of the exciton

to biexciton (bound two-exciton) transition, suggesting that this TRFR response is related to biexcitons [64].

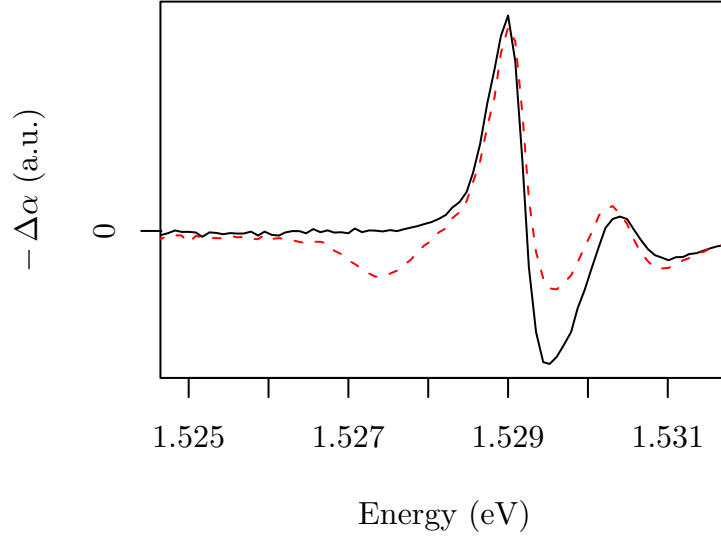


FIGURE 43. DA spectra of sample A obtained at $B = 0$ T and $T = 10$ K where the pump and probe have co- (solid line) and counter-circular (dashed line) polarization.

To describe the contributions of biexciton transitions to TRFR, a phenomenological model based on the N -exciton energy eigenstates is used. Figure 44 shows relevant energy eigenstates and optical selection rules with the crystal ground state $|g\rangle$, single exciton states $|x+\rangle$ and $|x-\rangle$, and a bound two-exciton (biexciton) state $|BX\rangle$.

With a σ^+ polarized pump field, the one-exciton states have the same hole angular momentum $j_z = -3/2$ and electron spins $s_x = 1/2$ and $-1/2$, respectively. In this notation, the electron spin coherence corresponds to a coherent superposition of $|x+\rangle$ and $|x-\rangle$. The optical selection rules are described in Chapter III. The biexciton

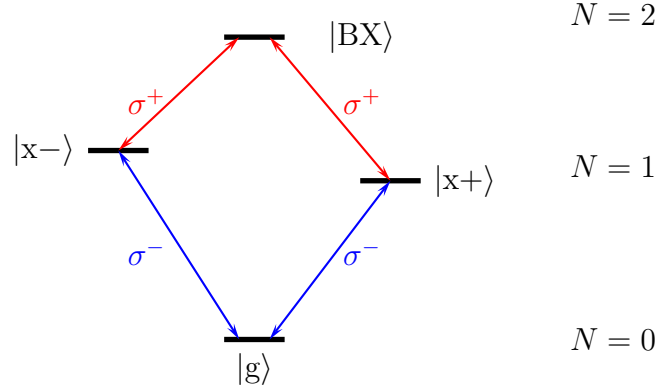


FIGURE 44. Schematic of N -exciton energy eigenstates for σ^- excited HH transitions with related biexciton transitions under Voigt geometry magnetic field.

state, $|BX\rangle$, now involves two two-exciton states characterized by $|s_x = 1/2, j_z = 3/2; s_x = -1/2, j_z = -3/2\rangle$ and $|s_x = -1/2, j_z = 3/2; s_x = 1/2, j_z = -3/2\rangle$, respectively. In TRFR, the linearly polarized probe has both left and right hand circularly polarized components. After the excitation of the spin coherence by the pump, the probe field can couple the spin coherence to the ground state via the one-exciton transitions, and to the biexciton state via the two-exciton transitions. The coupling to the ground state $|g\rangle$ essentially is the V-system discussed in Chapter III. Based on the calculation discussed in Chapter III, this V-system leads to a dispersive lineshape centered near the exciton resonance [62]. Similarly, it can be shown that the coupling to $|BX\rangle$ leads to an opposite dispersive lineshape centered at the biexciton resonance, as a result of an effective Λ -system. The opposite sign of these two

dispersive lineshapes can be understood as following: a stimulated emission process is associated with the coupling of spin coherence to $|g\rangle$ by the probe field, while a stimulated absorption process is associated with the coupling of spin coherence to $|BX\rangle$ by the probe field. After including the contributions of the relevant biexciton transitions using effective density matrix equations, the calculated spectral TRFR response is shown in Fig. 45(b). In comparison, the calculated spectral TRFR response without considering biexcitons is shown in Fig. 45(a). A linewidth of 2γ was used for both excitons and biexcitons. The biexciton binding energy was set to 3.5γ . The calculated lineshape qualitatively matches the experimental data shown in Fig. 42(b).

TRFR Response from Unbound Two-Exciton States

The above model has not included contributions from unbound two-exciton states. In addition, the TRFR response at the HH transition is also complicated by contributions from the nearby LH transitions. To elucidate the roles of unbound two-exciton states in TRFR, a 8 nm InGaAs MQW (sample C) is used for the two-color TRFR study. The HH absorption line of the InGaAs MQW is well-isolated from LH transitions. This allows a spectral response study without complications due to LH transitions.

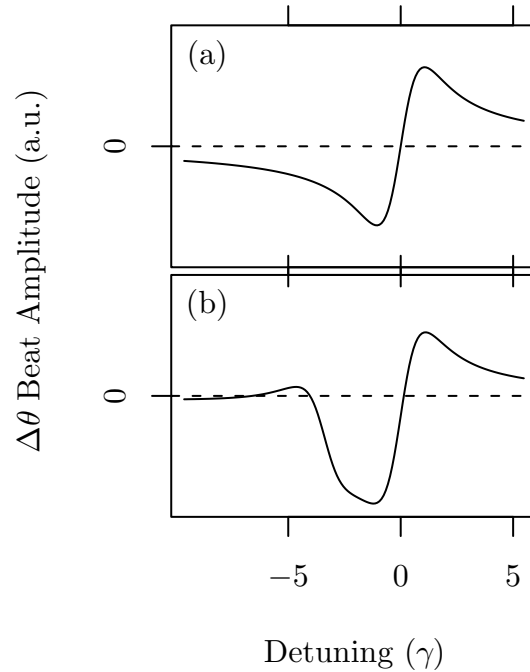


FIGURE 45. Calculated TRFR spectral responses. Upper curve (a) is without considering biexcitons. Lower curve (b) is after considering biexciton contributions.

A biexciton resonance for sample C with a binding energy of 1.4 meV is observed at 10 K with $B = 0$ T, as shown in Fig. 46. The spectral TRFR feature at the biexciton resonance is clearly observed at 10 K in Fig. 47, where total of 41 TRFR responses at different probe detunings are plotted in a 2-D color contour graph.

For the TRFR study in Fig. 47, effects of the unbound two-exciton states are masked by dominant contributions from biexcitons. To single out effects of these unbound two-exciton states, experimental studies were carried out in the InGaAs QW at an elevated temperature of 80 K, and the effects of inhomogeneous broadening are minimized as well.

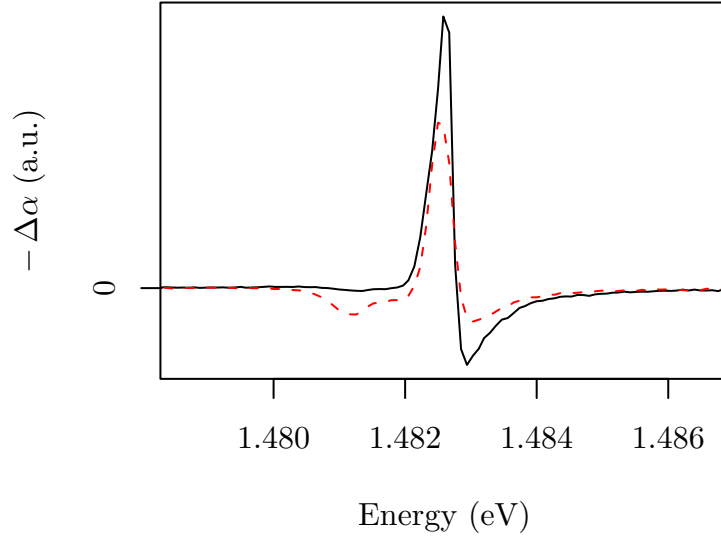


FIGURE 46. DA spectra of InGaAs MQW (sample C) obtained at $B = 0$ T and $T = 10$ K, with a probe which is delayed 20 ps with respect to the pump. The pump and probe have co- (solid line) or counter-circular (dashed line) polarization.

Figure 48 shows nearly degenerate TRFR responses obtained in sample C with $T = 80$ K and $B = 3$ T, with the pump energy fixed at the exciton absorption line center. A total of 41 TRFR responses at different probe detunings are plotted in a 2-D color contour graph. The spectral TRFR response in Fig. 48 still features two dispersive features with opposite dispersion. The dispersive feature at lower energy is centered at 0.7 meV below the exciton resonance, considerably away from the spectral position of the expected biexciton resonance.

The DA spectrum shown in Fig. 49 is characterized by an effective exciton energy shift as well as excitation induced exciton line broadening. The absence of a biexciton-induced resonance indicates that at 80 K the biexciton decoherence rate exceeds or is comparable to the biexciton binding energy. At an elevated temperate of

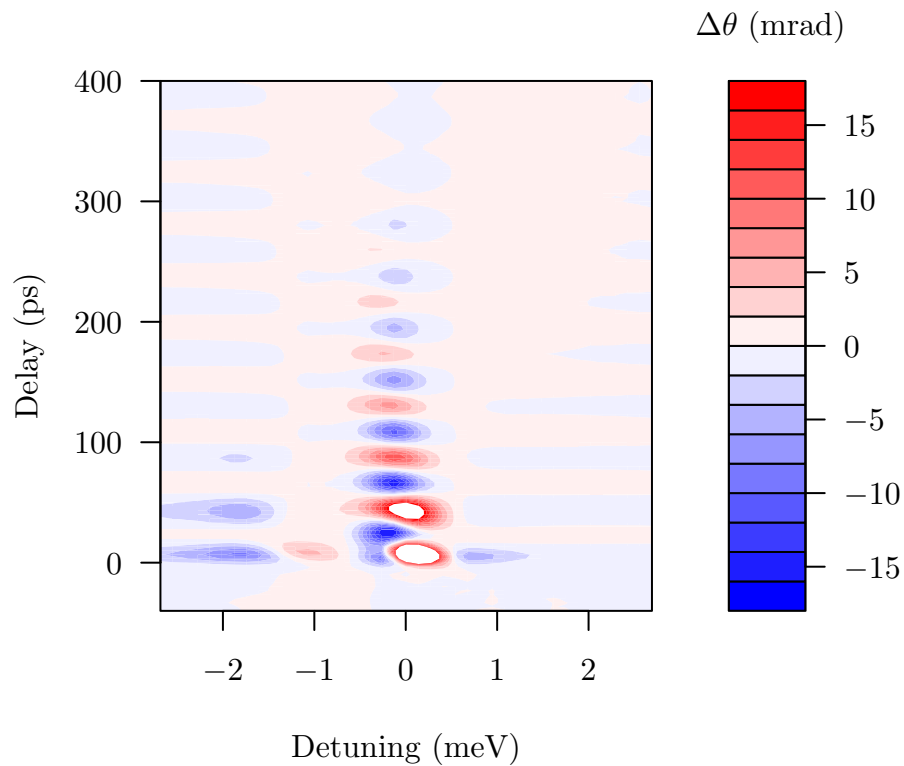


FIGURE 47. Two-color TRFR Spectra of InGaAs QW at 10 K, with $B = 3$ T. σ^- polarized pump pulse energy flux density is $\phi_{\text{pump}} = 8 \text{ nJ/cm}^2$. X polarized probe pulse energy flux density is $\phi_{\text{probe}} = 5 \text{ nJ/cm}^2$. Red color indicates a positive signal. Blue color indicates a negative signal. The white area represents data with an out-of-range positive value compared to the scale on the right side.

80 K, the biexcitons are ionized. The homogeneous linewidth is also large compared with the inhomogeneous linewidth.

The nearly degenerate TRFR response shown in Fig. 48 is numerically fitted to Eqn. (5.2) and the amplitude of quantum beats are plotted in Fig. 50(c). The dispersive spectral TRFR lineshape below the exciton resonance in Figure 48 thus provides unique and valuable information on the underlying two-exciton continuum states, information that is central to the understanding of an interacting exciton

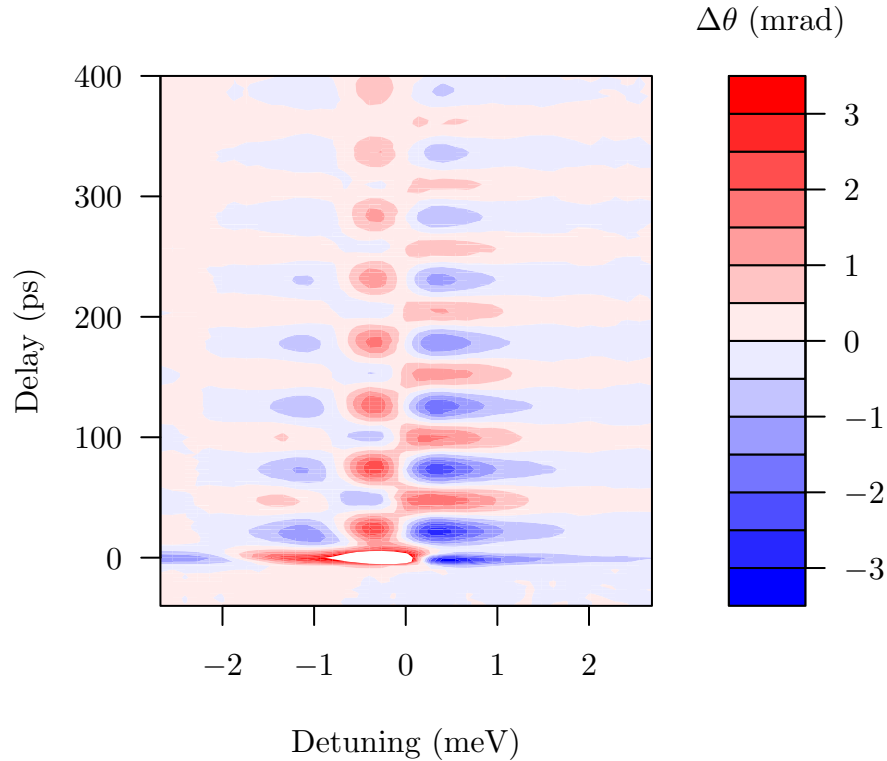


FIGURE 48. Two-color TRFR Spectra of sample C at 80 K, with $B = 3$ T. σ^- polarized pump pulse energy flux density is $\phi_{\text{pump}} = 6 \text{ nJ/cm}^2$. Linearly polarized probe pulse energy flux density is $\phi_{\text{probe}} = 1 \text{ nJ/cm}^2$. The white area represents data with an out-of-range positive value compared to the scale on the right side.

system but is otherwise difficult to obtain. Note that Fig. 50 also shows a comparison of the spectral response of the quantum beat amplitudes observed in TRFR and DA measurements of sample C at 80 K.

Transient DA and TRFR are two closely-related nonlinear optical responses. Previous chapters show that significant higher order optical processes are observed in the DA responses of electron spin coherence, arising from the underlying exciton-exciton interactions. The effects are understood by considering the coupling of electron spin coherence to two-exciton states. In TRFR these two-exciton states also

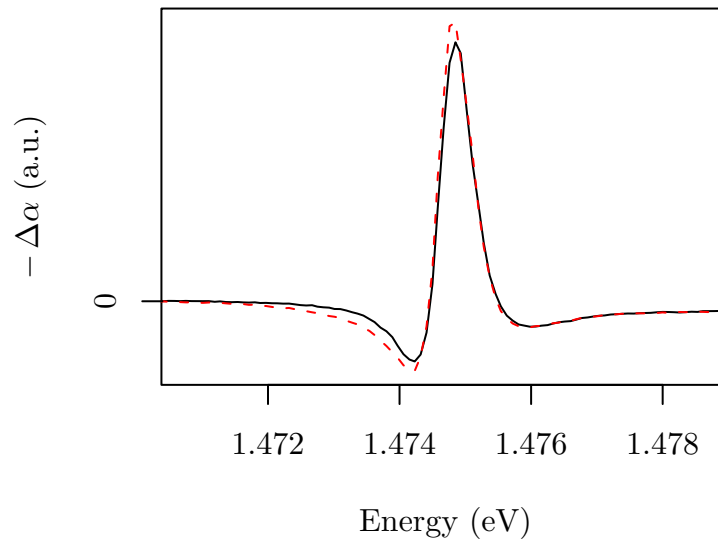


FIGURE 49. DA spectra of InGaAs QW obtained at $B = 0$ T and $T = 80$ K, with a probe which is delayed 20 ps with respect to the pump. The pump and probe have co- (solid line) and counter-circular (dashed line) polarization.

play crucial roles, as shown above. However, the probe intensity dependence of TRFR are very different compared to the DA responses. The following section presents an experimental observation of the difference, and also gives a phenomenological explanation.

Probe Intensity Dependence

Both the TRFR and transient DA measurements are nonlinear optical spectroscopy techniques, where the signal is measured from the mixing of a probe field with a nonlinear polarization created by the pump field. For the studies of electron spin coherence, the optical response is modified by the electron spin coherence and is

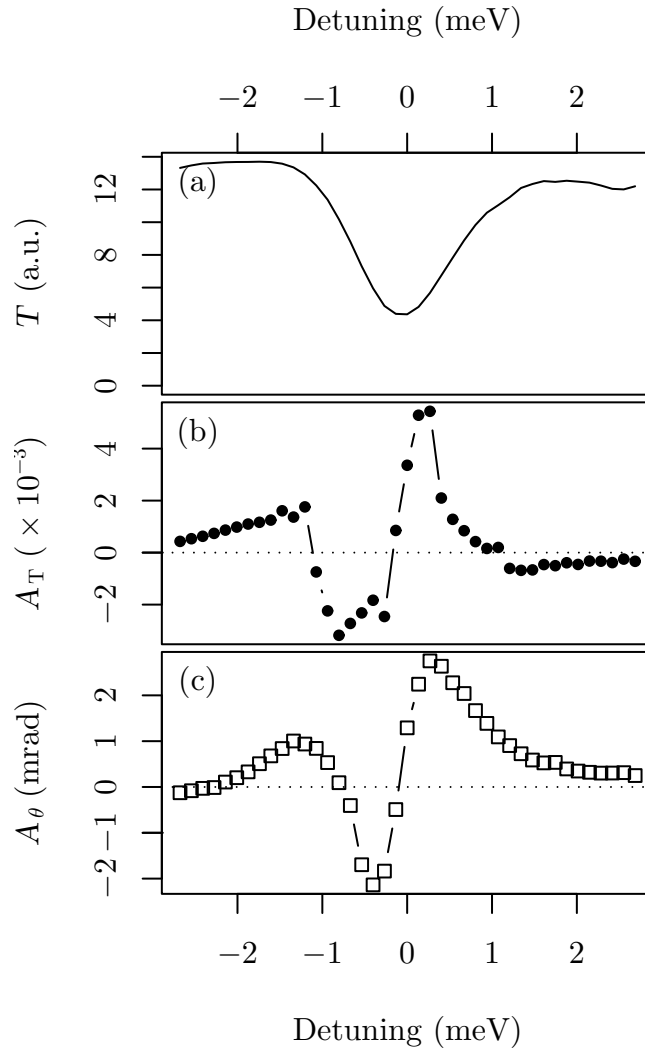


FIGURE 50. A comparison of DA spin beat amplitude and TRFR spin beat amplitude spectra. Obtained from fitting with the data taken with InGaAs QWs at 80 K, with $B = 3$ T. (a) The linear transmission spectrum. (b) The absorption beat amplitude spectrum, with $co\text{-}\sigma^-$ circular polarizations for pump and probe. (c) The polarization rotation beat amplitude spectrum, with σ^- polarized pump and linearly polarized probe. The pulse energy flux density for pump and probe are 6 nJ/cm^2 and 1 nJ/cm^2 , respectively.

probed either through the real part using TRFR or through the imaginary part using transient differential absorption.

However, the unusual higher order optical process shown in Fig. 32 seems to have no effect on the TRFR measurement, as shown in Fig. 51. This figure shows the degenerate TRFR response obtained in sample A at $T = 10$ K and $B = 3$ T, which is under the same condition as in Fig. 32 but with an x -polarized probe. Both the pump and probe were centered at the HH exciton absorption line center.

The TRFR response is independent of the probe intensity at relatively low probe intensities, and only starts to saturate at the highest probe intensities used for the measurement. Since TRFR and DA are determined by the real and imaginary parts of the complex nonlinear susceptibility, respectively, the qualitatively different temporal nonlinear optical behavior featured in TRFR and DA and the apparent lack of any manifestation of exciton-exciton interactions in the TRFR response are striking.

However, considering that for TRFR, contributions from one-exciton and unbound two-exciton transitions have the opposite spectral dispersion, the result shown in Fig. 51 can be explained as follows: the two contributions from one-exciton and unbound two-exciton transitions can interfere constructively near the exciton resonance, if the contribution from the unbound two-exciton states is centered slightly away from the exciton resonance. Due to interactions between excitons, the energy for the two-exciton transition normally differs from the one-exciton transition. In comparison, for DA, contributions from the one-exciton and two-exciton transitions always interfere destructively and can nearly cancel each other near the exciton

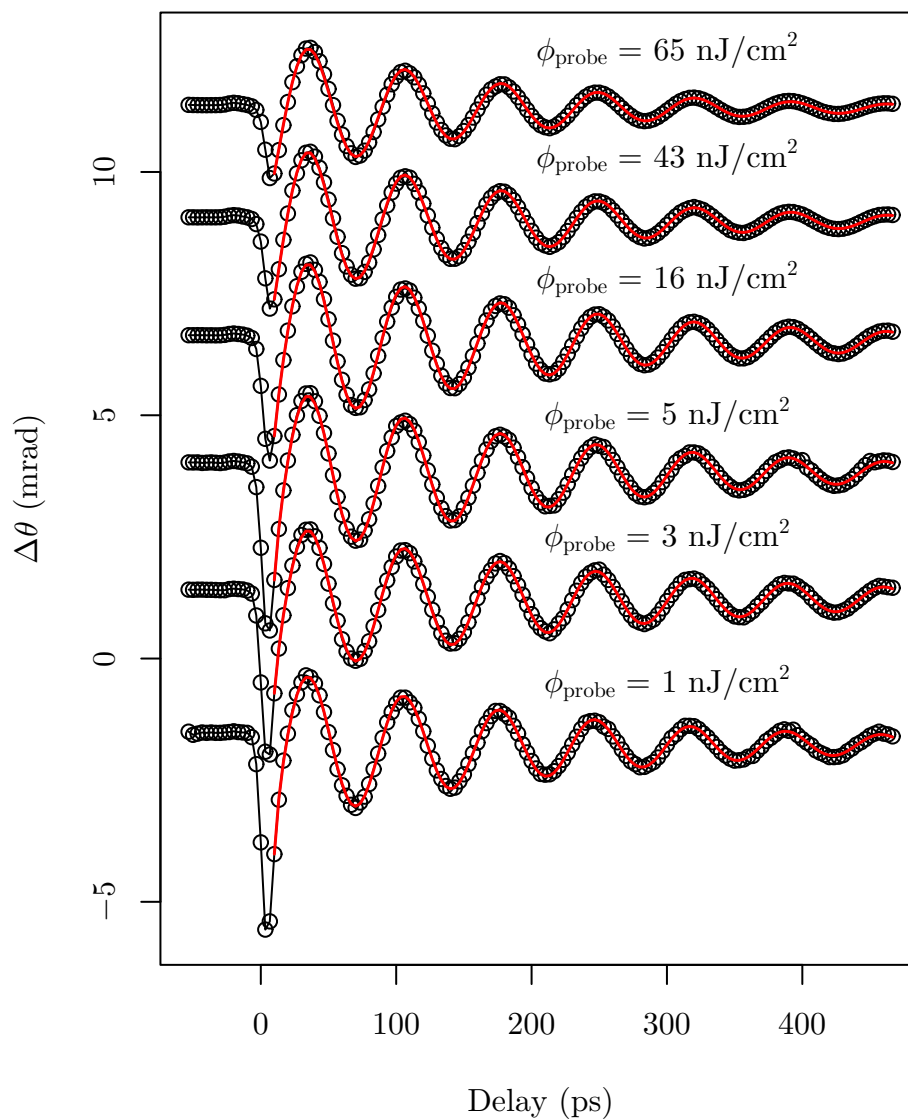


FIGURE 51. Probe intensity dependence of degenerate TRFR of sample A, obtained at 10 K and $B = 3$ T with a pump pulse energy flux density of $\phi_{\text{pump}} = 4$ nJ/cm². The probe intensity is indicated in the figure. The responses are vertically offset for clarity. Red solid lines are results of fits.

resonance, because one contribution leads to induced absorption and the other leads to induced transmission. The consequence of the nearly vanishing third order DA

response is that a fifth order process that does not suffer from the same cancellation becomes important in DA. The striking difference between TRFR and transient DA underscores that exciton-exciton interactions play crucial but qualitatively different roles in TRFR and DA.

Summary

In summary, a nearly degenerate TRFR experiment is used to highlight effects of manybody exciton-exciton interactions in an interacting exciton system. The coupling of the spin coherence to bound as well as unbound two-exciton states strongly modify the TRFR response. These couplings are revealed by distinct lineshapes in spectral TRFR responses, even though the corresponding temporal TRFR response shows no apparent effects of manybody interactions. While TRFR and DA are closely related, exciton-exciton interactions affect these nonlinear optical processes in qualitatively different ways.

CHAPTER IX

OPTICAL TRANSITIONS OF DIAMOND NITROGEN VACANCY CENTERS

The major part of this dissertation is focused on the nonlinear optical processes of the electron spin coherence associated with an excitonic system in undoped GaAs QWs. While huge efforts and interests are focused on the electron spin coherence in semiconductor QWs and other semiconductor heterostructures, a new candidate, the electron spin states of a nitrogen vacancy (NV) center in diamond, has emerged. The NV centers have exceptional spin properties, including triplet spin states as the ground states, and significant longer electron spin decoherence time compared to the electrons in semiconductors [65]. The NV center is a promising system for the optical manipulation of individual electron spin, because it also features a convenient optical transition wavelength (637 nm) with an atomic-like sharp zero-phonon line [66–70]. In addition, coupling the NV centers to an optical cavity also provides access to exciting areas of physics as well as applications [71]. Currently an active cavity QED

study of coupling optical transition of NV in a diamond nanocrystal to a whispering gallery mode in a fused silica microresonator is carrying out in the Wang lab. This chapter presents a preliminary study of the optical properties associated with the electron spin states of NV centers in diamond nanocrystals, using photoluminescence (PL) and photoluminescence excitation (PLE) methods. A zero-phonon linewidth as small as 16 MHz is observed in type Ib diamond nanocrystals at 10 K. This linewidth approaches the nearly lifetime limited linewidth in high purity type IIa diamond.

Nitrogen Vacancy Center

As defect centers in diamond crystals, the NV centers have been studied for a long time. The NV species have many different formations [72], including NV clusters and single NV sites. The single NV center consists of a single substitute nitrogen atom in adjacent to a single carbon vacancy site, as illustrated in Fig. 52.

NV centers can be neutral (NV^0) or negative charged (NV^-), which can be identified by different zero-phonon line emission wavelengths in the PL spectra. Figure 53 shows a typical PL spectrum of NV centers with an excitation wavelength of 532 nm obtained at room temperature. The NV^0 has a zero-phonon line centered at 575 nm, and the NV^- has a zero-phonon line centered at 637 nm. Broad phonon side band emissions dominate the PL spectrum at the lower energy side of zero phonon lines for both NV^0 and NV^- .

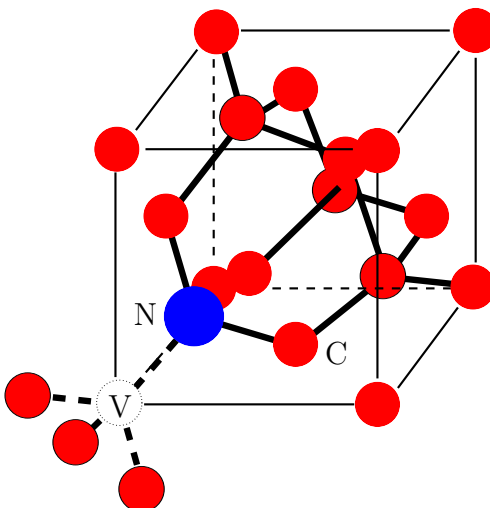


FIGURE 52. Structure of single Nitrogen-Vacancy Center of Diamond.

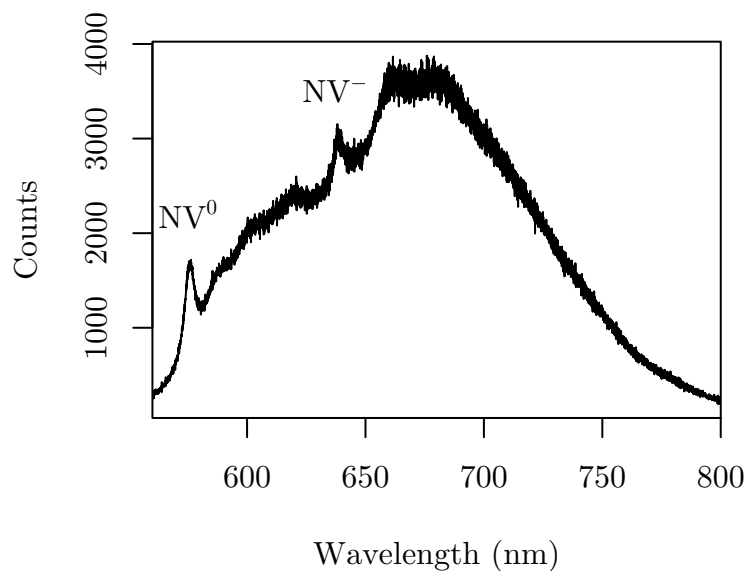


FIGURE 53. A typical PL spectrum of NV centers in diamond nanocrystals obtained at room temperature.

It has been experimentally shown, that the ground states of the NV^- is spin triplet 3A , with a natural spin splitting of 2.88 GHz between $m = \pm 1$ and $m = 0$ states

[73, 74]. The spin splitting can be resolved by microwave electron magnetic resonance experiments. Figure 54 shows the energy diagram of the NV^- . The extremely long spin flipping time and spin decoherence time are in part due to the fact that the spin states are ground states. With a weak external magnetic field the spin states becomes mixed, thus provides a very nice Λ -type three-level system for spin coherence applications. For convenience in the following discussion NV is used to represent NV^- .

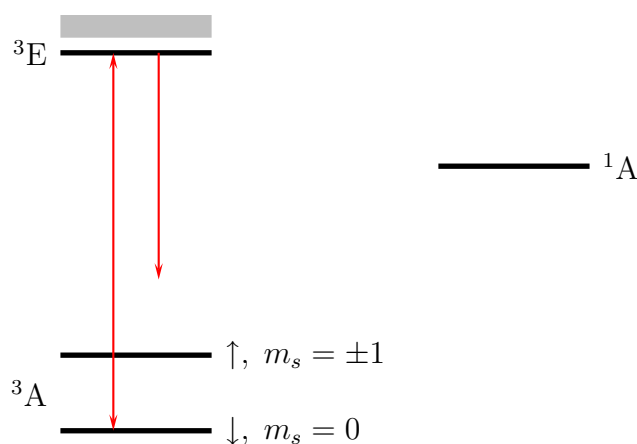


FIGURE 54. The energy diagram of the NV^- transition.

In spite of extensive studies of NV, optical properties of NV centers are still not well understood [75]. The energy level structure of a NV center is complicated by the presence of strain in diamond. The strain along with spin-orbit interactions modifies the excited states, which can lead to enhancement of non-spin-conserving transitions that are otherwise nearly dipole-forbidden [69]. Optical transitions in a NV center

are also complicated by photoionization of nitrogen impurities [76]. The ground state of substitutional nitrogen impurities in diamond is approximately 1.7 eV below the conduction band of diamond. Because the transition energy for the zero-phonon line of a NV center is 1.95 eV, resonant excitation of the NV center can also excite nearby nitrogen impurities. Fluctuating charges in the conduction band of diamond can lead to additional broadening or spectral diffusion of optical transitions in the NV center.

Sample Preparation

NV centers exist naturally in diamond crystals. Based on the abundance of nitrogen and other impurities, diamond is classified as type Ia, type Ib, type IIa and type IIb. Single NV centers are typically found in type Ib and type IIa diamonds. Raw diamond crystal powder is available from industrial vendors such as Element-6, Sun Marketing Group, and Microdiamant, in crystal sizes ranging from tens of microns to nanometers. These synthesized diamond crystals are created using high temperature high pressure methods. Synthetic type Ib diamond has a high concentration of nitrogen impurities, of order 100 ppm.

For the studies in this chapter, the raw diamond crystals were irradiated by a 2 MeV electron beam with an average flux of about 10^{17} electrons per cm^2 . Vacancies are created during the irradiation. The irradiated powder was subsequently annealed in vacuum at 800°C for 2 hours. This allows the vacancies to be captured

by substitutional nitrogen impurities and to form NV centers. Two types of diamond nanocrystals are prepared for this research. The first batch (nanocrystal sample A) is prepared from raw diamond nanocrystals with a size ranging from 0 to 200 nm. The second batch is prepared from raw diamond microcrystals with an average size of 40 μm . The irradiated and annealed microcrystals were then mechanically crushed to yield smaller nanocrystals (nanocrystal sample B).

The prepared nanocrystals were dispersed by sonication in chloroform (CHCl_3). A centrifugation can be performed to select nanocrystals with a proper range of sizes. Scanning electron microscopy (SEM) is used to check the crystal size. The SEM images of diamond nanocrystal samples A and B deposited on a Si wafer, is shown in Fig. 55(a) and (b), respectively.

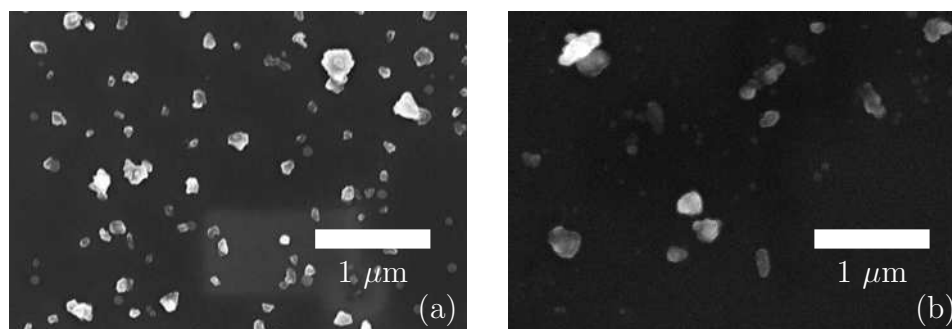


FIGURE 55. The SEM images of diamond crystals deposited on Si wafer. (a) Nanocrystal sample A. (b) Nanocrystal sample B.

Locating NV Centers

The sample was mounted on the cold finger of a liquid helium cryostat. The shroud of the cryostat was remodeled to provide a short distance between the sample and the window, allowing the use of an objective with large numerical aperture (NA). The objective used is an infinity corrected Olympus LUCPLFLN40X 40 \times fluorite objective, with a 3.4 mm working distance, a NA of 0.60 and a 0 mm \sim 2 mm cover class correction collar. The objective is mounted on a 3-D translation stage, which allows the searching of given spots on the sample. The experimental setup is a commonly used confocal design for PL measurement. The PL spectrum is obtained by a spectrometer (Acton Research SpectraPro 2500i) with a charge-coupled device (CCD) array (Princeton Instruments Spec-10). A laser at 532 nm (Coherent Verdi-5) was used for the PL experiments. Typical excitation power on the sample is between 1 μ W and 1 mW.

The microcrystals can be individually identified by the optical microscopy image. The spatial resolution of the optical system is limited by the Rayleigh diffraction disk, which is about the scale of the wavelength. It is difficult to optically image a nanocrystal. To locate the nanocrystals, a scanning imaging technique is used. Instead of scanning the excitation laser beam before the objective, the objective is raster scanned and 532 nm laser is used to excite the NV centers. The emissions from NV centers are detected by a silicon photon-counting avalanche photodiode

(APD, PerkinElmer SPCM-AQR-16) through a multimode fiber coupler. The TTL (Transistor-Transistor Logic) pulses from the APD are counted by a photon counting board (National Instrument PCI-6602) installed in a computer. Filters were used to remove laser scatterings. By diluting the solution and depositing it on a Si wafer with a low density, a single nanocrystal can be investigated on the wafer. Figure 56 shows a scanning 2-D laser fluorescence image from a diluted sample on the Si wafer. With information on the density of nanocrystals on the wafer obtained from SEM images, we can assign the image to a single nanocrystal.

The ability of locating a single nanocrystal on the wafer is important, although using SEM and scanning imaging to individually identify each single nanocrystal before more detailed spectroscopic studies is not necessary. It is because a single nanocrystal is likely to consist of a large number of NV centers. It is possible to identify optical transitions from single NV centers in the spectral domain, i.e., using PLE measurements. However, in practice we still need to keep a small amount of NV centers in the excitation volume, to allow the identification of single NV centers in the experiments discussed later.

Photoluminescence Spectrum of NV Centers in Diamond Nanocrystals

Figure 57 shows the PL spectrum from a treated (before the mechanical crush) $\sim 40 \mu\text{m}$ sized diamond crystal at 7.5 K. The sharp line at 637 nm features a full width

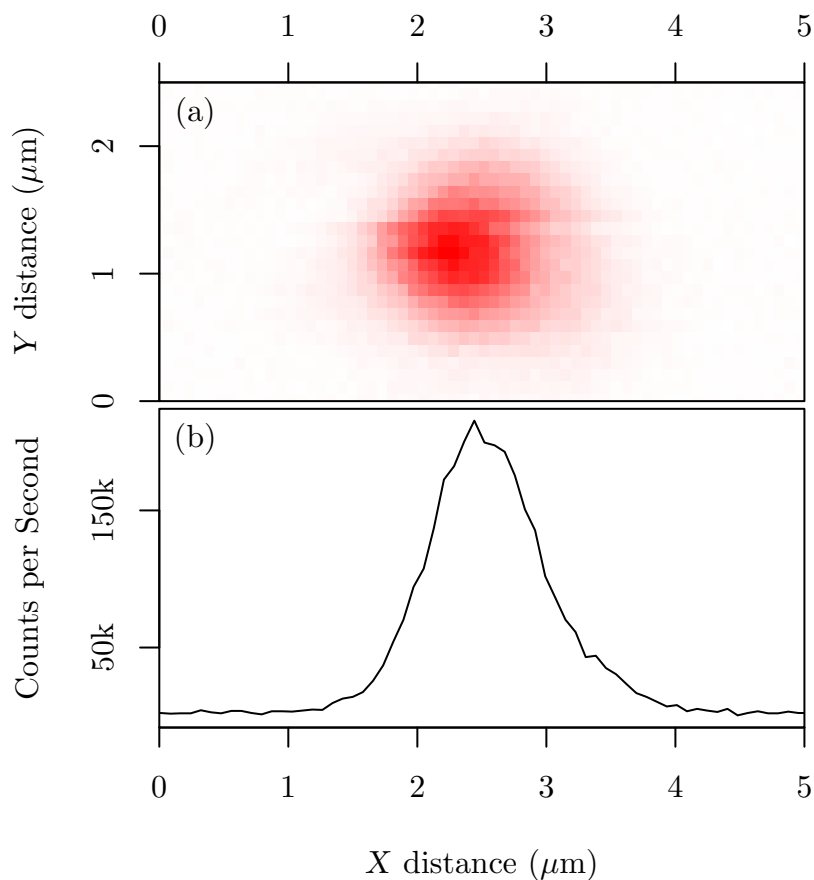


FIGURE 56. Scanning laser fluorescence image of a diamond nanocrystal on the Si wafer. (a) The 2-D image obtained from the raster scan. (b) The cross-section has a spatial width of 840 nm.

at half maximum (FWHM) of 0.36 nm, corresponding to the zero-phonon transition from the NV centers.

Figure 58(a) shows a PL spectrum collected from nanocrystal sample B obtained at 9 K. Multiple emission resonances with the linewidth of individual resonances narrower than that obtained from the microcrystal are observed. The multiple lines pattern is a signature of micro-PL for a system with a homogeneous

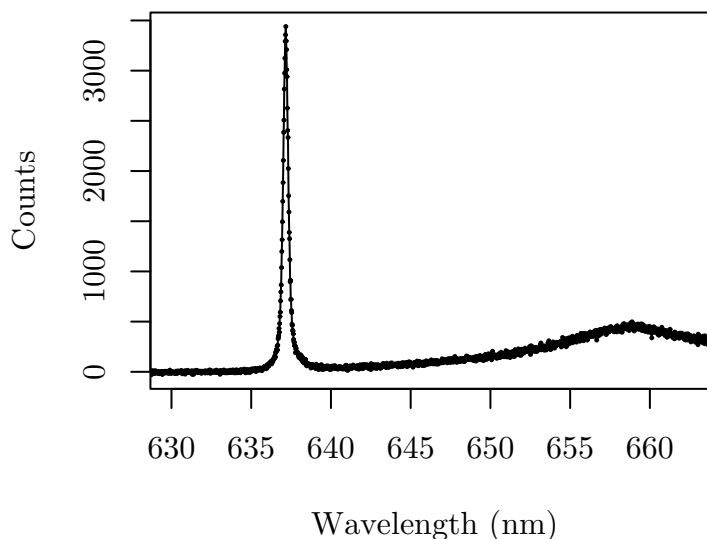


FIGURE 57. PL spectrum of a single diamond microcrystal at 7.5 K with a 1.2 mW 532 nm excitation.

linewidth small compared with the inhomogeneous linewidth, and is commonly observed for many diamond nanocrystals. The linewidth obtained from these narrowed resonances is limited by the spectral resolution of the spectrometer system. Because of the abundance of substitutional nitrogen impurities in type Ib diamond, a single nanocrystal after irradiation and annealing contains a relatively large number of NV centers. The spectral distribution of these NV centers are related to local strains. Local strains induced by the mechanical crushing of the microcrystals lead to significant shifts in the transition frequency of the NV centers. The spectral distribution of NV centers in Fig. 58(a) is about 5 nm, much wider than the linewidth observed in Fig. 57. Figure 58(b) shows a PL spectrum obtained from nanocrystal

sample A at 8 K. A single sharp zero-phonon line is observed, with a linewidth of 0.12 nm (~ 86 GHz), approaching to the instrument spectral resolution limit.

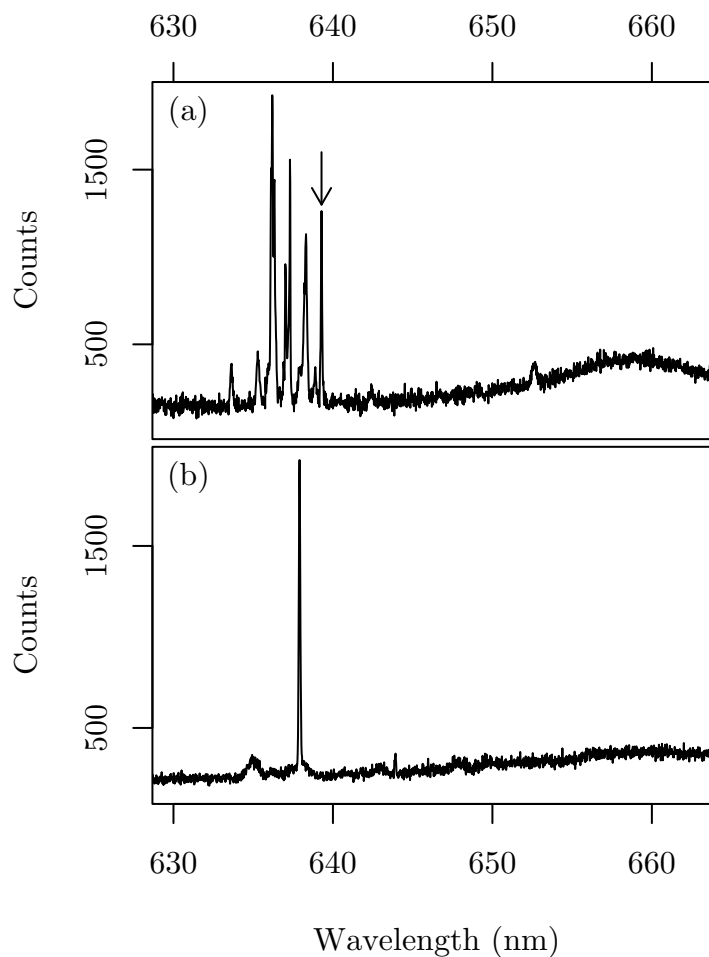


FIGURE 58. (a) Micro PL spectrum obtained with a diamond nanocrystal sample B at 9 K. It shows a large inhomogeneous distribution of NV resonances, where a photon antibunching (shown in Fig. 66) is observed with the 639.2 nm resonance indicated by an arrow. (b) Micro PL spectrum obtained with a diamond nanocrystal sample A at 8 K. It shows a narrow line observed with a linewidth approaching to the instrument resolution limit.

Blinking and Spectral Diffusion

The lifetime limited linewidth of NV centers in diamond is in the order of 10 MHz, which can not be resolved by a spectrometer system. The study of the zero-phonon linewidth is carried out with a PLE setup. Figure 59 illustrates the concepts of PLE. A tunable laser is used to scan across the zero-phonon absorption line. The estimated excitation laser focal spot size is 1 μm . While the zero-phonon transition of the NV centers are excited resonantly, the optical emissions arising from phonon assisted transitions at wavelength longer than 650 nm were detected with a photon-counting APD. Both holographic notch filter centered at 637 nm and red-pass filters were used to reject stray laser scattering as well as Raman scattering.

The lasers used for PLE measurements are a tunable diode laser (New Focus Velocity Model No. 6304) or a ring-cavity frequency-stabilized tunable dye laser (Coherent 899-21). The diode laser can be tuned continuously from 632 nm to 638.3 nm, and by an internal piezo to achieve a fine range of 80 GHz, with a typical output power of about 5 mW and a linewidth <300 kHz. The dye used in the dye laser is Exciton Kiton Red 620. The dye laser was operated in single mode, and was frequency-locked to an external reference cavity, with a tuning range of 30 GHz and a linewidth <1 MHz. The frequency scan was performed by an external triangle ramp voltage waveform provided by an function generator (Agilent 33120A). The photon

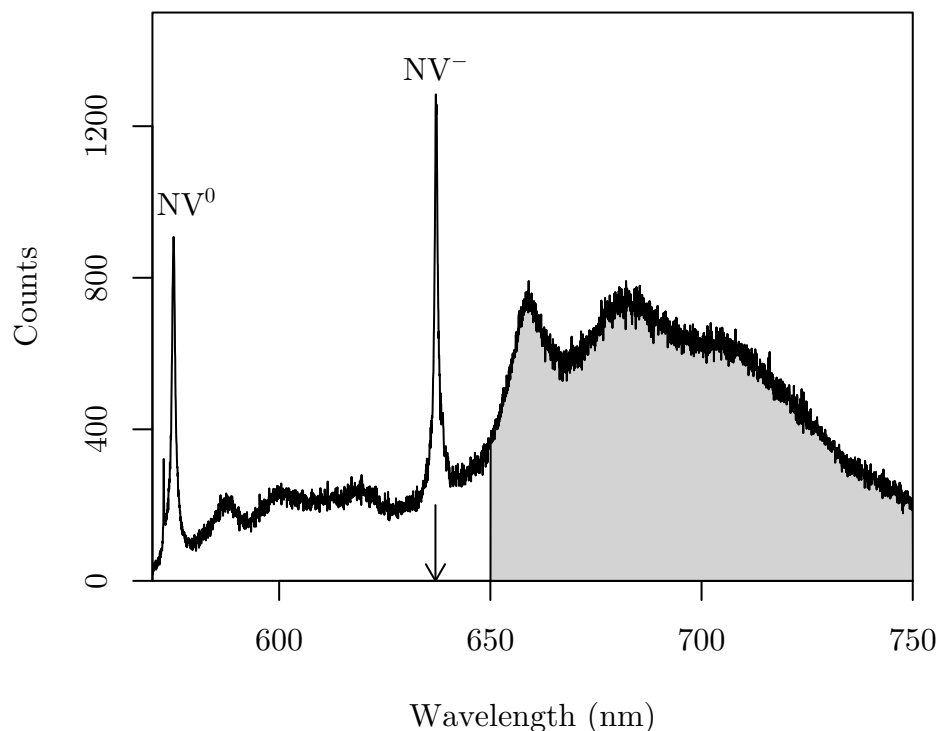


FIGURE 59. A PL spectrum obtained from a collection of a large amount of nanocrystal sample A at 10 K. PLE is done by scanning a laser cross the NV^- zero-phonon absorption line indicated by the arrow. The emissions from phonon side bands at wavelength longer than 650 nm (shaded area) are detected.

counting board installed in the computer counts the TTL signal pulses from the APD and also triggers the function generator to synchronize the external scan.

Repeated single scans of PLE spectrum obtained with a diode laser are shown in Fig. 60. Each scan took approximately 2 seconds. In a single scan, the laser frequency shift varied from 40 GHz to 0 GHz and then back to 40 GHz again. Accordingly, the two resonances shown in each scan of Fig. 60 correspond to emissions from the same NV center. More data like that shown in Fig. 60 is alternatively

visualized in Fig. 61(b). By averaging over the all traces, a linewidth of about 824 MHz is obtained, as shown in Fig. 61(a).

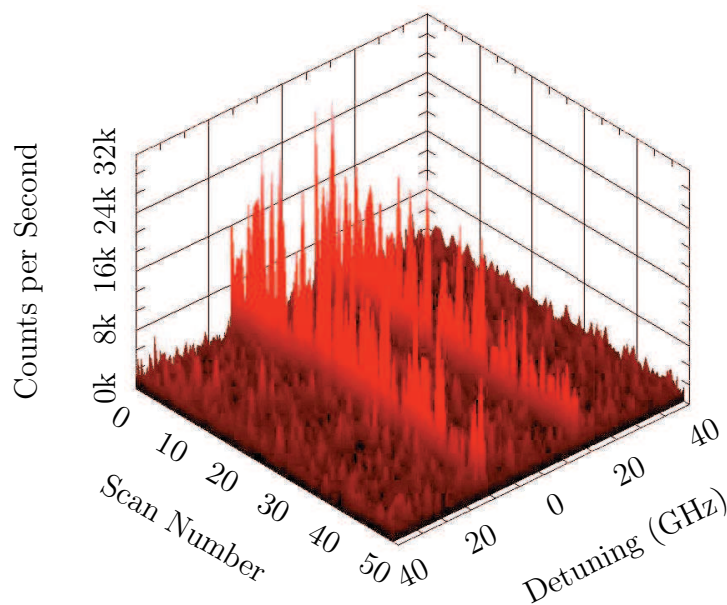


FIGURE 60. A blinking NV center observed in repeated PLE scans. Data obtained from nanocrystal sample B at 10K, with an excitation laser power of 200 nW. The two peaks correspond to emissions from the same NV center.

In this observation no optical re-pumping was used during or between the scans. The NV center remained bright during the hundreds of repeated scans, although both the amplitude and spectral position of the NV emission fluctuated. Bleaching of the NV center was also observed after about one hour of repeated scans. Since the occurrence of a spin-non-conserving transitions will put the NV center in a dark state, the PLE scans in Fig. 60 indicate that the particular NV center can undergo many cycles of spin-conserving transitions without incurring spin-non-

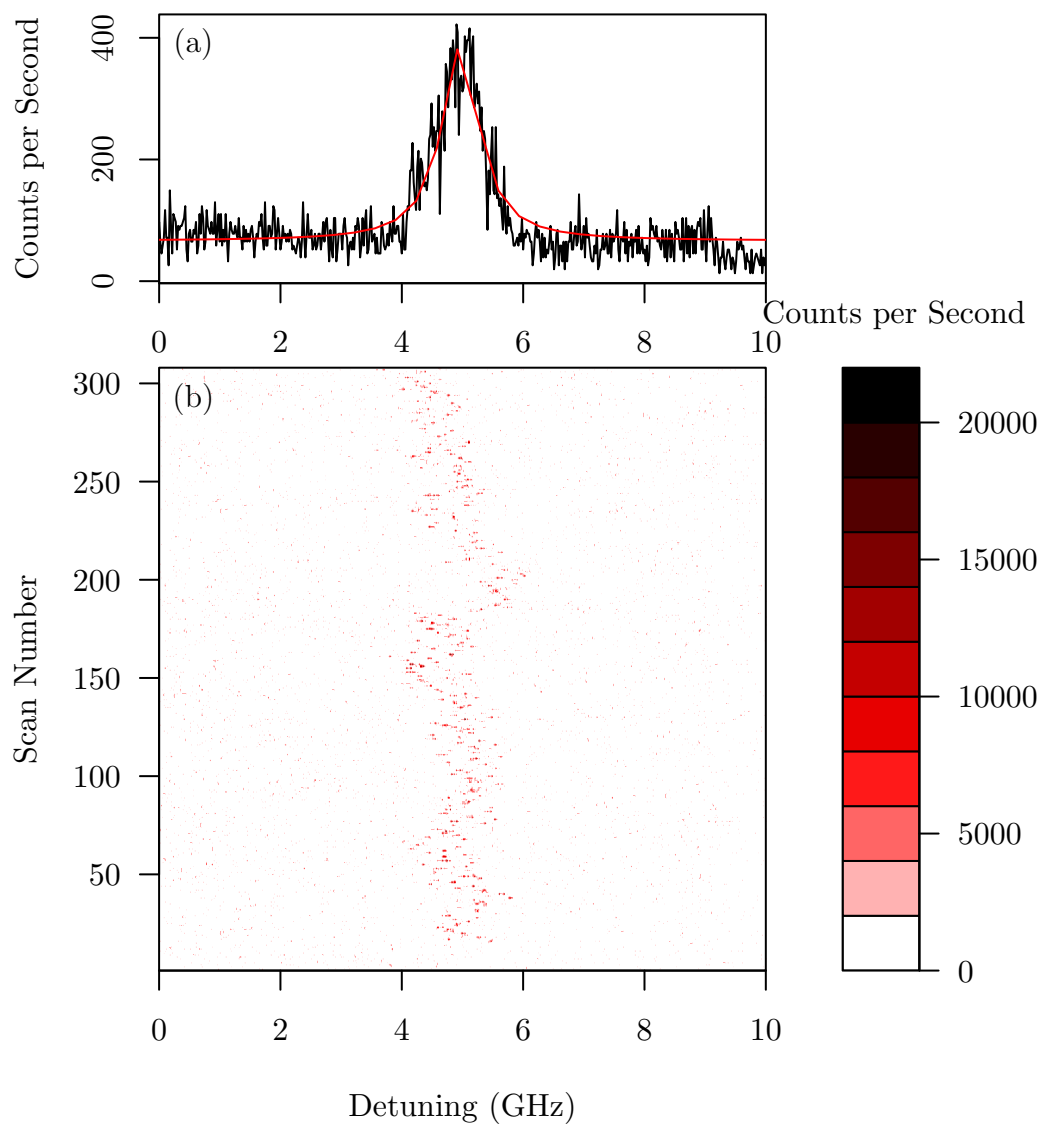


FIGURE 61. Repeated scans of PLE obtained at 10 K from nanocrystal sample B, with an excitation laser power of 200 nW is shown in (b). The averaged spectrum is shown in (a).

conserving transition. Note that the fluctuation in the spectral position observed in Fig. 60 is in part due to the drift in the diode laser frequency during the extended measurements.

For a better frequency stability, PLE studies have also been carried out by using the frequency-stabilized dye laser. Figure 62 shows repeated single scans of PLE obtained with nanocrystal sample B at 10 K. The scan speed is 368 MHz per second. Laser power is 300 nW. No optical re-pumping was used during or between the repeated scans. Most of NV centers incurs spin-non-conserving transition, after which the NV centers are in an inactive dark state.

Nevertheless, two NV centers (enclosed in dashed boxes of Fig. 62) are found to have relatively small effects of spectral diffusion during repeated scans. Three representative single PLE scans from an expanded plot the Fig. 62 are also shown in Fig. 63.

The non-Lorentzian lineshape of the PLE spectra in Fig. 63 indicates small spectral shifts of the NV transition frequency while the laser was scanned across the zero-phonon resonance. For a NV center in a particular individual nanocrystal, it is possible that after irradiation and annealing, most nearby nitrogen atoms have formed NV centers, leading to relatively small effects of photoionization of nitrogen impurities. Note that while this NV center exhibits only a limited amount of spectral diffusion, it spent significant amount of time in dark state, likely due to spin-non-conserving transitions. The lineshape of the first PLE spectrum in Fig. 63 also

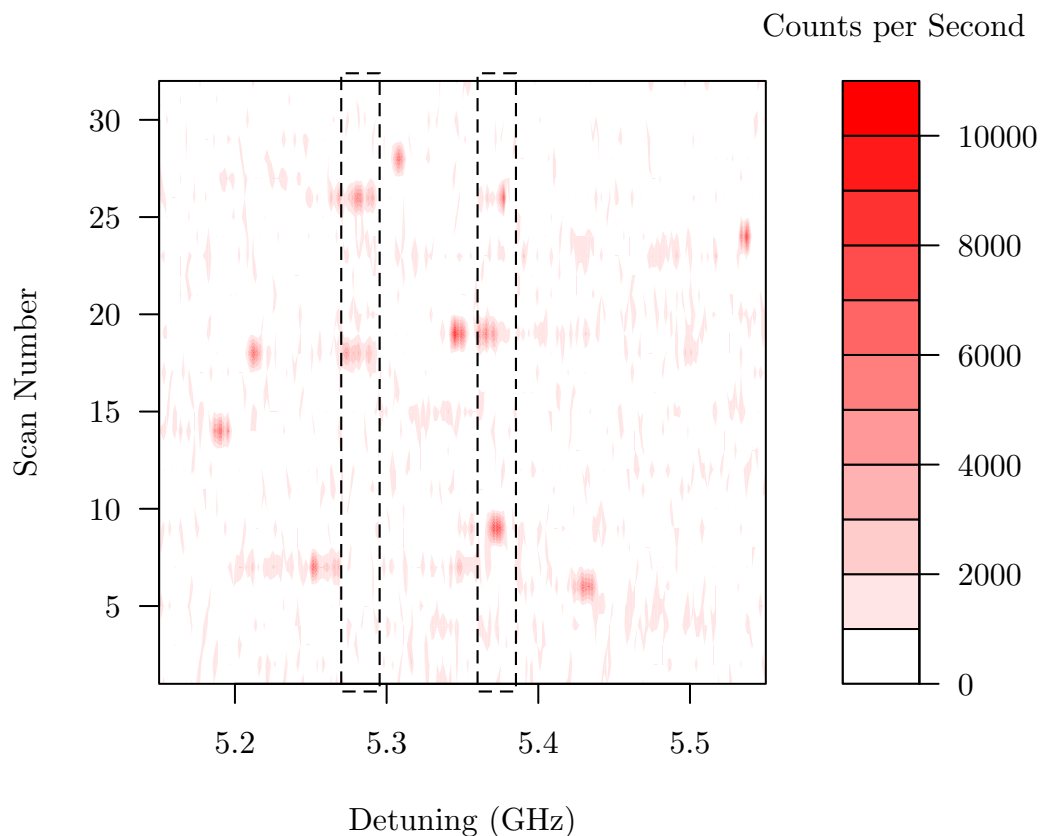


FIGURE 62. Repeated scans of PLE obtained at 10 K from nanocrystal sample B, with an excitation laser power of 300 nW using a dye laser.

suggests that the NV might have undergone a spin-non-conserving transition when the laser was scanned across the zero-phonon resonance.

A PLE scan from another NV center from the data shown in Fig. 62 is shown in Fig. 64. It features a Lorentzian-like lineshape. From the numerical fitting, a FWHM of 16 MHz is obtained, approaching the narrowest and lifetime limited homogeneous linewidth obtained from NV centers reported for bulk high purity type IIa diamond [77]. It indicates negligible effects of spectral diffusion during the time when the laser

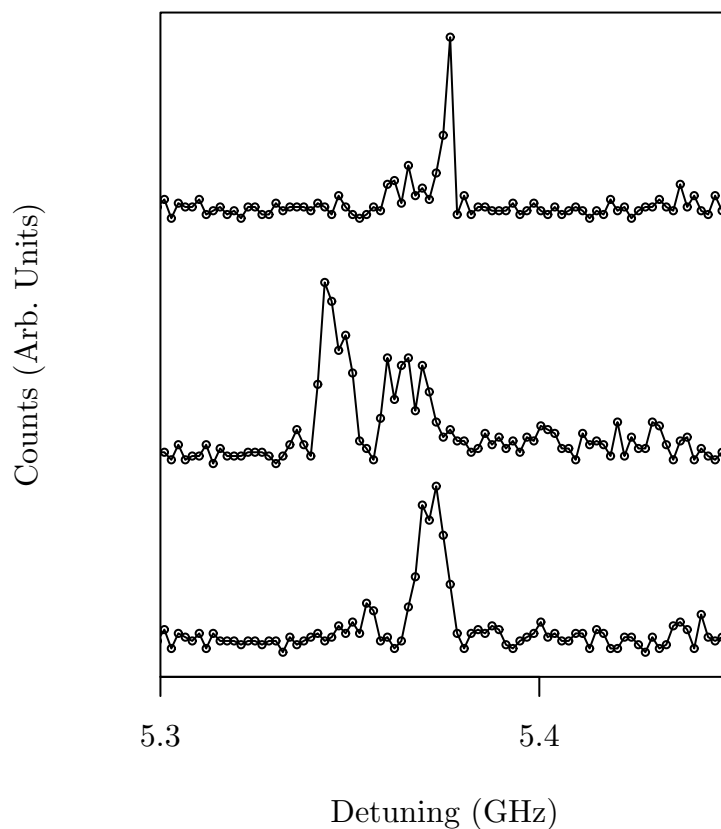


FIGURE 63. PLE spectra obtained at 10 K from nanocrystal sample B. The three representative scans are vertically offset for clarity.

was scanned across the resonance. However, this NV center showed relatively large spectral shifts after repeated PLE scans.

An inactive NV center with large spectral diffusion would be extremely hard to track experimentally. In this research, only a very small number of NV centers remain bright or exhibit only small effects of spectral diffusion during repeated PLE scans. However, our results show that a stable and active NV center can be found in type Ib diamond nanocrystals. Current results suggest that the properties of the NV

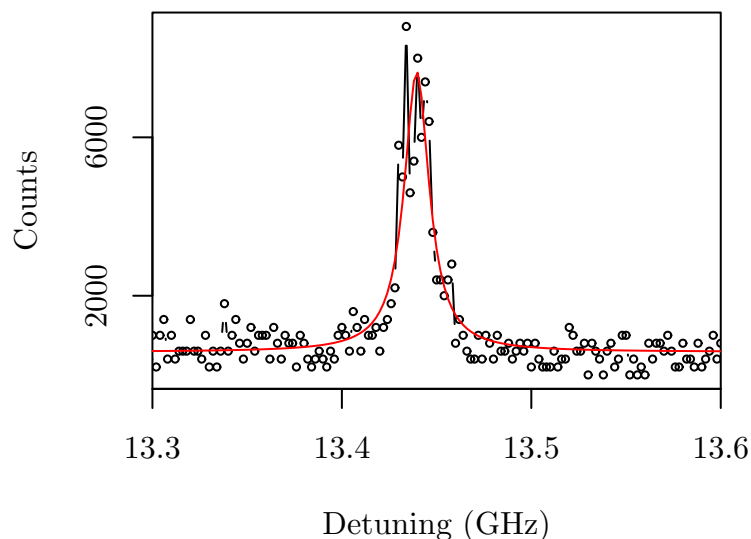


FIGURE 64. PLE spectrum of a zero phonon-line transition from a NV center at 10 K. A Lorentzian lineshape fitting is shown in red solid line, with a linewidth of 16 MHz.

centers may be sensitive to details of the sample preparation. Further development on sample preparation may greatly improve the optical properties of NV centers in nanocrystals.

Photon Correlation of NV Emission

In addition to PL and PLE studies, a $g^{(2)}$ photon correlation study is carried out to confirm a single NV center emission. Figure 65 shows photon antibunching observed from a single diamond nanocrystal, with a small dip at zero delay. This indicate a small number of emitters in the excitation/collection volume.

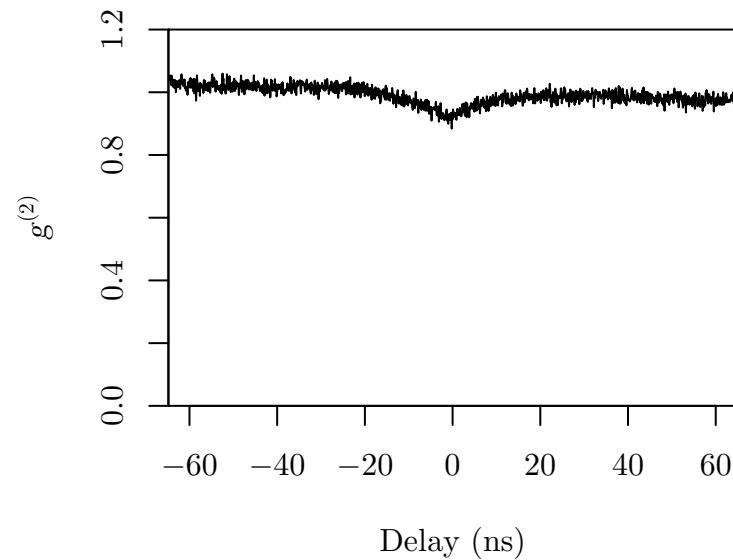


FIGURE 65. A photon antibunching with a 532 nm excitation indicates a limited number of emitters under excitation.

Since typical nanocrystals contain a large number of NV centers, resonant excitation was used to address a single NV center individually. With resonant excitation of the zero-phonon line, while detecting the emission from the phonon sidebands, an antibunching behavior is observed, as shown in Fig. 66. The normalized photon correlation falls below 0.5, confirming that the resonant excitation excites primarily a single NV center. This result agrees with earlier studies of single NV center as a single photon source [78–80].

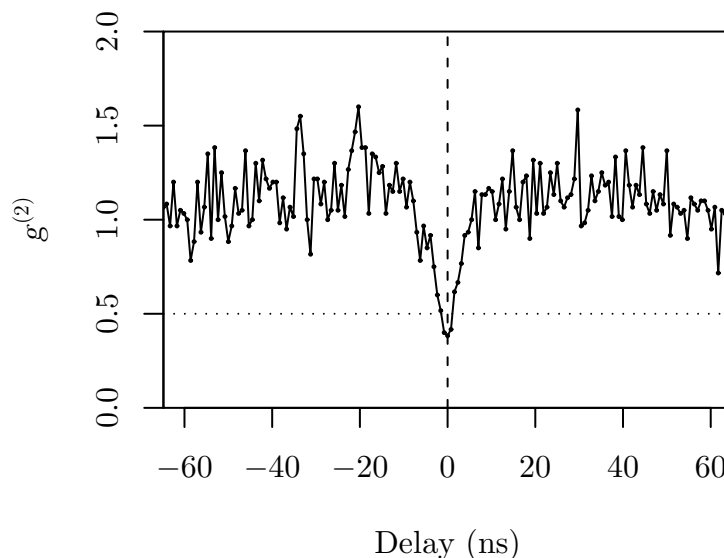


FIGURE 66. A photon antibunching of NV center emissions obtained from nanocrystal sample B, with a 100 nW 639.2 nm excitation at 9 K.

Summary

This chapter presented experimental results on homogeneous linewidth of zero-phonon lines of NV^- centers in diamond nanocrystals. Single diamond NV center has been identified individually, and single photon emission from NV center have been confirmed. The spectral diffusion of the NV optical transitions has been evaluated experimentally. The data shows that even though an overwhelming majority of the NV centers in type Ib diamond nanocrystals features strong effects of spectral diffusion and spends a significant amount of time in dark or optically inactive state, a nearly lifetime-limited zero-phonon linewidth still can be observed. Our results also suggest

that a proper sample selection and improved sample preparations may be the solution to obtain NV centers with better optical properties for future applications.

CHAPTER X

SUMMARY AND OUTLOOK

Summary

This dissertation investigates the effects of exciton-exciton interactions in the transient nonlinear optical response of electron spin coherences in undoped GaAs QWs. A spin precession manipulation scheme is presented. Strong nonlinear optical responses arising from underlying manybody interactions are observed in both DA and TRFR experiments.

We presented studies of quantum beats from electron spin coherence using degenerate TRFR. Experimental results include magnetic field dependence, temperature dependence, and laser detuning dependence. Our results agree with earlier studies. The temporal TRFR response can be understood without invoking manybody effects.

We have developed a spin manipulation scheme based on a three-pulse DA experiment. Both the amplitude as well as the phase of the DA quantum beats associated with the electron spin coherence can be controlled by tipping the spin with a control pulse. This spin manipulation scheme exploits the phase of the Larmor spin precession, instead of the optical phase of the pump or control pulses. An effective enhancement of the tipping angle associated with nonlinear optical processes is observed.

This enhancement can be understood through the coupling of electron spin coherence to two-exciton states in an N -exciton eigenstate picture. These couplings lead to a reduction of perpendicular spin component and an enhancement of parallel spin component in the DA responses. Additional experimental results of these nonlinear optical processes are also presented. This shows that by taking advantage of the manybody interactions inherent in a semiconductor, one can effectively change the read-out of the spin quantum beats.

The exciton-exciton interactions also play a crucial but qualitatively different role in TRFR. We have utilized a two-color transient pump-probe technique to reveal the underlying contributions from both bound and unbound two-exciton states in TRFR experiments. Our experimental studies of nearly degenerate TRFR of electron spin precession in an interacting exciton system show that manybody interactions between excitons strongly modify the TRFR spectral lineshape response through the coupling of the spin coherence to two-exciton states. The qualitative difference

between TRFR and transient DA nonlinear optical responses can be understood within the scope of N -exciton picture.

In addition to nonlinear optical studies on electron spin coherence in GaAs QWs, this dissertation also presents experimental studies on optical properties of NV centers in diamond nanocrystals. PL, PLE, and photon correlation experiments are carried out to investigate the zero-phonon linewidth and the spectral diffusion of NV centers. Our results indicate that the number of bright and stable NV centers is very small compared to the NV centers that incur spin-non-conserving transitions and strong spectral diffusions. A small zero-phonon linewidth of 16 MHz, however, can still be observed at low temperature from type Ib diamond nanocrystals.

Outlook

The effective enhancement of tipping angles in the spin manipulation scheme raised questions about how we can flip the spin using optical pulse, what is the condition needed, how an optical spin echo can be observed in an inhomogeneously broadened system, and what are the roles of exciton interactions in such experiments. The understanding of manybody interactions in excitonic systems hopefully can be extended by applying the two-color TRFR and three-pulse (or more pulses) DA techniques.

Another system currently of wide interest for spin coherence applications is the trion system in semiconductor heterostructures [81–87]. A trion can be considered as a charged exciton, where an exciton is bound to either an electron (X^-) or a hole (X^+). It provides an interesting Λ -type system with the spin states in the lower level states. The two-color as well as three-pulse pump-probe schemes can also be used in the trion studies.

Furthermore, a more powerful setup can be developed to integrate a spatial resolving power for the investigation of spin spatial inhomogeneity (spin imaging) as well as spin transport (spatial diffusion). Together with the ability to adjust the detuning as well as the delay and polarization of individual beams independently, there is plenty of interesting work that can be done.

The ultra robust spin coherence of NV centers in diamond crystals has emerged as a new star for today's quantum coherence studies. Current study shows strong sample dependence for the optical properties of NV centers. An improved sample preparation and selection procedure are needed to obtain a better system.

The Wang lab already demonstrated a strong coupling between the NV transition and a cavity mode in a fused silica micro-sphere resonator. With a better understanding of the optical properties of NV centers in diamond nanocrystals, creating entanglement using the electron spin coherence and the optical mode can be a promising subject. Another promising cavity system is the toroidal microcavity developed by Vahala's group [88]. A study of coupling between nanocrystals and

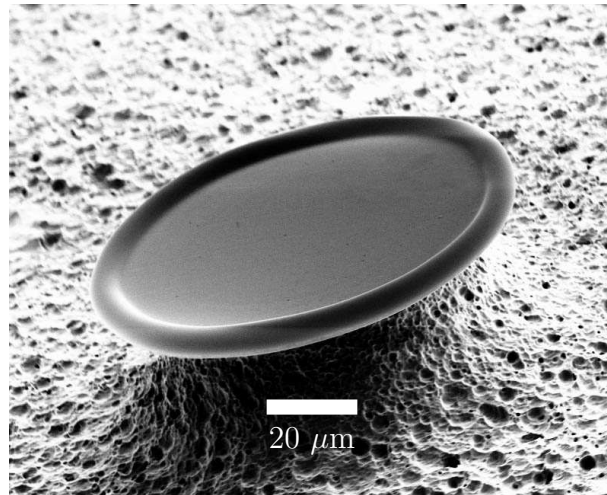


FIGURE 67. An SEM image of a toroidal silica micro cavity on a silicon chip.

the toroidal micro cavity can also be carried out in Wang lab. Figure 67 shows a preliminary result of an SEM image of a toroidal cavity on a silicon chip fabricated in the Wang lab. Future cavity QED studies can also be carried out in this system.

The efforts of exploiting electron spin coherence with optical methods in solid state systems, especially in semiconductor heterostructures and color-center defects of diamond crystals, for quantum control studies will continue to be an exciting field in physics as well as engineering researches throughout the world. In particular, with all the techniques and experimental systems already demonstrated, and the efforts put on the spin and cavity QED studies in Wang lab, I expect more exciting results coming out from this lab in the near future.

BIBLIOGRAPHY

- [1] M. J. Thorpe, K. D. Moll, J. R. Jones, B. Safdi, and J. Ye, “Broadband Cavity Ringdown Spectroscopy for Sensitive and Rapid Molecular Detection,” *Science* **311**, 1595–1599 (2006).
- [2] M. D. Lukin, “Colloquium: Trapping and manipulating photon states in atomic ensembles,” *Rev. Mod. Phys.* **75**, 457–472 (2003).
- [3] A. Schülzgen, R. Binder, M. E. Donovan, M. Lindberg, K. Wundke, H. M. Gibbs, G. Khitrova, and N. Peyghambarian, “Direct Observation of Excitonic Rabi Oscillations in Semiconductors,” *Phys. Rev. Lett.* **82**, 2346–2349 (1999).
- [4] S. A. Wolf, D. D. Awschalom, R. A. Buhrman, J. M. Daughton, S. von Molnar, M. L. Roukes, A. Y. Chtchelkanova, and D. M. Treger, “Spintronics: A Spin-Based Electronics Vision for the Future,” *Science* **294**, 1488–1495 (2001).
- [5] J. M. Kikkawa, I. P. Smorchkova, N. Samarth, and D. D. Awschalom, “Room-Temperature Spin Memory in Two-Dimensional Electron Gases,” *Science* **277**, 1284–1287 (1997).
- [6] J. A. Gupta, R. Knobel, N. Samarth, and D. D. Awschalom, “Ultrafast Manipulation of Electron Spin Coherence,” *Science* **292**, 2458–2461 (2001).
- [7] I. Zutic, J. Fabian, and D. S. Sarma, “Spintronics: Fundamentals and applications,” *Rev. Mod. Phys.* **76**, 323 (2004).
- [8] G. Salis, D. T. Fuchs, J. M. Kikkawa, D. D. Awschalom, Y. Ohno, and H. Ohno, “Optical Manipulation of Nuclear Spin by a Two-Dimensional Electron Gas,” *Phys. Rev. Lett.* **86**, 2677–2680 (2001).
- [9] *Optical Orientation, Modern Problems in Condensed Matter Sciences*, F. Meier and B. P. Zakharchenya, eds., (North-Holland, Amsterdam, 1984).
- [10] M. Dobers, K. v. Klitzing, and G. Weimann, “Electron-spin resonance in the two-dimensional electron gas of GaAs-Al_xGa_{1-x}As heterostructures,” *Phys. Rev. B* **38**, 5453–5456 (1988).
- [11] M. J. Snelling, G. P. Flinn, A. S. Plaut, R. T. Harley, A. C. Tropper, R. Eccleston, and C. C. Phillips, “Magnetic g factor of electrons in GaAs/Al_xGa_{1-x}As quantum wells,” *Phys. Rev. B* **44**, 11345–11352 (1991).

- [12] G. Breit, “Quantum Theory of Dispersion (Continued). Parts VI and VII,” *Rev. Mod. Phys.* **5**, 91 (1933).
- [13] E. Aleksandrov, “Luminiscence beats induced by pulsed excitation of coherent states,” *Opt. Spectrosc. (USSR)* **17**, 522–523 (1964).
- [14] A. P. Heberle, W. W. Rühle, and K. Ploog, “Quantum beats of electron Larmor precession in GaAs wells,” *Phys. Rev. Lett.* **72**, 3887–3890 (1994).
- [15] S. A. Crooker, D. D. Awschalom, J. J. Baumberg, F. Flack, and N. Samarth, “Optical spin resonance and transverse spin relaxation in magnetic semiconductor quantum wells,” *Phys. Rev. B* **56**, 7574–7588 (1997).
- [16] I. Malajovich, J. M. Kikkawa, D. D. Awschalom, J. J. Berry, and N. Samarth, “Coherent Transfer of Spin through a Semiconductor Heterointerface,” *Phys. Rev. Lett.* **84**, 1015–1018 (2000).
- [17] J. Shah, *Ultrafast Spectroscopy of Semiconductors and Semiconductor Nanostructures*, 2nd ed. (Springer, 1999).
- [18] M. Lindberg and S. W. Koch, “Effective Bloch equations for semiconductors,” *Phys. Rev. B* **38**, 3342–3350 (1988).
- [19] D. Birkedal, J. Singh, V. G. Lyssenko, J. Erland, and J. M. Hvam, “Binding of Quasi-Two-Dimensional Biexcitons,” *Phys. Rev. Lett.* **76**, 672–675 (1996).
- [20] S. Adachi, K. Hazu, T. Sota, S. F. Chichibu, G. Cantwell, D. B. Eason, D. C. Reynolds, and C. W. Litton, “Biexciton formation and exciton-exciton correlation effects in bulk ZnO,” *Semiconductor Science and Technology* **19**, S276–S278 (2004).
- [21] M. C. Phillips, H. Wang, I. Rumyantsev, N. H. Kwong, R. Takayama, and R. Binder, “Electromagnetically Induced Transparency in Semiconductors via Biexciton Coherence,” *Phys. Rev. Lett.* **91**, 183602 (2003).
- [22] T. Östreich, K. Schönhammer, and L. J. Sham, “Exciton-Exciton Correlation in the Nonlinear Optical Regime,” *Phys. Rev. Lett.* **74**, 4698–4701 (1995).
- [23] H. Wang, K. Ferrio, D. G. Steel, Y. Z. Hu, R. Binder, and S. W. Koch, “Transient nonlinear optical response from excitation induced dephasing in GaAs,” *Phys. Rev. Lett.* **71**, 1261–1264 (1993).
- [24] T. Östreich, K. Schönhammer, and L. J. Sham, “Theory of exciton-exciton correlation in nonlinear optical response,” *Phys. Rev. B* **58**, 12920–12936 (1998).

- [25] M. C. Phillips and H. Wang, “Exciton spin coherence and electromagnetically induced transparency in the transient optical response of GaAs quantum wells,” *Phys. Rev. B* **69**, 115337 (2004).
- [26] P. Palinginis and H. Wang, “Vanishing and Emerging of Absorption Quantum Beats from Electron Spin Coherence in GaAs Quantum Wells,” *Phys. Rev. Lett.* **92**, 037402 (2004).
- [27] C. F. Klingshirn, *Semiconductor Optics* (Springer, Verlag Berlin Heidelberg New York, 1997).
- [28] P. Y. Yu and M. Cardona, *Fundamentals of Semiconductors: Physics and Materials Properties*, 3rd ed. (Springer, 2001).
- [29] R. Winkler, *Spin-orbit coupling effects in two-dimensional electron and hole systems*, Vol. 191 of *Springer tracts in modern physics* (Springer, 2003).
- [30] M. Lindberg, R. Binder, Y. Z. Hu, and S. W. Koch, “Dipole selection rules in multiband semiconductors,” *Phys. Rev. B* **49**, 16942–16952 (1994).
- [31] S. Sarkar, P. Palinginis, P.-C. Ku, C. J. Chang-Hasnain, N. H. Kwong, R. Binder, and H. Wang, “Inducing electron spin coherence in GaAs quantum well waveguides: Spin coherence without spin precession,” *Phys. Rev. B* **72**, 035343 (2005).
- [32] V. M. Axt and A. Stahl, “A dynamics-controlled truncation scheme for the hierarchy of density matrices in semiconductor optics,” *Z. Phys. B, Condens. Matter* **93**, 195–204 (1994).
- [33] W. Schäfer, D. S. Kim, J. Shah, T. C. Damen, J. E. Cunningham, K. W. Goossen, L. N. Pfeiffer, and K. Köhler, “Femtosecond coherent fields induced by many-particle correlations in transient four-wave mixing,” *Phys. Rev. B* **53**, 16429–16443 (1996).
- [34] P. Kner, W. Schäfer, R. Lövenich, and D. S. Chemla, “Coherence of Four-Particle Correlations in Semiconductors,” *Phys. Rev. Lett.* **81**, 5386–5389 (1998).
- [35] M. Oestreich and W. W. Rühle, “Temperature Dependence of the Electron Landé g Factor in GaAs,” *Phys. Rev. Lett.* **74**, 2315–2318 (1995).
- [36] S. Pfalz, R. Winkler, T. Nowitzki, D. Reuter, A. D. Wieck, D. Hagele, and M. Oestreich, “Optical orientation of electron spins in GaAs quantum wells,” *Phys. Rev. B* **71**, 165305 (2005).

- [37] A. Fasolino, G. Platero, M. Potemski, J. C. Maan, K. Ploog, and G. Weimann, “Interband magneto-optics in GaAs/AlGaAs quantum wells in a parallel field,” *Surface Science* **267**, 509–513 (1992).
- [38] G. Goldoni and A. Fasolino, “Hole states in quantum wells under high in-plane magnetic fields: Implications for resonant magnetotunneling spectroscopy,” *Phys. Rev. B* **48**, 4948–4951 (1993).
- [39] A. M. Goebel, Master’s thesis, University of Oregon, Eugene, OR, 2004.
- [40] A. V. Kimel, F. Bentivegna, V. N. Gridnev, V. V. Pavlov, R. V. Pisarev, and T. Rasing, “Room-temperature ultrafast carrier and spin dynamics in GaAs probed by the photoinduced magneto-optical Kerr effect,” *Phys. Rev. B* **63**, 235201 (2001).
- [41] V. D. A. Baak, “Resonant Faraday rotation as a probe of atomic dispersion,” *American Journal of Physics* **64**, 724–735 (1996).
- [42] P. Palinginis and H. Wang, “Coherent Raman resonance from electron spin coherence in GaAs quantum wells,” *Phys. Rev. B* **70**, 153307 (2004).
- [43] T. Amand, X. Marie, P. Le Jeune, M. Brousseau, D. Robart, J. Barrau, and R. Planel, “Spin Quantum Beats of 2D Excitons,” *Phys. Rev. Lett.* **78**, 1355–1358 (1997).
- [44] M. Dyakonov, X. Marie, T. Amand, P. Le Jeune, D. Robart, M. Brousseau, and J. Barrau, “Coherent spin dynamics of excitons in quantum wells,” *Phys. Rev. B* **56**, 10412–10422 (1997).
- [45] M. W. Wu and H. Metiu, “Kinetics of spin coherence of electrons in an undoped semiconductor quantum well,” *Phys. Rev. B* **61**, 2945–2956 (2000).
- [46] M.-W. Wu, “Kinetic Theory of Spin Coherence of Electrons in Semiconductors,” *Journal of Superconductivity: Incorporating Novel Magnetism* **14**, 245–259(15) (2001).
- [47] N. Linder and L. J. Sham, “Theory of the coherent spin dynamics in magnetic semiconductor quantum wells,” *Physica E* **2**, 412–416 (1998).
- [48] A. Haché, Y. Kostoulas, R. Atanasov, J. L. P. Hughes, J. E. Sipe, and H. M. van Driel, “Observation of Coherently Controlled Photocurrent in Unbiased, Bulk GaAs,” *Phys. Rev. Lett.* **78**, 306–309 (1997).
- [49] M. J. Stevens, A. L. Smirl, R. D. R. Bhat, A. Najmaie, J. E. Sipe, and H. M. van Driel, “Quantum Interference Control of Ballistic Pure Spin Currents in Semiconductors,” *Phys. Rev. Lett.* **90**, 136603 (2003).

- [50] J. Hübner, W. W. Rühle, M. Klude, D. Hommel, R. D. R. Bhat, J. E. Sipe, and H. M. van Driel, “Direct Observation of Optically Injected Spin-Polarized Currents in Semiconductors,” *Phys. Rev. Lett.* **90**, 216601 (2003).
- [51] H. T. Duc, T. Meier, and S. W. Koch, “Microscopic Analysis of the Coherent Optical Generation and the Decay of Charge and Spin Currents in Semiconductor Heterostructures,” *Phys. Rev. Lett.* **95**, 086606 (2005).
- [52] A. P. Heberle, J. J. Baumberg, and K. Köhler, “Ultrafast Coherent Control and Destruction of Excitons in Quantum Wells,” *Phys. Rev. Lett.* **75**, 2598–2601 (1995).
- [53] N. H. Bonadeo, J. Erland, D. Gammon, D. Park, D. S. Katzer, and D. G. Steel, “Coherent Optical Control of the Quantum State of a Single Quantum Dot,” *Science* **282**, 1473–1476 (1998).
- [54] M. U. Wehner, M. H. Ulm, D. S. Chemla, and M. Wegener, “Coherent Control of Electron-LO-Phonon Scattering in Bulk GaAs,” *Phys. Rev. Lett.* **80**, 1992–1995 (1998).
- [55] P. Chen, C. Piermarocchi, and L. J. Sham, “Control of Exciton Dynamics in Nanodots for Quantum Operations,” *Phys. Rev. Lett.* **87**, 067401 (2001).
- [56] T. Flissikowski, A. Betke, I. A. Akimov, and F. Henneberger, “Two-Photon Coherent Control of a Single Quantum Dot,” *Phys. Rev. Lett.* **92**, 227401 (2004).
- [57] Q. Q. Wang, A. Muller, M. T. Cheng, H. J. Zhou, P. Bianucci, and C. K. Shih, “Coherent Control of a V-Type Three-Level System in a Single Quantum Dot,” *Phys. Rev. Lett.* **95**, 187404 (2005).
- [58] T. Voss, I. Ruckmann, J. Gutowski, V. M. Axt, and T. Kuhn, “Coherent control of the exciton and exciton-biexciton transitions in the generation of nonlinear wave-mixing signals in a semiconductor quantum well,” *Phys. Rev. B* **73**, 115311 (2006).
- [59] H. Haug and S. W. Koch, *Quantum theory of the optical and electronic properties of semiconductors*, 4th ed. (World Scientific, 2004).
- [60] V. M. Axt and T. Kuhn, “Femtosecond spectroscopy in semiconductors: a key to coherences, correlations and quantum kinetics,” *Reports on Progress in Physics* **67**, 433–512 (2004).
- [61] M. Ouyang and D. D. Awschalom, “Coherent Spin Transfer Between Molecularly Bridged Quantum Dots,” *Science* **301**, 1074–1078 (2003).

- [62] F. Meier, V. Cerletti, O. Gywat, D. Loss, and D. D. Awschalom, “Molecular spintronics: Coherent spin transfer in coupled quantum dots,” *Phys. Rev. B* **69**, 195315 (2004).
- [63] A. S. Lenihan, G. M. V. Dutt, D. G. Steel, S. Ghosh, and P. Bhattacharya, “Biexcitonic resonance in the nonlinear optical response of an InAs quantum dot ensemble,” *Phys. Rev. B* **69**, 045306 (2004).
- [64] T. Meier, S. W. Koch, M. Phillips, and H. Wang, “Strong coupling of heavy- and light-hole excitons induced by many-body correlations,” *Phys. Rev. B* **62**, 12605–12608 (2000).
- [65] T. A. Kennedy, J. S. Colton, J. E. Butler, R. C. Linares, and P. J. Doering, “Long coherence times at 300 K for nitrogen-vacancy center spins in diamond grown by chemical vapor deposition,” *Applied Physics Letters* **83**, 4190–4192 (2003).
- [66] R. Hanson, F. M. Mendoza, R. J. Epstein, and D. D. Awschalom, “Polarization and Readout of Coupled Single Spins in Diamond,” *Phys. Rev. Lett.* **97**, 087601 (2006).
- [67] F. Jelezko and J. Wrachtrup, “Read-out of single spins by optical spectroscopy,” *Journal of Physics: Condensed Matter* **16**, R1089–R1104 (2004).
- [68] T. Gaebel *et al.*, “Room-temperature coherent coupling of single spins in diamond,” *Nature Physics* **2**, 408–413 (2006).
- [69] C. Santori *et al.*, “Coherent Population Trapping of Single Spins in Diamond under Optical Excitation,” *Phys. Rev. Lett.* **97**, 247401 (2006).
- [70] G. M. V. Dutt, L. Childress, L. Jiang, E. Togan, J. Maze, F. Jelezko, A. S. Zibrov, P. R. Hemmer, and M. D. Lukin, “Quantum Register Based on Individual Electronic and Nuclear Spin Qubits in Diamond,” *Science* **316**, 1312–1316 (2007).
- [71] Y. S. Park, A. K. Cook, and H. Wang, “Cavity QED with Diamond Nanocrystals and Silica Microspheres,” *Nano Letters* **6**, 2075–2079 (2006).
- [72] A. Mainwood, “Nitrogen and nitrogen-vacancy complexes and their formation in diamond,” *Phys. Rev. B* **49**, 7934–7940 (1994).
- [73] M. N. B. E van Oort and M. Glasbeek, “Optically detected spin coherence of the diamond N-V centre in its triplet ground state,” *Journal of Physics C: Solid State Physics* **21**, 4385–4391 (1988).

- [74] D. A. Redman, S. Brown, R. H. Sands, and S. C. Rand, “Spin dynamics and electronic states of N-V centers in diamond by EPR and four-wave-mixing spectroscopy,” *Phys. Rev. Lett.* **67**, 3420–3423 (1991).
- [75] N. B. Manson, J. P. Harrison, and M. J. Sellars, “Nitrogen-vacancy center in diamond: Model of the electronic structure and associated dynamics,” *Phys. Rev. B* **74**, 104303 (2006).
- [76] F. Jelezko, I. Popa, A. Gruber, C. Tietz, J. Wrachtrup, A. Nizovtsev, and S. Kilin, “Single spin states in a defect center resolved by optical spectroscopy,” *Applied Physics Letters* **81**, 2160–2162 (2002).
- [77] P. Tamarat *et al.*, “Stark Shift Control of Single Optical Centers in Diamond,” *Phys. Rev. Lett.* **97**, 083002 (2006).
- [78] C. Kurtsiefer, S. Mayer, P. Zarda, and H. Weinfurter, “Stable Solid-State Source of Single Photons,” *Phys. Rev. Lett.* **85**, 290–293 (2000).
- [79] A. Beveratos, R. Brouri, T. Gacoin, J.-P. Poizat, and P. Grangier, “Nonclassical radiation from diamond nanocrystals,” *Phys. Rev. A* **64**, 061802 (2001).
- [80] A. Beveratos, S. Kühn, R. Brouri, T. Gacoin, J. P. Poizat, and P. Grangier, “Room temperature stable single-photon source,” *European Physical Journal D* **18**, 191–196 (2002).
- [81] K. Kheng, R. T. Cox, M. Y. d’ Aubigné, F. Bassani, K. Saminadayar, and S. Tatarenko, “Observation of negatively charged excitons X^- in semiconductor quantum wells,” *Phys. Rev. Lett.* **71**, 1752–1755 (1993).
- [82] A. J. Shields, M. Pepper, M. Y. Simmons, and D. A. Ritchie, “Spin-triplet negatively charged excitons in GaAs quantum wells,” *Phys. Rev. B* **52**, 7841–7844 (1995).
- [83] G. Finkelstein, H. Shtrikman, and I. Bar-Joseph, “Optical Spectroscopy of a Two-Dimensional Electron Gas near the Metal-Insulator Transition,” *Phys. Rev. Lett.* **74**, 976–979 (1995).
- [84] A. Esser, E. Runge, R. Zimmermann, and W. Langbein, “Photoluminescence and radiative lifetime of trions in GaAs quantum wells,” *Phys. Rev. B* **62**, 8232–8239 (2000).
- [85] E. Vanelle, M. Paillard, X. Marie, T. Amand, P. Gilliot, D. Brinkmann, R. Lévy, J. Cibert, and S. Tatarenko, “Spin coherence and formation dynamics of charged excitons in CdTe/Cd_{1-x-y}Mg_xZn_yTe quantum wells,” *Phys. Rev. B* **62**, 2696–2705 (2000).

- [86] G. V. Astakhov *et al.*, “Binding energy of charged excitons in ZnSe-based quantum wells,” *Phys. Rev. B* **65**, 165335 (2002).
- [87] B. Patton, W. Langbein, and U. Woggon, “Trion, biexciton, and exciton dynamics in single self-assembled CdSe quantum dots,” *Phys. Rev. B* **68**, 125316 (2003).
- [88] D. K. Armani, T. J. Kippenberg, S. M. Spillane, and K. J. Vahala, “Ultra-high-Q toroid microcavity on a chip,” *Nature* **421**, 925–928 (2003).